ACHIEVING SYNERGISM IN COMBINATION CHEMOTHERAPY FOR GASTRIC CANCER TREATMENT

by

Özen LEYLEK

A dissertation submitted to the
Graduate School of Health Sciences
in Partial Fulfillment of the requirements
for the Degree of
Doctor of Philosophy
in
Cellular and Molecular Medicine

June 20, 2023

Achieving Synergism in Combination Chemotherapy for Gastric Cancer Treatment

Koç University

Graduate School of Health Sciences

This is to certify that I have examined this copy of a doctoral dissertation by

Özen LEYLEK

and have found that it is complete and satisfactory in all respects,

and that any and all revisions required by the final

examining committee have been made.

Committee members:

Asst. Prof. Gülnihal Özcan (advisor)

Prof. Hakan Sedat Orer (co-advisor)

Prof. Tuğba Bağcı Önder

Assoc. Prof. Michael T Hemann

Assoc. Prof. Michael J Lee

Prof. Hakan Gürdal

Date: June 20, 2023

To all the girls

who bravely fight against the challenges in their education,

and all the women

who persistently battle for what they believe in…

ABSTRACT

Gastric cancer is the fifth most prevalent malignancy and the fourth-leading cause of cancer-associated deaths worldwide. Combination chemotherapy in adjunct to surgery is the mainstay of treatment in gastric cancer. However, survival rates are still very low, despite the administration of potent chemotherapeutics with different mechanisms of action in combination regimens, due to dose-limiting toxicities and chemoresistance.

Endeavors in the molecular characterization of cancer enabled the incorporation of molecular-targeted agents into combination regimens and improved treatment outcomes in several cancers. However, the number of approved targeted therapies and the benefit they provide is still limited in gastric cancer. In this thesis study, we aimed to identify the molecular-targeted agent and conventional chemotherapeutic combinations with synergistic action in gastric cancer cell models and dissect the mechanisms of synergism employing powerful functional genomic approaches.

Screening the dual combinations of small molecule inhibitors that target EGFR, mTOR, and cMET with five conventional chemotherapeutics with diverse mechanisms of action revealed erlotinib (EGFR inhibitor) and SN38 (topoisomerase I poison) as the most synergistic combination in all four cell models we tested. The synergism was much more robust in the gastric cancer cell model resistant to chemotherapy and stronger than that for combination regimens used in the clinic. Assessment of growth rate and cell death kinetics with FLICK assay validated that the synergism was due to increased cell death and a significant decrease in population size.

With a genome-wide perturbation screen and an RNAi-based signature assay, we revealed that the synergism was mainly due to the inhibition of the ABCG2 efflux pump by erlotinib, which enhanced the action of SN38. Hence this study marks the first discovery that functional genomics methodologies identify ABCG2 as an off-target of erlotinib and a potential mechanism of drug resistance against topoisomerase I poisons in gastric cancer. Based on the insights provided by this thesis study, we propose that ABCG2 inhibition by erlotinib in the presence of topoisomerase I poisons represents a promising strategy for the treatment of both naïve and chemoresistant gastric tumors.

ÖZETÇE

Mide kanseri, dünya genelindeki en yaygın beşinci kanser türü ve kansere bağlı ölümlerin dördüncü önde gelen nedenidir. Mide kanserinde, cerrahiye ek olarak kombinasyon kemoterapisi tedavinin temelini oluşturur. Bununla birlikte, farklı etki mekanizmalarına sahip etkili kemoterapötiklerin kombinasyon rejimleriyle birlikte kullanılmasına rağmen, doz sınırlayıcı toksisiteler ve kemoterapi direnci nedeniyle sağkalım oranları hala çok düşüktür.

Kanserin moleküler karakterizasyonuna yönelik çabalar, moleküler hedefli ajanların kombinasyon rejimlerine dahil edilmesini ve birkaç kanser türünde tedavi sonuçlarının iyileştirilmesini sağlamıştır. Bununla birlikte, onaylanmış hedefli tedavilerin sayısı ve sağladıkları fayda mide kanserinde hala sınırlıdır. Bu tez çalışmasında, mide kanseri hücre modellerinde sinerjistik etkisi olan moleküler hedefli ajan ve geleneksel kemoterapötik kombinasyonları tanımlamayı ve güçlü fonksiyonel genomik yaklaşımlar kullanarak sinerjizm mekanizmalarını incelemeyi amaçladık.

EGFR, mTOR ve cMET'e yönelik küçük molekül inhibitörlerinin beş farklı etki mekanizmasına sahip geleneksel kemoterapötiklerle birlikte çift kombinasyonlarının taranması, erlotinib (EGFR inhibitörü) ve SN38 (topoizomeraz I zehiri) kombinasyonunun test ettiğimiz dört hücre modelinde en fazla sinerjistik etkiye sahip olduğunu ortaya çıkardı. Sinerjizm, kemoterapiye dirençli mide kanseri hücre modelinde çok etkili ve mide kanseri tedavisinde klinikte kullanılan kombinasyon rejimlerine göre daha güçlü olduğu gözlemlendi. FLICK testi ile yapılan büyüme hızı ve hücre ölüm kinetiği değerlendirmesi, sinerjizmin artan hücre ölümüne ve popülasyon büyüklüğünde önemli bir azalmaya neden olduğunu doğruladı.

Genom genişinde bir pertürbasyon taraması ve RNAi tabanlı bir imza analizi ile, sinerjizmin temel olarak erlotinib tarafından ABCG2 dışarı atım pompasının inhibisyonuna bağlı olduğunu ve bu durumun SN38'in etkisini artırdığını ortaya koyduk. Bu çalışma, fonksiyonel genomik metodolojilerin ABCG2'yi erlotinibin yan hedefi olarak tanımlayan ve mide kanserinde topoizomeraz I zehirlerine karşı ilaç direnci mekanizması olarak potansiyel bir mekanizma olduğunu keşfeden ilk çalışma olması bakımından önem taşımaktadır. Bu tez çalışmasının sağladığı bilgiler doğrultusunda, topoizomeraz I zehirleri varlığında erlotinib ile ABCG2 inhibisyonunun hem daha önce tedavi uygulanmamış hem de kemoterapi direnci olan mide tümörlerinin tedavisi için umut verici bir strateji olabileceğini önermekteyiz.

ACKNOWLEDGEMENTS

First, I would like to express my gratitude to my supervisor, Asst. Prof. Gülnihal Özcan. Her unwavering encouragement and support have been invaluable to me throughout this long and challenging path. She consistently kept her doors open, readily offering solutions to challenges I encountered during my PhD.

I would like to thank my co-advisor Prof. Hakan Sedat Orer, and my thesis progress committee members Prof. Tuğba Bağcı Önder and Prof. Hakan Gürdal for fruitful discussions and their valuable support for the progression of this study.

I would like to express my sincere appreciation to Assoc. Prof. Michael J Lee and Assoc. Prof. Michael T Hemann for providing me with the invaluable opportunity to work in the exceptional scientific and welcoming environment. Their passion for science, strong determination, and profound knowledge have consistently inspired me, particularly at the moments when I felt discouraged. Being a visiting graduate student in Hemann Lab and Lee Lab as a Fulbright scholar with a PhD Dissertation Research Grant marked a significant milestone in my PhD journey, if not in my entire career.

The Scientific and Technological Research Council of Turkey (TUBITAK) ARDEB 3501 Grant No 117Z460 was the funding source for the early phases of my thesis study. Koç University Research Center for Translational Medicine (KUTTAM), University of Massachusetts Medical School, and Koch Institute for Integrative Cancer Research at MIT provided the necessary service and infrastructure for its successful completion. Therefore, I acknowledge these institutions for supporting my thesis study.

I would like to thank all members of GO Lab, Tevriz Dilan Demir, PhD, Ece Özmen, and Cemre Uçaryılmaz, for being great lab mates and creating such a supportive lab environment. Cemre Uçaryılmaz will always live in our memories with her enthusiasm for science.

I sincerely thank all the members of Hemann Lab and Lee Lab for their valuable assistance and inspiring scientific discussions. I would like to especially thank Megan Honeywell from Lee Lab for her support, particularly guiding me through the process of learning MATLAB and conducting CRISPR screening and its analysis. I want to extend my thank you to Peter Bruno, PhD, a former member of Hemann Lab, for his help with RNAi-based signature experiments. I would like to express my gratitude to James Ham from Hemann Lab for becoming a close friend in such a short time period and standing by my side during my visiting student period at MIT.

I want to express my heartfelt thanks to my roommates Burcu Özçimen, PhD & Fidan Şeker Polat, PhD, and my following roommates Ali Cenk Aksu, PhD & Deniz Ata, PhD for creating a warm atmosphere in our shared home. Their friendship and shared moments made my experience at Koç University truly enjoyable. Thank you for making our house feel like a place of comfort and support.

I want to thank Marco A. Quezada-Ramírez, PhD, Serkan Sayın, and Kaan Eren for their camaraderie and unwavering solidarity. They helped me a lot in overcoming all the challenges I faced during my time abroad. I would like to extend my gratitude to Alişan Kayabölen, PhD and Tolga Sever for their valuable friendship and the mutual support we have provided to each other throughout our time abroad. I am grateful for the sense of home away from home that they provided and the cherished moments that we have shared together.

I would like to sincerely thank Uğur Akcan, PhD, Nareg Pınarbaşı Değirmenci, Göktuğ Karabıyık, Özlem Yedier Bayram, PhD, Mehmet Yunus Çomar, Gizem Söyler, Buket Alpdoğan, PhD and Fatma Özgün, PhD for their friendship and support during this journey. They provided genuine companionship, which was valuable to me.

I want to express my heartfelt gratitude to my sisters, Selin Uzun Berber and Ceren Pamukcu, as well as Şahin Berber for their unconditional friendship and understanding throughout these years. Despite the moments when I may have taken time away from them, they have always been by my side, providing me enduring support and encouragement whenever I need. I am always thankful for the unbreakable bond we share.

Lastly, I cannot put into words the depth of my gratitude for the endless love and support of my beloved family. My mother, my father, and my little brother, your presence in my life is truly priceless. I am forever grateful for your love, encouragement, and belief in me. Özgün Yağmur, thank you from the bottom of my heart for holding my hand and being by my side in every step of my life.

TABLE OF CONTENTS

LIST OF TABLES

LIST OF FIGURES

NOMENCLATURE

5-FU	5-Fluorouracil
ABC	ATP-Binding Cassette
ABCB1	ATP Binding Cassette Subfamily B Member 1
ABCG2	ATP Binding Cassette Subfamily G Member 2
ANAPC4	Anaphase Promoting Complex Subunit 4
ARID1B	AT-Rich Interaction Domain 1B
ATR	Ataxia Telangiectasia and Rad3-Related Protein
AURKB	Aurora Kinase B
BCL2	B-Cell lymphoma 2
BIM	BCL2-Interacting Mediator of Cell Death
BOK	BCL2-Related Ovarian Killer
CDC45	Cell Division Cycle 45
CDK4/6	Cyclin-Dependent Kinase 4/6
CHEK1/CHK1	Checkpoint Kinase 1
CHK2	Checkpoint Kinase 2
CI	Combination Index
CIMP	CpG Island Methylator Phenotype
CIN	Chromosomal Instability
CLSPN	Claspin
c-MET	Mesenchymal-Epithelial Transition Factor
CML	Chronic Myelogenous Leukemia
COPG1	Coat Complex Subunit Gamma 1

COX2	Cyclooxygenase 2
CRISPR	Clustered Regularly Interspaced Short Palindromic Repeats
CYP2A6	Cytochrome P450 Family 2 Subfamily A Member 6
DDX39B	DExD-Box Helicase 39B
DNAPK	DNA-Dependent Protein Kinase
DRC	Dose-Response Curve
DSB	Double-Strand Breaks
EBV	Epstein-Barr Virus
ECD	Ecdysoneless Cell Cycle Regulator
EGFR	Epidermal Growth Factor Receptor
ERK	Extracellular Signal-Regulated Kinase
Fa	Fraction-affected
FABP5	Fatty Acid-Binding Protein 5
FAS	Fas Cell Surface Death Receptor
FLICK	Fluorescence-Based and Lysis-Dependent Inference of Cell Death Kinetics
GAPPS	Gastric Adenocarcinoma and Proximal Polyposis of the Stomach
GINS1	GINS Complex Subunit 1
GS	Genomically Stable
HDR	Homology-Directed Repair
HER2	Human Epidermal Growth Factor Receptor 2
HGF	Hepatocyte Growth Factor
HIST1H2BI	Histone Cluster 1 H2B Family Member I

HIST1H3D	Histone Cluster 1 H3D
ICI	Immune Checkpoint Inhibitor
JAK1	Janus Kinase 1
KEAP1	Kelch-Like ECH-Associated Protein 1
MAD1L1	Mitotic Arrest Deficient 1 Like 1
MAD2L1	Mitotic Arrest Deficient 2 Like 1
MAPK	Mitogen-Activated Protein Kinase
MDR1	Multidrug Resistance Protein 1
MLH1	MutL Homolog 1
MSH2	MutS Homolog 2
MSI	Microsatellite Instability
mTOR	Mammalian Target of Rapamycin
NHEJ	Non-Homologous End Joining
PARP	Poly (ADP-Ribose) Polymerase
PD-L1	Programmed Death-Ligand 1
PD-L2	Programmed Death-Ligand 2
PDX	Patient-Derived Xenograft
PI3K	Phosphoinositide 3 Kinase
PIK3CA	Phosphatidylinositol-4,5-Bisphosphate 3-Kinase Catalytic Subunit Alpha
PROTAC	Proteolysis-Targeting Chimera Compounds
RHOA	Ras Homolog Family Member A
RISC	RNA-Induced Silencing Complex

RNAi	RNA Interference
RNF168	Ring Finger Protein 168
RNP	Ribonucleoprotein
RPPA	Reverse-Phase Protein Array
RTK	Receptor Tyrosine Kinase
SLFN11	Schlafen Family Member 11
STK3	Serine/Threonine Kinase 3
TCGA	The Cancer Genome Atlas
TET3	Tet Methylcytosine Dioxygenase 3
TOP1	Topoisomerase 1
TOP2	Topoisomerase 2
VEGFR	Vascular Endothelial Growth Factor Receptor
WHO	World Health Organization
ZC3H18	Zinc Finger CCCH-Type Containing 18
ZNF479	Zinc Finger Protein 479
ZNF547	Zinc Finger Protein 547

1. INTRODUCTION

1.1. Gastric Cancer

1.1.1 Epidemiology and Main Risk Factors of Gastric Cancer

Gastric cancer is the fifth most prevalent cancer and the fourth-leading cause of cancer-related deaths worldwide[1]. Although the incidence rates of this malignancy have decreased globally, a recent statistical analysis estimated a 62% increase in the number of new cases by 2040[2]. According to the latest predictions published by GLOBOCAN, the incidence rate of gastric cancer in 2020 was 1,089,000 (the age-standardized incidence rate is 11.1 per 100,000), and the number of gastric cancer-associated deaths was 769,000 (the age-standardized mortality rate is 7.7 per 100,000) (Figure1.1)[3,4].

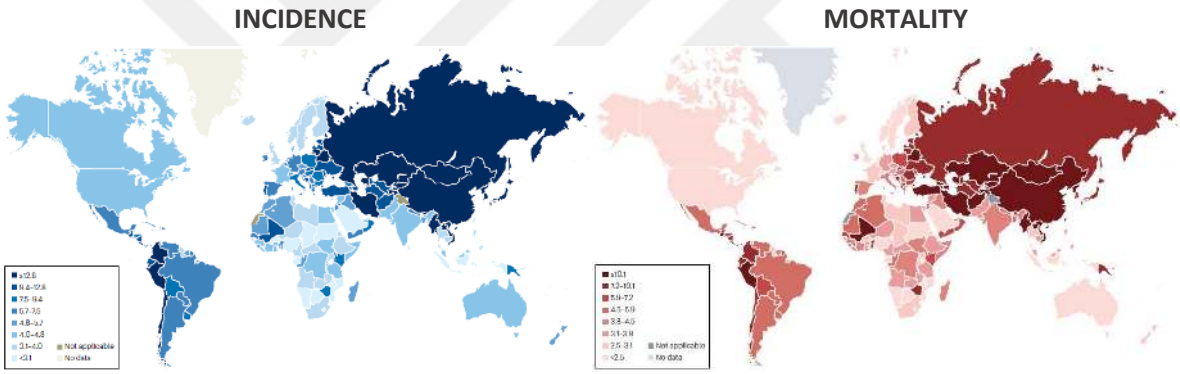

Figure 1.1: Epidemiology of gastric cancer. Maps show worldwide incidence and mortality rates of gastric cancer in 2020[3].

The main risk factors for gastric cancer are infection with *H. pylori* infection, older age, being male, tobacco and alcohol consumption, dietary factors, host genetics, Epstein-Barr virus infection and autoimmune disorders[1]. The main cause of non-cardia and intestinal-type gastric cancer is chronic infection with *H. pylori*[5,6]. Studies showed that the prevalence of *H. pylori* infection is closely related to the incidence rates of gastric cancer[7]. Tobacco consumption increases the risk of gastric cancer[8]. Alcohol consumption promotes the generation of reactive oxygen species that activate carcinogens and lead to folate deficiencies[9,10]. Both cause aberrant DNA methylation which can trigger gastric cancer

tumorigenesis[9,10]. Several studies demonstrated a strong correlation between a diet containing high salt and processed meat and an enhanced risk of gastric cancer[11,12]. The most of gastric cancer cases occurs sporadically, however, there are three types of hereditary disorders related to gastric cancer: hereditary diffuse gastric cancer, gastric adenocarcinoma and proximal polyposis of the stomach (GAPPS), and familial intestinal gastric cancer[13].

1.1.2 Histopathological and Molecular Classification of Gastric Cancer

Different types of histopathological classification systems have been developed to predict tumor characteristics and therapeutic outcomes in distinct classes of gastric cancer[14]. In the clinics, four main histopathological classification systems are widely used in different parts of the world, namely the Laurén, the World Health Organization (WHO), Goseki, and Ming classification systems[14].

The most widely used classification system for gastric cancer is Laurén classification established in 1965. Based on histopathological markers, it categorizes gastric cancer into two main groups: the intestinal and diffuse types (Figure 1.2)[15]. Some types of gastric adenocarcinomas might present the characteristics of both types or might not belong to either of these categories[16,17]. Less commonly, the mixed and unclassified types of gastric adenocarcinomas are observed[16,17].

The intestinal gastric adenocarcinoma is characterized by the well-structured glands organized in a tubular or papillary pattern[15]. The incidence rate of intestinal gastric adenocarcinoma is typically associated with male gender, older patients, and environmental factors such as *H. pylori* infection[18]. The incidence of intestinal-type gastric cancer is higher in older males[15].

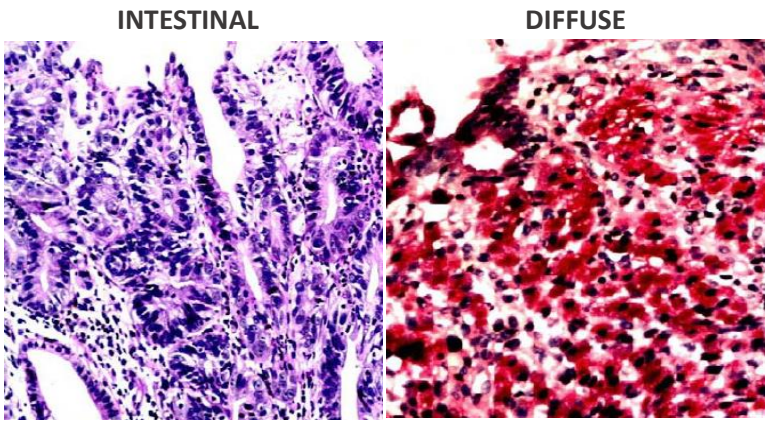

Figure 1.2: Histology of gastric adenocarcinoma subtypes. Van Gieson (VG) staining shows the well-characterized glandular or branching tubular structures of intestinal-type gastric adenocarcinoma[15]. Periodic acid-Schiff (PAS) staining is used to determine the mucine profile and atypical nuclei localization of diffuse-type gastric adenocarcinoma cells[15]. Images are at a magnification of 400x.

The diffuse-type gastric adenocarcinoma is characterized by the infiltration and diffuse growth of poorly cohesive cells that fail to form glandular structures[19]. The most characteristic cell type is signet ring cells, which contain intracytoplasmic mucin that leads to localization of the nucleus at the cell periphery[19,20]. This type of gastric adenocarcinoma is related to younger age, female gender, and genetic factors such as CDH1 mutation[15,21]. It shows more aggressive characteristics and worse prognosis compared to the intestinal type[15].

Although the Laurén classification has been widely used in clinical practices to reveal the histological characteristic of gastric adenocarcinoma, nearly 16%-26% of cases of histological diagnosis might be inconsistent with the Laurén classification[22,23]. Therefore, the histopathological classification systems might not provide an accurate information about the characteristics of gastric tumors. This pinpoints the requirement for effective classification systems that offer comprehensive insight into the biology behind the different types of gastric tumors. Such molecular classification of gastric cancer can guide the development of new targeted therapies to improve the survival rate patient suffering from this deadly disease[24].

The Cancer Genome Atlas (TCGA) research network identified the molecular characteristics of 295 primary gastric adenocarcinomas by utilizing six different high-throughput platforms, including array-based somatic copy number analysis and DNA methylation, mRNA and miRNA sequencing, whole genome sequencing, and reverse-phase protein array (RPPA)[24]. It built a more robust classification system characterizing core dysregulated pathways and molecular drivers of gastric cancer[24]. Based on the results, four main molecular subtypes of gastric cancer were identified: Epstein-Barr virus-infected tumors (EBV) (9%), tumors with microsatellite instability (MSI) (22%), genomically stable tumors (GS) (20%), and tumors with chromosomal instability (CIN) (50%)[24].

The four TCGA molecular subtypes of gastric cancer exhibited distinct genomic characteristics and mutational signatures[24]. EBV-positive tumors showed CpG island methylator phenotype (CIMP), non-silent PIK3CA mutation (80%), and the amplification of JAK1, PD-L1, and PD-L2[24]. The mutation rate was significantly enhanced in MSI tumors compared to the other, especially in the genes that encode targetable oncogenic proteins[24]. GS tumors mostly harbored different types of mutations in RHOA gene and gene fusions in RHO-family GTPase-activating proteins[24]. Aneuploidy and the amplification of receptor tyrosine kinases (RTK) were frequently observed in CIN tumors[24]. EGFR overexpression through gene amplification and enhanced EGFR phosphorylation was observed in the CIN subtype[24]. Main characteristics of these molecular subtypes (Figure 1.3A) and key alterations in RTK/RAS and RTK/PI3K pathways (Figure 1.3B) are summarized in Figure 1.3. Despite that TCGA molecular classification system paved the way to the molecular characterization of gastric adenocarcinomas, the knowledge it presented has not been translated into effective therapies, yet.

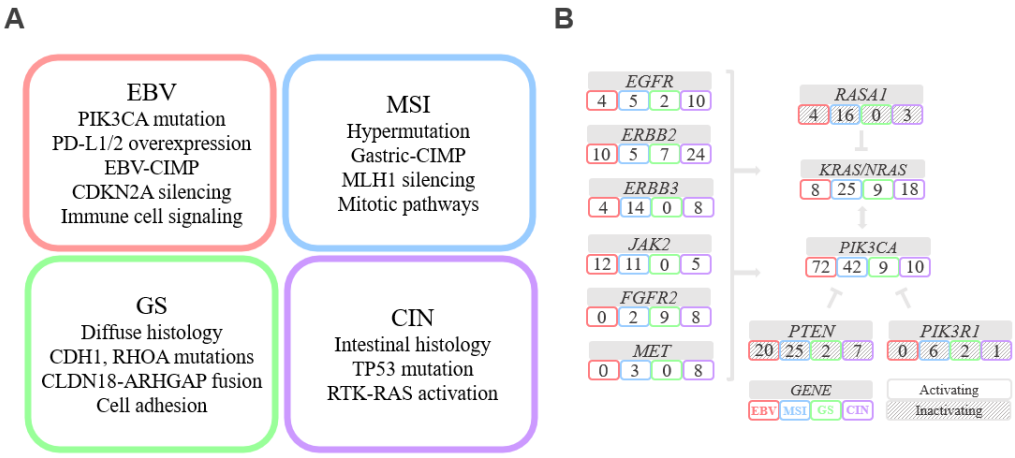

Figure 1.3: Characteristics of molecular subtypes of gastric cancer. A. Molecular features associated with four molecular subtypes of gastric cancer. B. Alterations in RTK/RAS and RTK/PI3K signaling pathways among molecular subtypes. Both panels are adapted from[2].

1.2 Current Treatment Strategies for Gastric Cancer

Gastrectomy and total lymphadenectomy accompanied by neoadjuvant, or adjuvant chemotherapy is the mainstay of treatment in resectable gastric tumors[25,26,27]. However, palliative chemotherapy is the standard approach in advanced/unresectable gastric cancer[27]. Common chemotherapy regimens are based on combining chemotherapeutics from different groups to achieve increased anti-cancer effect and decrease non-specific toxicity by administering different agents with non-overlapping toxicities at low doses.

5-fluorouracil-based chemoradiotherapy following surgery was accepted as a standard treatment approach in the US, which enhanced overall survival and recurrence-free survival in comparison with surgery alone[25]. ECF combination regimen (epirubicin, cisplatin, 5-fluorouracil) was approved as the first-line treatment followed by surgery in Europe since it significantly increased the overall survival of patients[26]. However, a randomized phase III clinical trial demonstrated that the FLOT combination regimen (5-fluorouracil, leucovorin, oxaliplatin, and docetaxel) improved the treatment efficacy and patient survival compared to ECF[28]. Therefore, FLOT followed by surgery was accepted as a new standard

approach for gastric cancer treatment in Europe[27]. According to the results of a phase III clinical trial, CAPOX combination (capecitabine and oxaliplatin) following surgery improved both disease-free and overall survival of patients with stage II/III gastric cancer[30].

Chemotherapy was also shown to improve the overall survival of patients with metastatic or unresectable[31]. Two randomized phase III trials demonstrated that the treatment efficacy was significantly improved by chemotherapy compared to palliative care alone in 208 patients with advanced/metastatic gastric cancer[32,33]. The combination of platinum and fluoropyrimidine is globally accepted as a first-line treatment in advanced stage gastric cancer[34]. The most commonly used platinum-derived agents are cisplatin and oxaliplatin in this combination[35]. However, cisplatin has been substituted with oxaliplatin in recent years due to the lower toxicity profile[35]. In addition, a phase III clinical trial evaluated the DCF triplet regimen (docetaxel, cisplatin, and 5-fluorouracil) in patients with advanced gastric cancer[36]. Despite the improved overall survival, DCF combination led to severe toxicities in patients[27]. Dose optimization studies have overcome this handicap. Hence, dose-modified DCF (mDCF) has been accepted as a first-line treatment for patients with advanced gastric cancer[37,38].

Despite the administration of potent anti-cancer agents in combination regimens, overall survival rates are still low in gastric cancer. The development of treatment approaches as if gastric cancer is a uniform entity, despite its histologically and molecularly variant presentation among patients, is one of the reasons for the failure of therapy. A more comprehensive knowledge about tumor biomarkers and the development of molecular-targeted approaches is crucial to increase therapeutic success in gastric cancer.

1.2.1 Targeted Therapies for Gastric Cancer

The endeavors to understand the molecular processes underlying tumor progression paved the way for the development of targeted therapy-based treatment approaches in cancer. Since conventional therapeutics have a high risk of non-selective toxicity to healthy tissues, incorporating molecular-targeted agents into the combination regimens enabled the use of conventional chemotherapeutics at lower doses while preserving the anti-tumor efficacy. Therefore, the use of molecularly targeted agent-conventional chemotherapeutic combinations became an attractive approach in cancer therapy. However, the targeted therapies approved for gastric cancer are limited to trastuzumab[39], pembrolizumab[40], nivolumab[41], and ramucirumab[42].

Trastuzumab monoclonal antibody that inhibits HER2 receptor has been incorporated in cisplatin-fluoropyrimidine combination, which has improved the overall survival of patients with advanced or HER2-positive gastric cancers[39]. Hence, evaluating HER2 positivity became a critical step to determine treatment strategy in metastatic gastric cancer[35]. Several clinical trials have also assessed HER2-targeting agents for the treatment of locally advanced gastric cancer[35]. A clinical trial showed that the addition of two HER2-targeting agents to the FLOT regimen enhanced the pathological complete response, compared to FLOT alone[43].

Immune checkpoint inhibitors (ICIs), especially anti-PD1 antibodies including pembrolizumab and nivolumab, have been evaluated in many clinical trials in combination with the standard regimens for gastric cancer treatment[35]. A clinical trial showed that the incorporation of pembrolizumab in standard chemotherapy improved the overall survival of patients[40]. In another clinical trial, the progression-free survival of patients was extended by nivolumab combined with oxaliplatin-based chemotherapy, despite that the overall survival did not improve[41]. The combination of ICIs with trifluridine/tipiracil (FTD/TPI) has been recently approved as a pioneering treatment strategy for the third-line or later settings in advanced gastric cancer therapy[44]. Many ongoing studies investigate how chemotherapy affects the patient response to immunotherapies and which

subsets of patients benefit from agents targeting immune checkpoints[35]. For instance, patients with microsatellite unstable or EBV-positive gastric tumors are more responsive to immunotherapies[45].

Inhibition of angiogenesis, an important cancer hallmark, using small molecule inhibitors or monoclonal antibodies is of clinical interest for gastric cancer treatment[35,46]. Gastric tumors highly express the vascular endothelial growth factor receptor (VEGFR) and cytokines, involved in angiogenesis[35]. Ramucirumab, a VEGFR-targeting humanized monoclonal antibody, failed to elicit an increased efficacy as monotherapy in a clinical trial[47]. However, the combination of ramucirumab and paclitaxel improved the overall survival in gastric cancer patients, compared to paclitaxel alone in another clinical trial[42]. Hence, it has been approved a new standard treatment approach for gastric cancer therapy[35].

Despite that trastuzumab, nivolumab, pembrolizumab, and ramucirumab increased treatment response to some extent, they are effective in a small group of advanced-stage patients with target positivity. Therefore, identifying new drug targets and exploring the efficacy of new molecular targeted agents in combination with conventional chemotherapy is crucial to improve treatment outcomes in gastric cancer patients. Studies in the last decades suggest epidermal growth factor receptor (EGFR), mechanistic target of rapamycin (mTOR), and c-MET as potential targets to increase treatment efficacy in gastric cancer.

1.2.2 EGFR, mTOR, and c-MET as Drug Targets in Gastric Cancer Therapy

EGFR is a transmembrane receptor tyrosine kinase activated by the binding of epidermal growth factor (EGF)[48]. Increased expression and/or enhanced activity of this receptor contribute to the development of several malignancies[48]. EGFR plays an important role in tumorigenesis by stimulating cell proliferation, angiogenesis, and metastasis, and also by inhibiting apoptotic cell death[48]. EGFR amplification or overexpression is observed in 5-10% of gastric cancer cases[49,50]. In addition, enhanced EGFR expression is associated with dismal prognosis in

gastric cancer[51,52]. Studies proved that silencing EGFR expression suppressed the growth and invasion ability of gastric cancer cells and increased apoptotic cell death[53]. Monoclonal antibodies and tyrosine kinase inhibitors targeting EGFR have achieved successful therapeutic responses in gastric cancer cell lines[54,55]. As an example, cetuximab, a chimeric (mouse/human) monoclonal antibody targeting EGFR showed a synergistic effect in combination with irinotecan by inducing cell cycle arrest at G2/M phases and apoptosis in gastric cancer cell models[56]. Cetuximab increases the sensitivity of gastric cancer cells to oxaliplatin treatment[57]. In addition, gefitinib, a small molecule inhibitor targeting EGFR enhanced cell death in gastric cancer cells and elicited synergy in combination with paclitaxel[58]. However, EGFR inhibitors failed to achieve enhanced therapeutic response in clinical trials.

The combination of cetuximab with cisplatin and docetaxel or with capecitabine and oxaliplatin did not increase progression-free survival or overall survival of gastric cancer patients in a phase III clinical trial[59,60]. The addition of cetuximab to the combination of capecitabine and cisplatin did not provide an additional benefit for the treatment of advanced gastric cancer in another phase III clinical study[61]. In a double-blind randomized phase II study, it was observed that gefitinib could reach the tumor tissue and inhibit EGFR activity sufficiently but did not improve the patient response significantly[62]. However, other clinical studies conducted based on biomarker analyses showed better results in patients with EGFR-amplified tumors, improving the response rate by 58% and progression-free survival for 10 months[63].

mTOR is a serine/threonine kinase from the kinase family associated with the phosphoinositide 3-kinase (PI3K) pathway[64]. By forming a complex with different proteins, mTOR stimulates cell growth and cell cycle progression, inhibits autophagy, and promotes cell survival[65]. mTOR overexpression is associated with advanced gastric cancer and a low survival rate[66]. Studies have shown that mTOR inhibition substantially suppressed tumor growth and vascularization in subcutaneous and orthotropic gastric cancer mouse models[67]. In

a xenograft gastric cancer tumor model, everolimus, a small molecule inhibitor of mTOR, in combination with high dose cyclophosphamide increased the sensitivity of gastric cells to the chemotherapy[68].

Only a limited number of patients with advanced gastric cancer who did not respond to the combination of fluoropyrimidines and platinum responded to everolimus treatment in a phase II study[69]. However, it could not achieve an increase in progression-free survival and overall survival. In another phase II study in advanced gastric cancer refractory to chemotherapy, 45% of the patients had a decrease in tumor volume with everolimus treatment, but no difference was observed in complete or partial response[70]. Only 10.6 % of the patients who had been previously treated with at least two lines of systemic chemotherapy responded to the combination of capecitabine and everolimus[71]. The incorporation of low-dose everolimus into the combination of cisplatin, 5-fluorouracil, and leucovorin regimen as first-line treatment did not change the response rate in patients with advanced gastric cancer[72].

c-MET is a hepatocyte growth factor receptor in the receptor tyrosine kinase family[73]. It plays an important role in tumor growth, survival, angiogenesis, and metastasis. c-MET gene amplification and protein overexpression have been associated with gastric cancer progression, increased risk of distant metastases, and reduced survival[74]. The inhibition of c-MET protein expression suppressed the peritoneal spread in gastric cancer models[75]. Studies showed that c-MET inhibitor SU11274 increased the sensitivity of gastric cancer stem cells to irinotecan[76]. c-MET inhibitor SAR125844 suppressed tumor growth in gastric cancer xenograft models overexpressing c-MET in a dose-dependent manner[77].

Foretinib and tivantinib, small molecule inhibitors of c-MET, could not achieve an efficacious response in gastric cancer patients in phase II trials[78]. Although the combination of the ECX regimen (epirubicin, cisplatin, and capecitabine) with rilotumumab, an anti-HGF antibody, achieved an increase in survival and the reduction of tumor mass[79], this combination did not improve patient survival in the randomized double-blind phase III trial[80].

Targeted therapies against EGFR, mTOR, and c-MET failed to improve progression-free survival or overall survival of patients in most of the clinical trials mentioned above, although they showed promising results in in vitro or xenograft gastric cancer models. In these trials, EGFR, mTOR, and c-MET-targeting agents were administered to gastric cancer patients without the stratification of the patient populations based on biomarker positivity. This might be one of the possible reasons that can explain the failures in these studies. Since the majority of clinical trials were performed in unselected patient populations which may include individuals who were not expected to benefit from the treatment, the efficacy of these treatments was limited. The mutational profile of gastric cancer tumors is highly complex and shows significant variabilities between patients as well as within the same patient's tumor. Thus, the molecular characterization of tumor samples is a crucial step to select the right patient populations and to design effective therapy regimens. This can improve the patient's responses to targeted therapies in gastric cancer treatment. In addition, although targeted therapies initially demonstrate an increased efficacy against gastric tumors, the spatial and temporal heterogeneity of the tumor might be altered during treatment, contributing to the development of therapy resistance. As a result, continuous monitoring of the tumor and the identification of new biomarkers are essential to guide the therapeutic approaches and improve patient outcomes. This underscores the need for personalized medicine based on the molecular characterization of the patient's tumor, genetic background, and medical history to develop a tailored treatment strategy.

1.3 Rational Selection of Drugs in Combination Therapy and Synergism

One of the critical factors that would increase the success of molecular-targeted agents is to select drug combinations rationally. Most of the drug combinations used clinically are selected empirically by a trial-and-error approach over decades. However, the drugs in a combination regimen may exhibit three different types of interactions: antagonism, additivity, and synergism[81]. To reach the main aims of combination chemotherapy in cancer -increasing anti-tumor

efficiency, decreasing non-specific toxicity, preventing drug resistance, and addressing tumor heterogeneity- the drugs in combination should exhibit a synergistic effect. Irrational combination strategies may be the reason for the failure of EGFR, mTOR, or c-MET targeting agents in clinical trials. Additionally, reliable synergism measures should be used to identify efficacious drug combinations. Hence in this project, we investigated the effect of combining EGFR, mTOR, or c-MET inhibitors with 5 different conventional chemotherapeutics with distinct mechanisms of action and used efficient methods to identify synergism in drug combinations.

1.4 Mechanisms of Action of Conventional Chemotherapeutics Used in The Study

To rationally identify synergistic combinations in gastric cancer, we analyzed dual combinations of the inhibitors of EGFR, mTOR, or c-MET with five different conventional chemotherapeutics in gastric cancer cell models in this thesis study. Our conventional chemotherapeutics are SN38 – an active metabolite of irinotecan (topoisomerase I inhibitor), doxorubicin (topoisomerase II inhibitor), cisplatin (platinum derivative), 5-fluorouracil (anti-metabolite), and paclitaxel (mitosis inhibitor), which exhibit diverse mechanisms of action, explained below.

1.4.1 Topoisomerase Inhibitors

Topoisomerases are key enzymes in resolving structural and topological complexes during DNA replication and transcription[82]. These enzymes trigger a reaction that breaks DNA strands and forms a covalent phospho-tyrosine link while simultaneously breaking DNA phosphodiester bonds. Hence, topoisomerases enable the release of DNA superhelices without causing DNA damage[82].

There are two types of topoisomerases: type I which breaks one DNA strand at a time and type II which break both strands of the DNA double helix simultaneously[82]. These classes are further categorized into IA, IB, IIA, and IIB based on their structural and mechanistic similarities[82].

Topoisomerase inhibitors disrupt the covalent DNA-topoisomerase complex and induce DNA damage, which causes replicative and transcriptional stress, cytotoxicity, and ultimately cell death[82]. These inhibitors are mechanistically classified into six main groups[82]. The first group of agents prevents DNA binding by competitively inhibiting the topoisomerase active site[83]. The second group acts as "topoisomerase poisons" by forming a locked ternary complex of DNA-topoisomerase-inhibitor, which prevent DNA re-ligation[84]. Inhibitors in the third category competitively inhibit the ATP binding pocket, which interferes with the ATP hydrolysis of type II enzymes[85]. The fourth group of topoisomerase inhibitors binds to the target DNA and prevents topoisomerase binding[86]. The fifth group binds to the DNA-topoisomerase complex and causes DNA cleavage[86]. The last category inhibits ATP hydrolysis, and therefore, blocks the release of DNA by type II enzymes after strand passage[87].

Topoisomerase poisons classified within the second category represent the predominant class of topoisomerase inhibitors administered to cancer patients. These include camptothecin derivatives such as irinotecan and topotecan, anthracycline derivatives including doxorubicin, epirubicin, and daunorubicin, and epipodophyllotoxin-derived agents like etoposide[82]. Camptothecin derivatives cause DNA double-strand breaks by targeting type I topoisomerases[88]. This inhibits DNA replication and induce cytotoxicity[88]. On the other hand, anthracycline derivatives and epipodophyllotoxin-derived agents act on type II topoisomerases[89]. These anti-cancer drugs intercalate into DNA-topoisomerase complex or directly bind to topoisomerase II, respectively[89]. This results in the formation of a stable ternary complex that prevents DNA re-ligation during replication[89].

1.4.2 Platinum Derivatives

Platinum derivatives form DNA adducts, which prevent DNA replication and suppress mRNA and protein synthesis, ultimately triggering cell death. Cisplatin is one of the most extensively used platinum-based agents[82]. It primarily modifies the N7 position of guanine[82]. This results in the formation of DNA-

cisplatin adducts, which is the responsible mechanism for the cytotoxic effect of cisplatin[82]. It has been approved as an anti-cancer agent for various cancer types, including gastric, breast, pancreatic, bladder, and non-small cell lung cancers[82].

1.4.3 Anti-metabolites

Anti-metabolite agents function as analogs of biological compounds, which inhibit their synthesis and involvement in biological processes[82]. As a result, these agents interrupt crucial metabolic pathways, especially DNA synthesis, which elicits enhanced cytotoxicity in rapidly dividing cells[82]. Anti-metabolite agents can be classified into three main categories: antifolates, ribonucleotide reductase inhibitors, and nucleoside analogs[82]. Antifolates, exemplified by methotrexate, inhibit the activity of enzymes involved in folate metabolism which plays an important role in DNA replication and the synthesis of tetrahydrofolic acid and purine[90]. Ribonucleotide reductase inhibitors inhibit the activity of ribonucleotide reductase enzyme, which disrupts the synthesis of nucleotide precursors essential for DNA synthesis[91]. Nucleoside analogs are further categorized into two classes: (1) purine analogs such as mercaptopurine and thioguanine, and (2) pyrimidine analogs that include 5-fluorouracil, cytarabine, and gemcitabine[92]. These agents either inhibit specific enzymes involved in nucleotide synthesis or mimic natural nucleosides[92]. These actions ultimately lead to the inhibition of DNA and RNA synthesis[92].

1.4.4 Mitotic Inhibitors

Mitotic inhibitors cause permanent arrest of the cell cycle by preventing the polymerization or depolymerization of actin, tubulin, or microtubules[93]. This leads to chromosome misalignment and activation of the spindle assembly checkpoint[94]. As a result, cells arrested at the cell cycle either die during mitosis or bypass the spindle assembly checkpoint which results in aneuploidy and cell death[93]. Mitotic inhibitors are classified into 4 main categories: (1) enhancers or stabilizers of actin polymerization (jasplakinolide, phalloidin), (2) inhibitors of actin polymerization (cytochalasin, latrunculin, and swinholide), (3) enhancers or stabilizers of microtubule polymerization (paclitaxel), (4) inhibitors or inducers of microtubule

polymerization (colchicine, nocodazole, vinblastine, rotenone, demecolcine)[82]. Paclitaxel, vinblastine, and demecolcine, which primarily target microtubules, are of significant clinical importance and are widely used in the treatment of various cancer types including breast, ovarian, lung, pancreatic cancer, and melanoma[82].

1.5 Pharmacological Interactions in Combination Therapy

Many experimental and theoretical studies have been performed to develop a standardized methodology that quantitatively defines the degree of effect of the drug combination[81]. Despite all challenges, these studies provided a plausible definition of synergism and antagonism in combination therapy[81]. Synergism and antagonism refer respectively to a greater and lesser effect than additivity[81]. Hence, this definition makes it crucial to define additivity correctly, to understand the pharmacological interactions in combination therapy.

Current methodologies that define pharmacological interactions use mainly two different approaches: effect-based and dose-effect-based approaches[81]. Effect-based approaches compare the effect of single agents to the combination[81]. There are four main effect-based strategies, which are combination sub-thresholding, highest single agent, response additivity, and bliss independence[81].

Combination sub-thresholding requires the combination of ineffective doses of single agents and compares responses to that of the untreated control group using statistical testing with a p-value cut-off of 0.05[81]. The disadvantage of combination sub-thresholding is that it does not provide a clear distinction between responses to single agents and combination since the effectiveness of treatments is evaluated based on the statistical threshold[95].

The highest single-agent approach, also known as the Gaddum's non-interaction[96], compares the effect of single agents with the effect of the combination[81]. It then uses statistical testing that calculates the p-value to evaluate the difference between a single agent achieving the highest response and the combination[81]. As it only compares the combination with the highest single agent,

it fails to discriminate synergistic combination therapies from combinations with additive effect[81].

The response additivity method compares the observed effect of combination with the expected effect[81]. It utilizes statistical testing to understand the significance of pharmacological interaction in combination[97]. However, it assumes that single agents applied in combination exhibit linear dose-response curves with zero intercepts, although dose-response curves are generally characterized by a sigmoidal shape[81]. This might lead to misinterpretation of the pharmacological interaction in drug combinations.

The bliss independence model, also known as probabilistic independence, compares the effect of combination to the expected additivity which is inferred from the probability of the independent contribution of every single agent to the combinations' effect[98]. Although it is one of the widely used effect-based models, it has three main limitations[81]. The first one is its dependence on the assumption that agents exhibit a sigmoidal dose-response curve, which may not be valid for certain drugs[81]. Another limitation is that it is only applicable to individual agents that show expected additivity within the probability range of 0 to 1[81]. Moreover, it fails to consider any possible interactions between the drugs that might target the same biological pathway or molecule[81].

Dose-effect-based approaches offer a different perspective on the pharmacological interactions in drug combinations[96]. These approaches focus on finding the doses applied in combination that achieve the same quantitative effect with the reference dose of individual agents[96]. This allows for more precise comparison of the effects of single agents with nonlinear dose-response curves[81]. Dose-effect-based approaches provide a more clear definition of synergism, additivity, and antagonism based on the expected additive effect in combination which depends on the individual dose-response curves[81].

Isobologram analysis and combination index theorem are widely used dose-effect-based strategies[81]. The mathematical framework used in these models was formally proposed by Loewe, also known as Loewe additivity[81,99]. These models

have utilized Loewe additivity to derive several mathematical models for the analysis of pharmacological interactions in drug combinations[81]. Isobologram analysis is a graphical method used to determine the pharmacological interaction in combination treatments based on the comparison of the observed effect with that predicted under the assumption of Loewe additivity[100]. Isobologram curves are obtained by plotting the doses of single agents that are required to have an additive effect in combination[100]. The effect of the combination is defined as additivity when the response observed in combination is on the isobologram curve[100]. The combination exhibits synergistic or antagonistic effects when the response is under or above the isobologram curve, respectively[100]. An example plot for isobologram analysis is shown in Figure 1.4A.

The combination index theorem developed by Chou and Talalay offers a more quantitative evaluation of pharmacological interactions in combination treatments. It is derived from the Loewe additivity model and developed based on the median-effect equation derived from the mass-action law principle[102]. The Chou-Talalay method referred combination index theorem is the unified theory encompassing Michaelis-Menten, Hill, Scatchard, and Henderson-Hasselbalch equations, which formulate enzyme kinetics, the interaction between ligand and binding site, binding affinity, and pH balance, respectively[102].

According to the combination index theorem, the combination with additive effect exhibits a combination index of 1[101]. The combination is defined as synergistic or antagonistic when the combination index is lesser or greater than 1, respectively[101]. At least five different doses of individual agents should be tested to calculate the combination index reliably[101]. The combination index theorem is more response-oriented compared to the isobologram method which is more dose-oriented. The response-combination index plot of the Chou-Talalay method allows us to understand the degree of pharmacological interaction in combination at each response level[101]. This method also facilitates interpreting data derived from combinations including more than two agents[101]. An example plot for the combination index theorem is shown in Figure 1.4B.

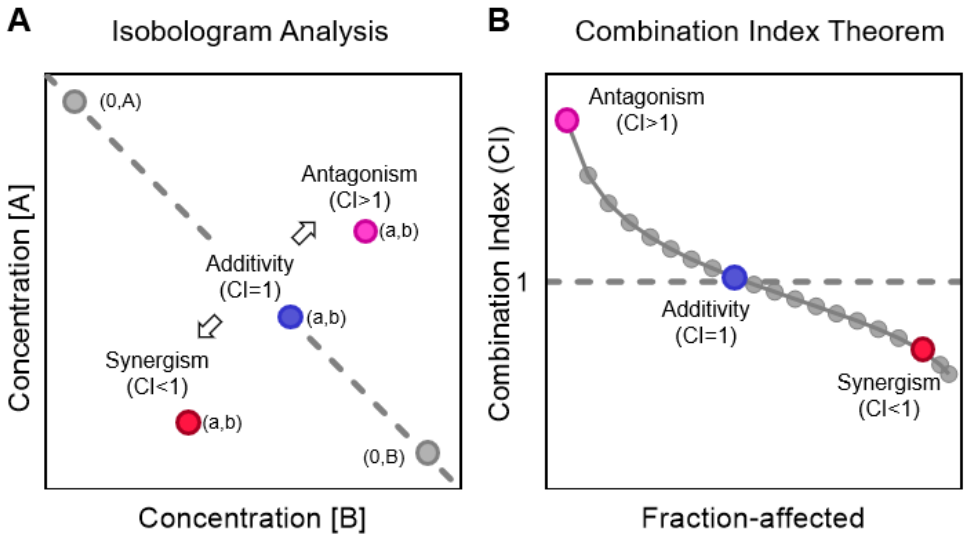

Figure 1.4: Dose-effect-based approaches. A. Isobologram analysis of a drug combination. The line of additivity is determined by the individual doses of drugs A and B. The doses in combination are represented by a and b. The localization of the combination induced by a and b is compared to the line of addivity, which determines the pharmacological interaction as synergy, addivity, or antagonism. The figure is adapted from a publication of Foucquier J. & Guedj, M[81]. B. The quantitative fraction-affected (fa) – combination index (CI) plot based on combination index theorem developed by Chou-Talalay to calculate CI values for give data points[101]. The Compusyn program, originally developed by Chou, generates a simulated fa – CI curve based on actual experimental data and predicts CI values for effect levels ranging from 0.05 to 0.97 when the individual drug components are combined at a constant ratio[101]. CI<1, CI=1, and CI>1 are interpreted as synergy, additivity, and antagonism, respectively.

The combination index theorem calculates the combination index using the equation represented in Figure 1.5 and allows the quantitative determination of synergism, additivity, and antagonism[101]. In this thesis project, we used the Chou-Talalay combination index method to reliably assess synergism in drug combinations.

$$\text{Combination Index (CI)} = \frac{[X_{combination}]}{[X_{single}]} + \frac{[Y_{combination}]}{[Y_{single}]}$$

Figure 1.5: Simplified formulation of Chou-Talalay's CI theorem. X and Y denote two different agents. The denominators represent the drug concentration required to induce a specific degree of drug response when the drug X or Y administered alone. The nominators indicate the concentrations of X or Y in combination that achieves the same degree of drug response.

In addition to identifying synergistic drug combinations rationally, we aimed to understand the molecular mechanisms of synergistic action in this study, since this knowledge paves the way for the development of new and efficacious molecular targeted agents. Hence, a comprehensive review of the mechanisms of synergism is crucial here.

1.6 Pharmacodynamic Actions Achieving Synergism

Combination therapies can exhibit synergism by diverse mechanisms. An extensive literature search by Jia et al. reveals three main pharmacodynamic actions that achieve synergism: complementary, anti-counteractive, and facilitating actions[103]. A schematic example for each action is provided in Figure 1.6.

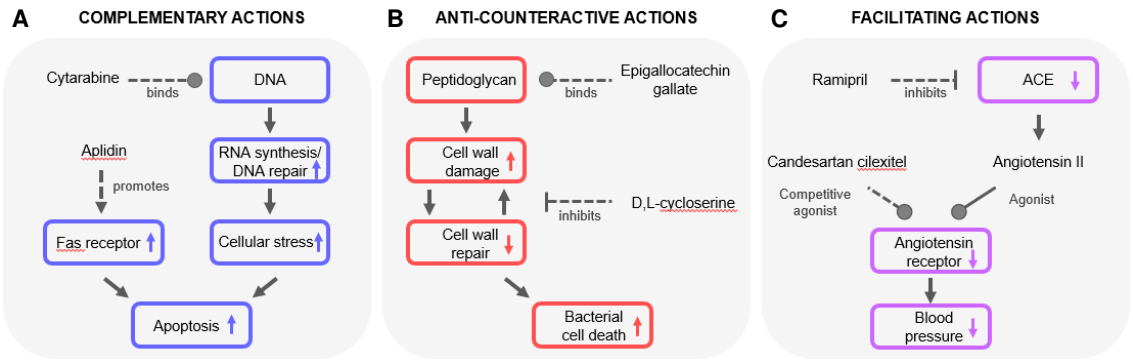

Figure 1.6: Pharmacodynamic actions achieving synergy. A. Complementary action: Aplidin enhances the activation of the FAS receptor, which triggers extrinsic apoptosis. Cytarabine, on the other hand, inhibits RNA synthesis and DNA repair, inducing cellular stress and apoptosis. B. Anticounteractive action: Cycloserine interferes with the bacterial cell wall synthesis and epigallocatechin gallate damages the bacterial cell wall repair function, leading to cell death. C. Facilitating action: Candesartan cilexitel competes with angiotensin II and inhibits the angiotensin receptor. Ramipril inhibits the production of angiotensin II. The figure is adapted from the study by Sun et al.[104].

Complementary actions mainly cover the positive modulation of a target or process by simultaneously acting on the multiple nodes of the same pathway or its interconnected pathways[103]. These actions involve interactions with various sites, conformations, states, and mutant forms of the target, which cooperatively alter the target activity and/or expression[103]. Furthermore, these actions effectively enhance positive effects and decrease negative effects associated with the target[103]. For instance, the combination of celecoxib and emodin elicits synergy through complementary actions that inhibit different targets within the same pathway, which leads to the repression of cancer cell growth[105]. Celecoxib, an inhibitor of cyclooxygenase 2 (COX2), inhibits AKT protein kinase and disrupts the growth of certain types of cancer cells[105]. Emodin inhibits tyrosine kinases in the PI3K pathway that activates AKT, interrupting the suppression of apoptosis by AKT[105]. Therefore, emodin complements the inhibitory effect of celecoxib on AKT

activity, which achieves synergy by inhibiting cancer cell growth and triggering apoptotic cell death[105].

Anti-counteractive actions result from interactions with an antagonist or inhibitory target and negative regulation of network robustness and counteractive actions[103]. Synergistic combinations with anti-counteractive effects show an effect on distinct targets within the same or interconnected pathways or different sites on the same target[103]. For instance, anti-counteractive action is employed by the combination of cisplatin and topotecan as an anti-cancer treatment[106]. Cisplatin generates DNA adducts which are bypassed during replication through a mutagenic translesional bypass mechanism[106]. On the other hand, topotecan inhibits topoisomerase I and stabilizes the covalent complexes formed by topoisomerase and DNA, which prevents the progression of the replication fork[106]. Thereby, the counteractive effect against cisplatin action is reduced by topotecan, resulting in synergism between two anti-cancer agents[106].

Facilitating actions stem from the secondary effect of one agent that boosts the activity or potency of the other[103]. These actions can be exemplified through the combination of gentamicin and vancomycin, which elicits synergy in penicillin-resistant strains[107]. Gentamicin strongly inhibits the bacterial ribosome, and therefore, disrupts protein synthesis by inducing misreading of the genetic code during translation[107]. Vancomycin specifically suppresses the synthesis of bacterial cell wall peptidoglycan that increases cell membrane permeability[107]. The enhanced membrane permeability caused by vancomycin facilitates the penetration of gentamicin into bacterial cells, which enhances the anti-bacterial action of gentamicin[107].

1.7 Current Methodologies Identifying Synergistic Combinations

The main methodology to assess pharmacological interactions is based on dose-response experiments[108]. This approach enables systematic evaluation of the effects of all possible concentrations of the combination[108]. It is convenient for high-throughput screening *in vitro*, allowing the assessment of multiple drug combinations within a single experiment (Figure 1.7A)[108]. For instance, recent

studies have utilized this approach to reveal potential combination partners for ibrutinib in the treatment of hematological malignancies[109] and to explore novel combinations for Ewing sarcoma treatment[110]. Although small-scale or hypothesis-driven combination therapies can be evaluated in *in vivo* disease models, it is required to evaluate these therapies in *in vitro* settings at the first step since the assessment of all possible combinations for a specific cancer type is infeasible[108]. Despite all endeavors, the proportion of synergistic combinations that are discovered by dose-response experiments in cell lines or animal models is limited. This underscores the need for new approaches and experimental systems to define synergistic combination therapies.

The utilization of chemical and genetic perturbation systems has paved the way for the identification of new targets and the development of novel combination therapies that achieve synergy (Figure 1.7B) [108]. Chemical libraries consist of small molecules that exhibit well-defined pharmacology and are convenient for the evaluation of drug response[111]. The application of high-throughput chemical screening to certain genomic or proteomic backgrounds enables the comprehensive evaluation of multiple biological systems simultaneously in a well-defined manner[111]. This approach is of utmost importance for the determination of the selectivity profiles of kinase inhibitors and the identification of efficacious combination therapies through the detection of synthetic lethality[111]. The applications of genetic perturbation systems in identifying novel combination therapies are explained in detail in following section.

New cellular systems have been developed to improve the translation of high-throughput drug sensitivity profiling into clinical practice for personalized treatment strategies (Figure 1.7C)[108]. Initial efforts in translational studies have focused on primary hematopoietic malignancies that offer an advantage for sampling[112]. The assessment of ex vivo drug sensitivity that measures cell viability has been successfully employed in these studies, allowing the evaluation of single-agent and combination treatments[112]. For instance, Tyner and colleagues identified translational combination therapies using ex vivo cellular systems, involving

combinations with BCL2 inhibitors for myeloid malignancies, and with PI3K and bromodomain inhibitors for lymphoid cancers[112]. These findings have contributed to the optimization of personalized treatment strategies[112].

Challenges have emerged during the sampling process of solid tumors due to their complex cellular composition and three-dimensional structure[108]. Patient-derived xenograft models have been developed to overcome some of these challenges by preserving the niche factors and tissue architecture upon successful engraftment[113]. These models have been established for various cancer types, allowing for the identification of efficacious combination treatments[108]. As an example, the administration of BRAF inhibitor encorafenib and CDK4/6 inhibitor LEE011 has achieved promising responses in the patient-derived xenograft models of colorectal cancer and non-small cell lung carcinoma[114]. However, these models have some disadvantages, including an extended duration from sampling to obtaining drug sensitivity results and the limited number of combination treatments that can be tested simultaneously[108].

The development of organoid culture systems has offered opportunities to evaluate treatment efficacy in solid cancer tissue biopsies[115]. These systems have been successfully established for various cancer types, including the esophagus, stomach, liver, pancreas, colon, and breast[115]. Clever and colleagues have pioneered the construction of a cancer organoid biobank derived from colorectal cancer, which has provided a valuable asset for compound screening[116]. Furthermore, Jabs et al. utilized high-content fluorescence microscopy to investigate the effects of single-agent and combination treatments in ovarian cancer cell monolayer cultures and organoids[117]. Their study highlighted the effect of culture conditions on drug response[117]. Current culture systems have primarily relied on small molecule libraries; however, the emergence of new compound classes and treatment strategies, such as immunotherapeutic antibodies and cellular therapies, necessitates the development of ex vivo and organoid-derived culture systems[108,118]. These systems can capture the complex cellular interactions required to develop personalized combination therapies[108].

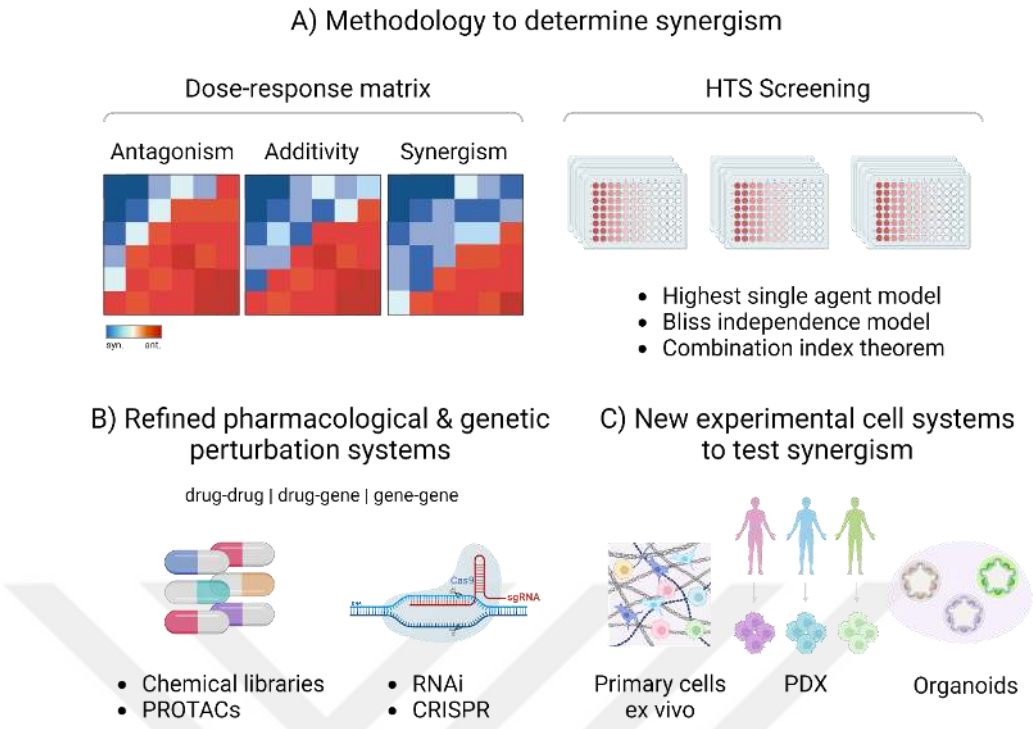

Figure 1.7: Identification of efficacious combination therapies. A. Diverse methodologies for statistical analysis and scoring synergy in drug combinations. B. Novel chemical and functional genetic approaches for identifying pharmacological interactions in drug combinations. RNAi: RNA interference, CRISPR: Clustered regularly interspaced short palindromic repeats, PROTAC: Proteolysis targeting chimera compounds. C. Novel cellular systems for discovering effective drug combinations. PDX: Patient-derived xenograft. The figure is adapted from a study by Pemovska, T., et al.[119]. and generated using biorender.com.

1.8 Functional Genomics Approaches for Investigating the Mechanisms of Synergy and Identifying New Targets in Cancer Therapy

1.8.1 Fundamental Principles of Functional Genomics Approaches

The term functional genomics encompasses various levels of biological information, including DNA (genomics and epigenomics), RNA (transcriptomics), proteins (proteomics), and metabolites (metabolomics)[82]. Each of these levels of

scientific knowledge from high-throughput studies provides invaluable tools to understand the gene function and phenotype-to-genotype relationship[82]. In this thesis, we employed RNAi and CRISPR-based functional genomics approaches which are powerful tools to dissect the mechanism of synergy in drug combinations.

1.8.1.1 RNAi Technology

The injection of double-stranded RNAs (dsRNAs) into *Caenorhabditis elegans* to silence genes established the basis for the discovery of RNAi as a powerful tool for studying gene function[120]. This technology was immediately adapted for application in mammalian cells, allowing the specific downregulation of targeted genes[121]. RNAi inhibits gene translation via cleaving or suppressing messenger RNA (mRNA) using short RNA sequences that are complementary to the mRNA[82]. The process can be initiated by endogenous microRNAs (miRNA), synthetic exogenous small interfering RNAs (siRNA), and short hairpin RNAs (shRNA)[122,123]. Precursor forms of miRNA and shRNA are processed in the nucleus by the Drosha protein, and then exported to the cytoplasm[82,124]. In the cytoplasm, these structures are further trimmed by an enzyme called Dicer to generate miRNA, shRNA, or siRNA[125]. Dicer associate with RNA-induced silencing complex (RISC) which cleaves the passenger strand and becomes active when loaded with a single-stranded RNA (ssRNA) molecule[126]. The ssRNA serves as a guide to target complementary mRNA sequences, which results in mRNA degradation and inhibition of protein translation (Figure 1.8)[82]. By combining multiple siRNAs or shRNAs, numerous genes can be simultaneously targeted in an unbiased manner[127]. RNAi screens have been extensively utilized to study gene functions related to cell proliferation, survival, and death in response chemotherapy[128]. In this study, we utilized an RNAi-based signature approach encompassing eight different shRNAs to investigate drug mechanisms of action, as explained in section 1.8.2.2.

1.8.1.2 CRISPR-Cas9 System

CRISPR system and its associated Cas proteins establish an adaptive immune system in bacteria and archaea[129]. This system encodes sequence information from viruses and utilizes it for defense against pathogens[129]. Researchers have exploited the potential of the CRISPR/Cas system to build a ground-breaking genome editing tool by engineering it to target DNA from other species[130]. Various CRISPR/Cas systems have been identified[131]. Among these, CRISPR system with Cas9 enzyme from *Streptococcus pyogenes* has been extensively studied[132]. When guide RNA (gRNA) and Cas9 protein are simutaneously expressed in the cell, they form a ribonucleoprotein (RNP) complex that scans the target DNA for Cas9-binding sites known as protospacer adjacent motifs (PAMs)[133]. Upon binding to the PAM sequence, Cas9 undergoes a conformational change, allowing for precise base pairing between the gRNA and target DNA[133]. The perfect annealing between gRNA and the target activates the catalytic centers of Cas9, which then induce a double-strand break at the target site by creating blunt ends[133]. As a result, it leads to the silencing of the target gene[133]. The mechanisms of RNAi technology and the CRISPR/Cas9 system are illustrated in Figure 1.8.

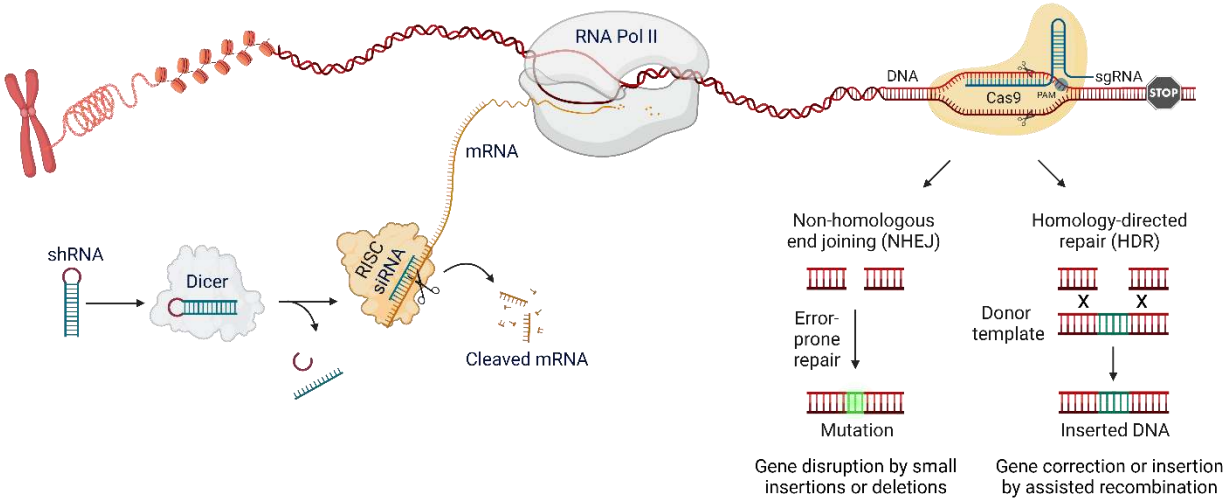

Figure 1.8: Fundamental principles of RNAi and CRISPR approaches. RNAi involves gene silencing through the action of endogenous miRNA or exogenous siRNA or shRNAs. Pre-dsRNA molecules are fragmented by Dicer, and the guide strand associates with the RNA-induced silencing complex (RISC) to target and degrade complementary mRNA sequences. CRISPR utilizes the Cas9 enzyme with a partially-annealed single guide RNA (sgRNA) molecule to scan DNA for specific motifs. Cas9 induces double-strand breaks (DSBs) at the target sites, which can be repaired through homology-directed repair (HDR) or non-homologous end joining (NHEJ). The figure is adapted from by a study from Cetin, R., et al.[82] and generated using biorender.com. The part illustrating NHEJ and HDR repair systems is obtained from a BioRender poster titled *"A tool for genome editing: CRISPR – Cas9"* (Cress, B., Lee, J. H., Bardet, L., *et al.*).

1.8.2 Uncovering Mechanisms of Action, Chemotherapy Resistance, and Potential Drug Targets in Cancer Therapy Using Functional Genomics

This section covers the applications of functional genomics approaches to provide biological insight into the mechanism of action of anti-cancer agents, chemoresistance mechanisms, and identification of potential drug targets in cancer.

1.8.2.1 RNAi and CRISPR Screening Approaches

Genome-wide CRISPR screens have played a significant role in uncovering the mechanisms of resistance to many anti-cancer agents. For instance, individual agents and dual combinations of the R-CHOP regimen (the combination of rituximab, cyclophosphamide, doxorubicin, vincristine, and prednisone) were investigated using genome-wide CRISPR screens, to reveal the cross-resistance factors in diffuse B-cell lymphoma cells[134]. The ABC multidrug resistance transporter genes including ABCC1, ABCG2, and ABCB1 were identified, which confirmed the previous studies on chemoresistance mechanisms[134,]. Moreover, hydroxy-daunomycin target gene TOP2 was shown as a primary contributor to hydroxy-daunomycin resistance, which is also correlated with previous CRISPR screens[135]. These findings align with a pooled RNAi screen that identified TOP2A as a major determinant of doxorubicin resistance[136]. Lamba's group employed Brunello CRISPR knockout library in the K562 CML cell line under etoposide treatment and identified that ABCC1 knockout enhanced the etoposide toxicity[137]. The same group also discovered the association between the expression levels of DNA damage repair helicase RAD54L2 and etoposide resistance[137,138].

Despite that the genome-wide CRISPR screens are valuable tools to understand the key dependencies for chemoresistance in cancer cells, performing genome-scale perturbation screens to map these dependencies is challenging due to the limited number of drug-resistant cell model panels[82]. To overcome these limitations, Ha et al. conducted a proof-of-concept study by targeting the MDR1 gene via CRISPR in doxorubicin-resistant breast cancer cells[139]. This modification successfully restored the susceptibility of these cells to doxorubicin treatment[139]. Similarly, Wang et al. focused on the urokinase plasminogen activator receptor, a gene frequently overexpressed in cancer cells[140]. Genetic ablation of this receptor in endocervical and colorectal adenocarcinoma cell lines reduced the resistance against multiple drugs, including 5-fluorouracil, cisplatin, docetaxel, and doxorubicin[140].

A genome-wide CRISPR screen identified a mismatch repair gene MSH2 as a main component of cisplatin resistance in bladder cancer[141]. Gene ontology analysis of mostly enriched genes revealed the mismatch repair pathway as a critical contributor to cisplatin resistance[141]. Moreover, the enhanced expression of MSH2 and MLH1, members of the mismatch repair pathway, caused an increase in cisplatin resistance[141]. These results support the effectiveness of the whole-genome CRISPR screens and confirm the relationship between the genes identified and cisplatin resistance.

A comprehensive siRNA screen targeting 645 human kinases discovered several kinases of which knockdown enhanced gemcitabine-induced apoptosis in MiaPaCa2 pancreatic cancer cell line[142]. Silencing of kinases in PI3K/Akt/mTOR pathway decreased the cell survival upon gemcitabine treatment[142], confirming previous studies indicating the involvement of this pathway in gemcitabine resistance[143,144]. In addition, checkpoint kinase 1 (CHEK1) was revealed as a prominent candidate, compatible with its crucial role in DNA damage repair pathway[142]. Following this finding, another group demonstrated that CHEK1 knockdown in MiaPaCa2 cells elicited enhanced sensitivity to gemcitabine treatment[145]. Moreover, a synthetic lethality screen in another pancreatic cell line using an shRNA library targeting 10000 genes showed decreased cell viability in CHEK1-knockdown cells under gemcitabine treatment[146]. These findings suggested the presence of the same mechanism in a broader range of cell types.

Genome-scale gene knockdown and knockout screens have also been utilized to uncover factors that contribute to resistance and susceptibility to mitotic agents[82]. White and colleagues performed a genome-wide RNAi screening approach in human non-small cell lung cancer cells under paclitaxel treatment to identify synthetic lethal drug-gene relationships[147]. They identified multiple proteins involved in microtubule function and dynamics, as well as core proteasome components[147]. Following this study, another group employed CRISPR screening in HAP1 CML cell line to discover loss-of-function mutations that lead to resistance against paclitaxel, along with 26 other anti-cancer drugs[148].

This study revealed that the previously uncharacterized open reading frame C1orf115 which harbors the DUF4710 domain with an unknown function that confers resistance to paclitaxel, vincristine, and cladribine – a purine analog[148]. This finding suggests that C1orf115 may represent an uncharacterized multidrug resistance gene[82].

1.8.2.2 RNAi-based Signature Approach

Data-driven classification has been a valuable approach to enlighten mechanistic actions of novel anti-cancer agents[149]. Many research groups have used different model organisms and cell line models to generate molecular and phenotypic signatures of drug mechanisms of action[150–152]. However, the number of studies that uses data-driven approaches to annotate drug mechanisms of action has been limited[149]. A robust pipeline that integrates the molecular signatures of agents has been needed to predict drug mechanisms of action accurately. To address this requirement, Pritchard et al. developed an shRNA-based signature approach that annotates drugs based on their signatures[149].

The shRNA-based signature approach utilizes supervised and unsupervised learning models that are connected by network-based statistics[149]. It predicts drug mechanisms based on the trained model and reveals novel mechanisms of action which are not present in the trained model[149]. Incorporating new mechanisms identified into the training set allows the prediction of various examples that might belong to these new categories[149]. Therefore, it provides both statistical and biological generalizations of agents[149]. By utilizing the shRNA-based signature approach, the Hemann group demonstrated that oxaliplatin causes stress in ribosome biogenesis that induces cell death as opposed to other platinum-derived anti-cancer agents, such as cisplatin and carboplatin, which kill cancer cells by triggering DNA-damage response[153]. The difference between the mechanisms of action of oxaliplatin and other platinum-derived agents can explain the distinct clinical efficacies of these agents in different cancer types. This finding has also been confirmed by other studies[154,155]. This indicates that the shRNA-based

signature approach is a powerful tool to discover unknown drug mechanisms of action.

Based on the value of CRISPR or shRNA-based functional genomics approaches in the delineation of mechanisms of drug action and chemoresistance, we used these approaches in this thesis to investigate the mechanism of synergism for the molecular-targeted agent-conventional chemotherapeutic combinations in gastric cancer cell models.

2. MATERIALS and METHODS

2.1 Cell Culture and General Reagents

AGS, SNU1, SNU5, SNU16, SNU484 and NCI-N87 gastric adenocarcinoma cell lines were obtained from American Tissue Type Culture Collection (USA). Gastric adenocarcinoma cell lines were grown in RPMI media (Corning, USA) supplemented with 10% fetal bovine serum (FBS) (Gibco, USA) and 1% Penicillin-Streptomycin (P/S) (Gibco, USA). Eμ-Myc Cdkn2a$^{Arf-/-}$ leukemia cell line was grown in B-cell media (BCM) composed of DMEM and IMDM media supplemented with 10% FBS, 1% P/S and 0.1% 2-mercaptoethanol (Gibco, USA). Lenti-X cells were cultured in DMEM media (Corning, USA) supplemented with 10% FBS and 1% (P/S). Doxorubicin, epirubicin, cisplatin, 5-fluorouracil, and paclitaxel were purchased from European Directorate for the Quality of Medicines and HealthCare (France). SN38, erlotinib, gefitinib, lapatinib, osimertinib, afatinib, everolimus, and JNJ-38877605 were purchased from Sellekchem (USA). Cell death inhibitors including Z-VAD-FMK, Z-VAD-IETD, ferrostatin, rucaparib, and necrostatin were obtained from ApexBio (USA). Thiazolyl blue tetrazolium bromide (MTT) was purchased from Sigma-Aldrich (USA). Primary antibodies used in immunoblotting experiments are anti-B-actin (Sigma-Aldrich, USA), anti-EGFR (CST, USA), anti-phospho-p44/42 MAPK (Erk1/2) (Thr202/Tyr204) (CST, USA), and anti-ABCG2 (CST, USA). Primary antibodies and reagents used in flow cytometry analyses include anti-cleaved-caspase3 (BD Pharmingen), anti-cleaved-PARP (Asp214) (BD Pharmingen), anti-phospho-histone H2A.X (Ser129) (Millipore, USA), propidium iodide (Invitrogen, USA), and Hoechst-33342 (Thermo Scientific, USA), RnaseA (Sigma Aldrich, USA).

2.2 Drug Response Experiments

2.2.1 Anti-cancer Agents

Dual combinations of five different conventional chemotherapeutics from anthracyclines, platinum derivatives, taxanes, fluoropyrimidines, and

topoisomerase inhibitors with three different molecular-targeted agents were simultaneously applied to gastric adenocarcinoma cell lines (Figure 2.1). Doxorubicin, cisplatin, 5-fluorouracil, paclitaxel, and irinotecan, which stand out in treating gastric cancer were selected as conventional chemotherapeutics. Molecularly targeted agents used in the study were erlotinib, everolimus, and JNJ-38877605, which target EGFR, mTOR, and c-MET, respectively.

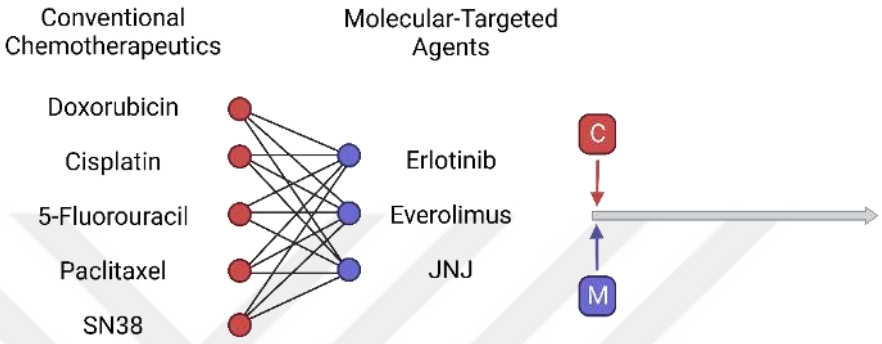

Figure 2.1: Drug pairs. The dual combination of molecular-targeted agent-conventional chemotherapeutics was tested in each cell line via simultaneous application. JNJ: JNJ-38877605.

The Compusyn program developed by Chou and Talalay was used to calculate combination index (CI) values to quantitatively define synergism (CI<1), additivity (CI=1), and antagonism (CI>1) in concomitant applications. Fraction-affected (fa) values calculated based on the percent viability in control and treatment groups, then normalized to 1, were entered into the program along with the corresponding doses. Fa values derived from the results of MTT cell viability experiments (see section 2.2.2) provided information about the size of cell population affected by the treatment(s). The most synergistic drug pair was selected from the initial drug pair screen for further analysis.

2.2.2 MTT Assay

MTT cell viability assay is used to evaluate cell survival as a response to the treatment, based on the conversion of MTT into formazan crystals by living cells. Briefly, cells at appropriate numbers were seeded in 96-well flat-bottom cell culture plates (Corning,USA) 24 hours before the experiment. Cells were subject to at least seven different concentrations of each agent and the combination. After five days of incubation, 3 mg/ml MTT was added to each well and incubated for 4 hours in the dark. Formazan crystals, the reduced form of MTT, were dissolved with 13.8% SDS solution (Bio-Rad, USA) containing 1% HCl by shaking plates overnight at room temperature, and the absorbance was measured at 570 nm by a microplate reader (Synergy H1, Biotek). The percent cell viability for each concentration was calculated by normalizing the signal to the control group. This protocol was followed to analyze the drug response of single-agent treatments and simultaneous applications (Figure 2.1). The sigmoidal dose-response curve (DRC) of each treatment was plotted using four-parameter logistic regression to identify plateau, hill slope, EC_{max}, and EC_{50} in GraphPad Prism7.

2.2.3 FLICK Assay

Richards et al. optimized a plate-reader-based assay called fluorescence-based and lysis-dependent inference of cell death kinetics (FLICK) which specifically quantifies cell death and enables the direct quantification of death kinetics[156].

One of the most critical components of the FLICK assay is SYTOX green nucleic acid dye, which is impermeant to live cells, acting as an indicator of dead cells. SYTOX dye (Invitrogen, USA) at a final concentration of 5 μM was added into wells with the treatment of interest. Since it is a highly stable dye, this enables the monitorization of the cell death kinetics throughout the assay. Cells were seeded at a density of 2000-2500 cells/well in 96-well plates in the presence of SYTOX and treated as explained in the MTT assay protocol. The data was collected by measuring kinetic reads of the SYTOX signal using a microplate reader (Tecan Spark or Tecan M1000) throughout five days, the assay length

previously used in the MTT assay. Cells were exposed to 0.1% Triton-X (Thermo Scientific, USA) for lysis at the end of the experiment, from which total population size was inferred in the presence of SYTOX. In addition to experiment plates, a plate called '*T0*' was also prepared for the lysis of the cells at the beginning of the experiment without any treatment, used to determine the initial size of the cell population. The exponential growth modelling of population sizes at the initial and end time points was used to infer the total population size at intermediate time points. Dead population sizes represented by SYTOX signal and total population sizes were used to calculate the size of live populations at each concentration. Calculations of fractional viability (FV), relative viability (RV), the lethal fraction (LF), and normalized growth rate inhibition (GR) values were performed using the information on live, dead, and total populations (Figure 2.2). The experiment steps are summarized in Figure 2.3. The MATLAB data analysis code is available in the GitHub repositories (MJLee-Lab/fitGrowth; MJLee-Lab/fitLED; MJLee-Lab/fit_via)[156].

$$FV = \frac{Live}{Live + Dead} \qquad RV = \frac{Live_{treated}}{Live_{untreated}} \qquad GR = 2^{\left(\frac{\log_2\left(\frac{Live_{treated}}{Live_{T0}}\right)}{\log_2\left(\frac{Live_{untreated}}{Live_{T0}}\right)}\right)} - 1$$

$$LF(t) = LF_0 + (LF_p - LF_0) * (1 - e^{-D_R(t-D_0)})$$

Figure 2.2: Formulations for FV, RV, GR, and LF models. Parameters of the LF model include LF_0 (the starting lethal fraction), LF_p (the death plateau), D_0 (the death onset time), and D_R (the maximum rate of death)[156].

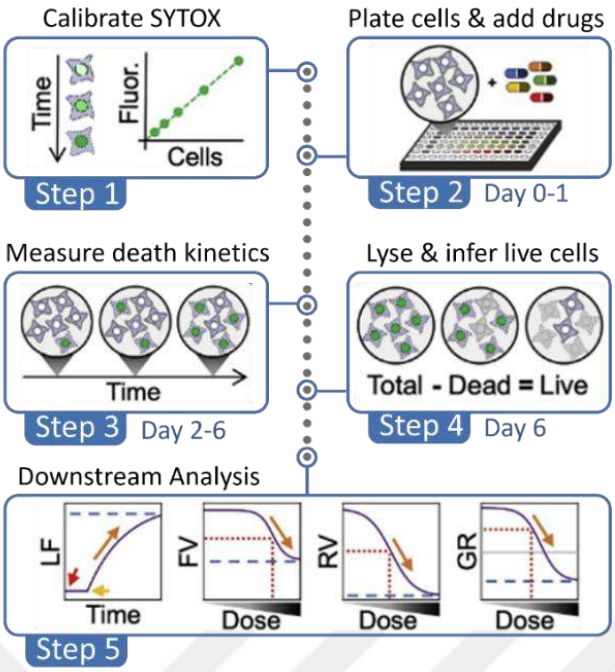

Figure 2.3: Summary of steps in FLICK assay. Summary of steps in FLICK assay. LF: Lethal fraction.

Serially diluted cells were seeded at different numbers in the presence of SYTOX to optimize gain values for the fluorescence measurements and the period for Triton-X permeabilization. Cells were lysed with 0.1% Triton-X at the final, and measurements were taken using gain values ranging from 100 to 150. The exposure of cells to Triton-X for 2-3h at 37°C and 5% CO_2 permeabilized the cell membrane, and the fluorescence signal did not drastically change with the extended exposure period (Figure 2.4).

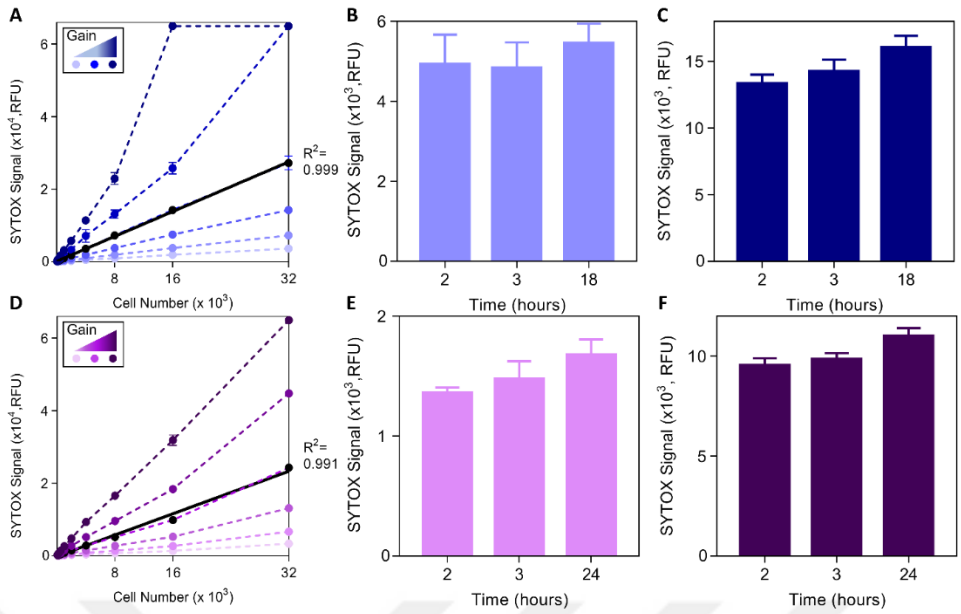

Figure 2.4: Example results of the FLICK optimization experiments. A. Fluorescence measurements at different gain settings in AGS cells. B. and C. Change in SYTOX signal at low and high numbers of AGS cells after different exposure periods to Triton-X, respectively. D. Fluorescence measurements at different gain settings in SNU5 cells. E. and F. Change in SYTOX signal at low and high numbers of SNU5 cells after different exposure periods to Triton-X. The gain value was set to 130 for both cell lines since cell number and SYTOX signal were linearly well correlated.

2.3 Quantitative Immunoblotting

1-1.5 million cells were seeded in 10-cm dishes and incubated overnight at 37°C, 5% CO_2 in a humidified incubator. Cells were collected the next day to assess the knockout of the gene of interest or treated with EGFR inhibitors including erlotinib, gefitinib, lapatinib, osimertinib, and afatinib at 10µM in a time-dependent manner and collected at indicated time points. Pellets were washed with ice-cold PBS and lysed in SDS-lysis buffer (50mM tris-HCl, 2% SDS, 5% glycerol, 5mM EDTA, 1mM NaF, 10mM β-GP, 1mM phenylmethylsulphonyl-floride, 1mM Na3VO4, and protease and phosphatase inhibitor tablets) at volumes depending on pellet sizes. Lysate concentration was determined using the Pierce BCA Protein Assay following the manufacturer's instructions (Thermo Fisher

Scientific, USA) and normalized to the same protein concentration. Proteins were separated by running samples either on 4-15% precast TGX gels (Bio-Rad, USA) or on 10% hand-poured SDS-PAGE gels. Gels were transferred to nitrocellulose membranes which were then blocked in 50% PBS:50% Intercept Blocking Buffer (IBB, LI-COR Biosciences, USA) solution on a shaker at room temperature for 1h. Membranes were incubated with primary antibody diluted 1:1000 in 50% PBS-T (0.1% Tween in PBS):50% IBB at 4°C overnight. The next day, membranes were washed three times for 5 mins in PBS-T and incubated with secondary antibodies (LI-COR, USA) diluted 1:15000 in 50% PBS-T:50% IBB at room temperature for 1h. Immunoblots were then washed three times for 5 mins in PBS-T and visualized using LI-COR Odyssey CLx scanner. Band intensities were quantified using ImageJ software, and the protein of interest was normalized to internal loading control.

2.3 Flow cytometry

Cell cycle progression, apoptotic activity, and DNA damage profile were assessed using flow cytometry-based analysis.

Cells were collected via centrifugation at 1500 rpm for 5 mins at the indicated time points to evaluate cell cycle progression in the presence and absence of drug of interest. Pellets were washed in ice-cold PBS and fixed in ice-cold 70% ethanol. Samples were stored at -20°C. On the day of analysis, each sample was then washed twice in ice cold PBS and resuspended in 10% Rnase A in PBS. Propidium iodide at a final concentration of 0.5mg/ml was added to each sample, and analysis was performed using LSRII or Miltenyi MACSQuant VYB flow cytometers.

The evaluation of apoptotic activity was performed by quantifying cleaved-caspase3 and cleaved-PARP levels. Cells were collected as mentioned above and fixed in 4% formaldehyde solution in PBS at room temperature for 15 mins. After washing once with cold PBS, samples were fixed in ice-cold 100% methanol and stored at -20°C. On the experiment day, methanol was removed, and pellets were washed twice with PBS-T. Each sample was incubated with primary cleaved-

caspase3 antibody diluted 1:500 in 50% PBS-T:50% IBB at room temperature. After 8h, samples were washed once with PBS-T and then incubated with primary cleaved-PARP-647 antibody and goat anti-rabbit Alexa-488 (both diluted 1:250 in 50% PBS-T:50% IBB) overnight at room temperature. Each sample was washed twice with PBS-T the following day and analyzed using Miltenyi MACSQuant VYB.

DNA damage was profiled through the quantification of phospho-H2AX level in a cell cycle-dependent manner. Cells were collected and fixed, as mentioned above. After removing methanol and washing once with PBS, samples were incubated with primary phospho-H2AX antibody diluted 1:200 in 50% PBS-T:50% IBB at room temperature for 8h. Each sample was then washed once with PBS-T and incubated with goat anti-mouse Alexa-488 diluted in 1:250 50% PBS-T:50% IBB overnight at room temperature. The following day, samples were washed once with PBS and resuspended in 10% Rnase A in PBS. Propidium iodide was added to each sample at a final concentration of 0.5mg/ml, and analysis was performed using LSRII or Miltenyi MACSQuant VYB flow cytometers. Data analysis of all flow cytometry-based experiments was performed using FlowJo software.

2.4 Generation of SNU5$^{EGFR\text{-}KO}$

SNU5$^{EGFR\text{-}KO}$ single-cell clones were generated in two steps. First, SNU5 cells expressing Cas9 (SNU5-Cas9) were generated. lentiCas9-Blast (Addgene, USA) plasmid was packaged into viruses in lenti-X cells. For this purpose, 3.5 million lenti-X cells were seeded into a 10 cm dish and allowed to adhere overnight. VSVG and psPAX2 packaging vectors and the equimolar amount of lentiCas9-Blast were diluted in OptiMEM. It was mixed with lipofectamine 2000, diluted in OptiMEM, then incubated at room temperature for 15 minutes. The mixture was dropped onto lenti-X cells and incubated for 6 hours. The medium was then replaced by fresh medium, and virus collection was performed after 24 and 48 hours. All media containing lentiviral particles were combined, centrifuged, and filtered with a 0.45μm filter. The media were aliquoted

and stored at -80°C for long-term storage. SNU5 parental cells were transduced with viruses containing lentiCas9-Blast by centrifuging at 830xg at 32°C for 90 minutes in the presence of polybrene (4ug/ml at the final concentration), and then the media were replaced by fresh media. SNU5-Cas9 cells were selected by blasticidin (10µg/ml) treatment (Figure 2.5A).

Three different single guide RNAs (sgRNA) were designed and cloned into the lentiGuide-puro (Addgene, USA) vector. Plasmids were transformed into Stbl3 bacteria, then spread over agar plates containing ampicillin. Two colonies for each plasmid were selected and grown in an ampicillin-containing LB Broth liquid culture. After 16h of incubation, plasmids were isolated using a plasmid isolation kit (MN NucleoSpin) following the manufacturer's instructions. All plasmids were verified by sequencing (primer: 5'-GACTATCATATGCTTACCGT-3'). Plasmids were packaged into lentiviruses, and SNU-Cas9 cells were infected with viruses containing either EGFR-targeting or non-targeting sgRNA plasmids. SNU5-Cas9 cells expressing sgRNA were selected by puromycin treatment (2µg/ml). Viral packaging and transduction were performed by following protocols explained above. Cells were grown, and the knockout efficiency in total population was evaluated via immunoblotting (Figure 2.5B). VSVG, psPAX2, lentiCas9-Blast and lentiGuide-puro plasmids were kindly gifted by Tugba Bagci Onder's group.

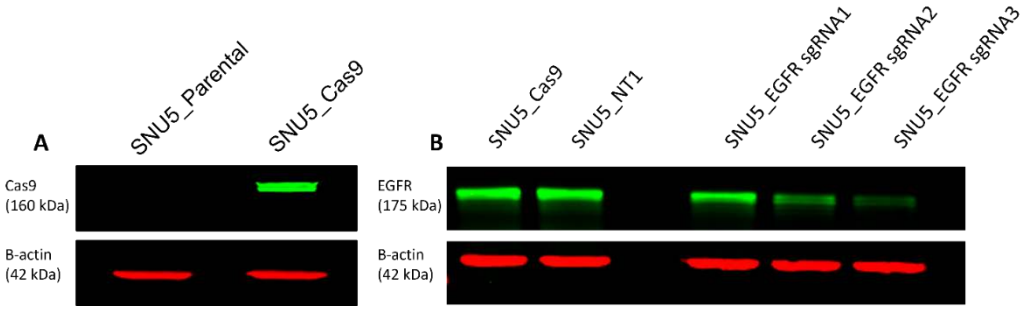

Figure 2.5: Evaluation of Cas9 and EGFR expression via immunoblotting. A. Confirmation of Cas9 expression in SNU5 cells. B. Evaluation of knockout efficiency in total population transduced with three different EGFR-targeting sgRNA constructs. sgRNA: single guide RNA. NT: Non-targeting.

As shown in Figure 2. 5B, EGFR expression was substantially decreased in SNU5-EGFR-sgRNA3 cells compared to SNU5-Cas9 cells and SNU5-NT1 cells. Despite the efficient decrease in the expression of EGFR, there were still some cells in the population expressing EGFR, which might result from the knockout of only one allele of the EGFR gene. These cells have the potential to dominate the population over time. For this reason, single-cell clones from SNU5-EGFR-sgRNA3 cell population were generated to obtain EGFR double-knockout cell line(s), and EGFR expression in these clones was assessed by immunoblotting. Selected clones were further validated by Sanger sequencing (sequencing primer: 5'-AATTTAAAGACTCACTCTCC-3')

2.5 A Genome-wide CRISPR Screening

A genome-wide CRISPR screening was performed to have deep insight into the mechanistic action of SN38 and erlotinib combination compared to the SN38-only treatment. In line with this purpose, CRISPR screening was coupled with Annexin V-conjugated bead sorting experiment to actively separate dead and live cells.

2.5.1 Optimization Steps

Three optimization experiments were conducted (1) to determine the equipotent doses of combination and SN38-only treatments, (2) to understand the effectiveness of annexin V-conjugated bead sorting in separating live and dead populations, and (3) to calculate the multiplicity of infection (MOI) of the library used. Drug response experiments showed that combination induced more efficacious response than SN38-only treatment when both treatments were applied at equimolar concentrations. However, in this case, it is hard to understand whether the presence of erlotinib leads combination to induce cell death by acting on a different pathway than SN38-only treatment or only causes increased activation of the same pathway(s) triggered by SN38. Therefore, the application of equipotent concentration of both treatments was required to solely investigate the possible differences in the mechanisms of action. For this reason, we optimized the equipotent concentrations of SN38-only and the combination. Cells were seeded

into 12-well plates and treated with three different equipotent concentrations of each treatment, which were inferred from FV curve fitting data. The number of both dead and live cells was determined by cell counting with a hemacytometer from day0 to day5. This experiment revealed the general trend of change in live/dead cell number and FV over time. It was also repeated in 10 cm plates only for day3 at the selected concentrations to evaluate the effect of culture size.

The annexin V-conjugated magnetic bead sorting efficiency was assessed to optimize the initial population size required to obtain live and dead populations with 500x coverage for next-generation sequencing (NGS). SNU5 cells were treated with either SN38 only or combination at equipotent concentrations. After three days, cells were labeled with annexin V-conjugated beads (Miltenyi, USA) following the manufacturer's instructions and loaded into the magnetic columns. The unlabelled live fraction was collected by flow-through, and the dead fraction positive for annexin-V was eluted from columns. Annexin-V positivity was also evaluated using flow cytometry by staining cells with PE-conjugated annexin-V.

To determine the MOI of the library, 2.5 million SNU5 cells were seeded into each well of 12-well plates and incubated with the dilution series of the library in the presence of polybrene for 6 hours at 37°C and 5% CO_2. The library infection was performed by incubation only since it was previously realized that spinfection causes the accumulation of cells at one side of wells, which can significantly affect the distribution of the library. Cells were then replated with fresh media. After 24 hours, puromycin (2µg/ml) selection was initiated for cells infected with one of the virus dilution series, and fresh media was added to the other. The number of live cells was determined for all series at the end of the selection. The virus volume that resulted in 30% survival in puromycin-selected cells compared to control cells was calculated to achieve the final MOI of 0.3.

2.5.2 Experimental Procedure

A genome-wide CRISPR screening was performed using **T**oronto **K**nock**O**ut Library **v3** (TKOv3) including 71090 single guide RNA (sgRNA) (70948 sgRNA targeting 18053 protein-coding genes (4 sgRNA/gene) and 142 control non-targeting sgRNA against EGFP, LacZ and luciferase)[157]. >300x10^6 SNU5-Cas9 cells were infected with TKOv3 library to achieve 500x coverage by following the protocol used in the MOI optimization experiment and selected via puromycin treatment. Cells were then taken into fresh media and further expanded to reach approximately 300-400 coverage for the experiment. On day 1, 90x10^6 and 50x10^6 cells were plated in duplicate for each treatment and untreated condition, respectively. 50x10^6 cells were collected and frozen in duplicate for the T0 controls. Cells were treated with either SN38 only (13.5nM) or combination (3.7nM SN38 + 370nM Erlotinib) on day0. On day2, all experiment groups were passaged by maintaining culture conditions. Live and dead fractions of treatment groups were separated using annexin V-conjugated magnetic bead sorting on day3.

Genomic DNA of all treatment, control, and T0 group replicates was extracted using a genomic DNA purification kit (Promega, USA) according to the manufacturer's instructions. The amount of DNA was determined for all samples by nanodrop and Qubit. TKOv3 CRISPR sequencing library was prepared by performing a two-step PCR reaction. The first reaction (PCR1) was established to enrich the guide RNA regions in the genome and the second reaction (PCR2) was to amplify guide RNAs with Illumina TruSeq adapters with i5 and i7 indices. These indices are unique sequences that are added to the DNA of each sample in

different combinations during library preparation to allow the pooling of all samples during multiplex sequencing. Primer sequences are shown in Table 2.1.

PCR 1 – Primer Sequences	
pLCKO2 forward primer	GAGGGCCTATTTCCCATGATTC
pLCKO2 reverse primer	CAAACCCAGGGCTGCCTTGGAA
PCR 2 – i5 and i7 Index Primer Sequences for Illumina Sequencer	
PCR 2 – i5 forward primers	Illumina adapter / i5 barcode / Insert annealing sequence
S501-F	AATGATACGGCGACCACCGAGATCTACACTAGATCGCACACTCTTTCCCTACACGACGCTCTTCCGATCTTTGTGGAAAGGACGAGGTACCG
S502-F	AATGATACGGCGACCACCGAGATCTACACCTCTCTATACACTCTTTCCCTACACGACGCTCTTCCGATCTTTGTGGAAAGGACGAGGTACCG
S503-F	AATGATACGGCGACCACCGAGATCTACACTATCCTCTACACTCTTTCCCTACACGACGCTCTTCCGATCTTTGTGGAAAGGACGAGGTACCG
PCR 2 – i5 forward primers	Illumina adapter / i5 barcode / Insert annealing sequence
D701-R	CAAGCAGAAGACGGCATACGAGATCGAGTAATGTGACTGGAGTTCAGACGTGTGCTCTTCCGATCTACTTGCTATTTCTAGCTCTAAAAC
D702-R	CAAGCAGAAGACGGCATACGAGATTCTCCGGAGTGACTGGAGTTCAGACGTGTGCTCTTCCGATCTACTTGCTATTTCTAGCTCTAAAAC
D704-R	CAAGCAGAAGACGGCATACGAGATGGAATCTCGTGACTGGAGTTCAGACGTGTGCTCTTCCGATCTACTTGCTATTTCTAGCTCTAAAAC
D705-R	CAAGCAGAAGACGGCATACGAGATTTCTGAATGTGACTGGAGTTCAGACGTGTGCTCTTCCGATCTACTTGCTATTTCTAGCTCTAAAAC

Table 2.1: Primers used in PCR1 and PCR2 reactions of CRISPR screening.

The optimization experiment was performed to determine the amount of genomic DNA and the cycle number for PCR1, not to saturate the reaction. This is explained in the result part in detail. Analysis of agarose gel images was performed on Image Lab software. Reaction volumes and thermocycler settings for PCR1 and PCR2 are given in Table 2.2.

A

PCR1	1X
2X polymerase master mix	25 µl
10µM PCR1 forward primer	2.5 µl
10µM PCR1 reverse primer	2.5 µl
Genomic DNA	2.5 µg
Water	up to 50 µl
Total	50 µl

Step	Temperature	Time	
1	98°C	30 sec	
2	98°C	10 sec	23 cycles
3	66°C	30 sec	
4	72°C	15 sec	
5	72°C	2 min	
6	10°C	Hold	

B

PCR2	1X
2X polymerase master mix	25 µl
10µM i5 forward primer	2.5 µl
10µM i7 reverse primer	2.5 µl
PCR1 product	5 µl
Water	up to 50 µl
Total	50 µl

Step	Temperature	Time	
1	98°C	30 sec	
2	98°C	10 sec	10 cycles
3	55°C	30 sec	
4	65°C	15 sec	
5	65°C	5 min	
6	10°C	Hold	

Table 2.2: Experimental conditions in PCR1 and PCR2. A. Reaction volumes (left) and thermocycler setting (right) for PCR1. B. Reaction volumes (left) and thermocycler setting (right) for PCR2.

50µl of each PCR1 reaction per sample was pooled and mixed, and then 5µl of PCR1 product was run on 1% agarose gel to check the quality of the 600bp product. PCR2 reaction in 50µl yielding 200bp product was established for each sample, and the product was run on 2% agarose gel. 200bp product was excised, and DNA was purified from agarose gel using a gel extraction kit following the manufacturer's instructions. The experimental workflow of CRISPR screening is illustrated in Figure 2.6.

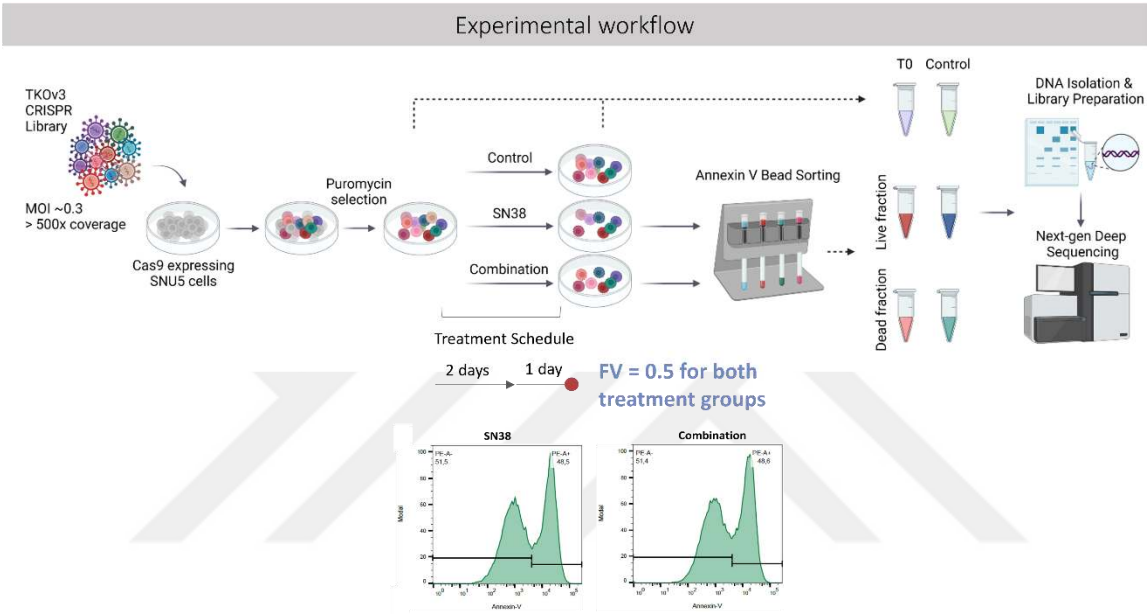

Figure 2.6: Experimental workflow of the genome wide CRISPR screen.

2.5.3 Analysis

Reads of each sequenced library were demultiplexed by using the barcode splitter and trimmer functions of the FASTX toolkit. Reads from each condition were mapped to the TKOv3 library using Bowtie2 read alignment tool. A parametric fit of DESeq2 was used to determine the log2(fold change) for each comparison of interest. The 1000 nontargeting sgRNA controls were then randomly assigned to set of four "genes". Guide-level scores were transformed into the single gene-level fold change by calculating the mean of all sgRNAs. Fold change at the gene level were *z*-scored based on the mean and standard deviation of nontargeting genes. Empiric *p* values were calculated from *z*-scored fold changes by bootstrapping guide-level scores, which then false discovery rate

(FDR)-corrected using the Benjamini-Hochberg procedure for statistical robustness. This analysis pipeline was selected from a set of methods tested in parallel that involve the log2(fold change) calculation of each comparison using trimmed or raw sgRNA counts in DESeq2 and the estimation of gene-level scores from sgRNA level fold change values with different analysis streams. All analysis steps are summarized in Figure 2.7. Candidate hit genes were identified using dead *vs* live comparisons of SN38 only and combination treatment groups to enlighten the differences in death mechanisms under these treatments.

Gene Set Enrichment Analysis (GSEA) was performed using GSEA 4.2.3. GSEA Pre-ranked tool was utilized to identify signatures that show significant enrichment or depletion using rank-ordered gene level fold changes of dead cells compared to live cells under both treatments. Significance was determined by 1000 gene set permutation. All gene expression signatures within Molecular Signature Database (MSigDB) related to our data were tested. Leading Edge Analysis in GSEA was run to examine the core member(s) of high-scoring gene sets in Gene Ontology Biological Process (GO-BP) that contribute to the enrichment score and determine the correlation between the top ten gene sets. All data analysis of screen results and statistical tests was performed using MATLAB unless otherwise mentioned.

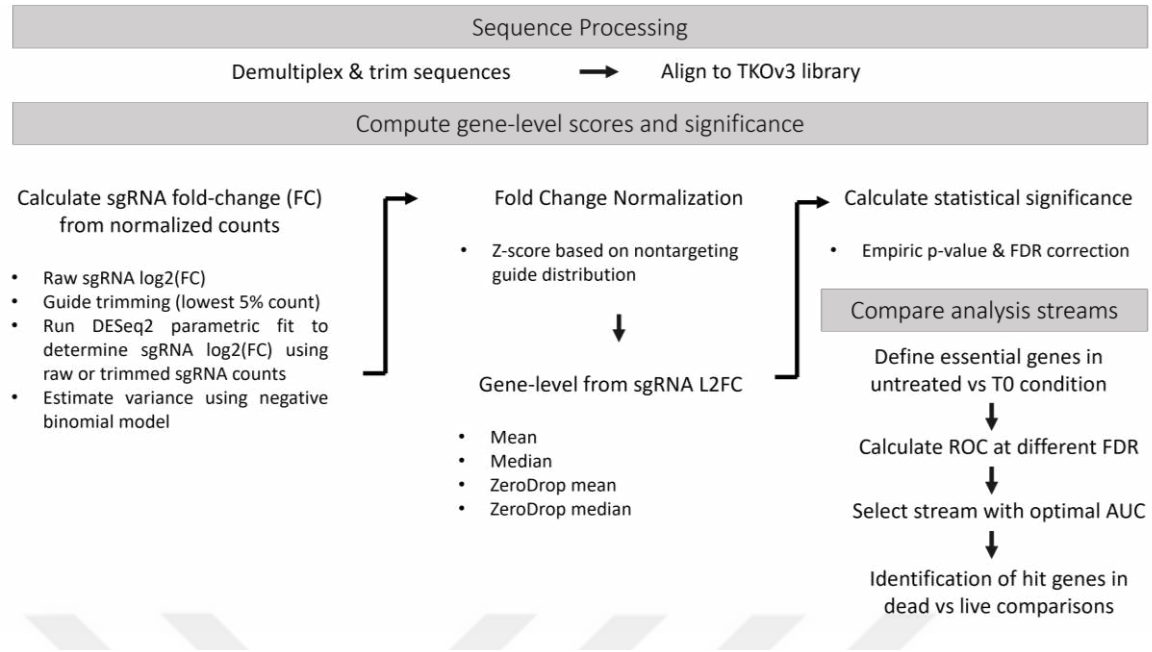

Figure 2.7: Analysis workflow of the genome wide CRISPR screen. The schematic representation is adapted from Cruz-Gordillo *et al.*[158] FC: fold-change. L2FC: Log2 fold-change.

2.6 Validation of CRISPR Screening

Three different validation assays were performed to confirm CRISPR screening results, including FLICK and annexin-V+ assays, described above, and the competition assay explained in this section.

All sgRNAs targeting selected candidate hit genes were cloned in pRDA_170 vector with the e2-crimson dark red fluorescence protein sequence. SgRNA sequences are provided in Table 5.1 in the appendix section. SNU5-Cas9 cells were transduced with viruses containing these vectors and then selected by puromycin treatment as described above. SNU5-Cas9 and SNU5 cells with sgRNA targeting gene of interest were mixed at a 1:1 ratio and seeded in 12-well plates ($2x10^5$ cells/well). Cells were treated by following the treatment schedule used in CRISPR screening, and on day3, the enrichment/depletion of e2-crimson-positive cells was assessed using BD FACS Celesta flow cytometry (Figure 2.8). Data analysis was performed by FlowJo software.

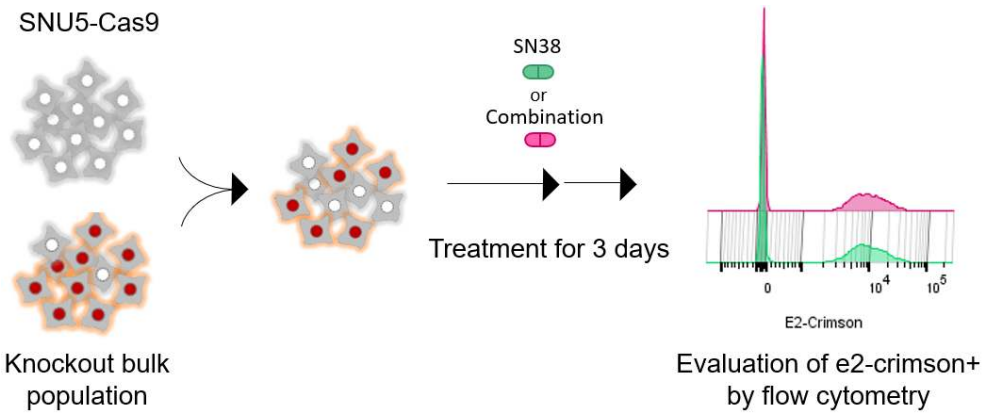

Figure 2.8: Experimental workflow of the competition assay.

2.7 RNAi-based Signature Assay

Eight shRNAs (Table 5.2 in the appendix section) used in RNAi-based GFP competition assay were in pMSCV-LTR-miR30-SV40-GFP (MLS) retroviral vector and validated for their knock-down and off-target effects[159–161]. Eμ-Myc Cdkn2a$^{Arf-/-}$ leukemia cells grown in BCM media were transduced with each GFP-tagged shRNA construct at 25-30% infection rate as described previously[162]. Cells were seeded into 24-well plates (125000 cells/well for treatment wells, 65000 cells/well for control wells) in 250μl BCM and treated with 250 μl of drug-containing media that reached the final concentration inducing 80-90% cell death (LD_{80-90}) at the end of 48 hours. After 24h, fresh media replaced 300 μl media of control wells and then 500 μl fresh media was added into all wells. At the end of 48 hours, the GFP percentage of treatment and control wells was determined using BD FACS Celesta flow cytometry by examining live cells based on DAPI exclusion. The experiment was performed as three independent biological replicates with three technical replicates. Resistance index (RI) was calculated by following formulation: $(GFP_{treatment} - (GFP_{treatment} * GFP_{control}))/ (GFP_{control} - (GFP_{treatment} * GFP_{control}))$ [159], which was used to generate the signature of each drug of interest. The experiment steps are summarized in Figure 2.9.

Each signature was compared with a previously generated reference set of drugs using the modified Euclidean K–nearest neighbors (K-NN) algorithm via MATLAB[149,159]. This algorithm calculates the linkage ratio (LR) between the drug of interest and the nearest category in the reference set by dividing the pairwise

distance of the category with the new drug by the category without the new drug. It determines the *p*-value by comparing the linkage ratio of the new drug to the distribution of negative-control linkage ratios. LR>1 and/or *p* value>0.05 is interpreted as the drug of interest that belongs to the "new class" with a mechanism of action not represented in the reference set[153]. Principle component analysis (PCA) was also performed as another means of data visualization using "pca" function in MATLAB, which was not used to classify the drugs.

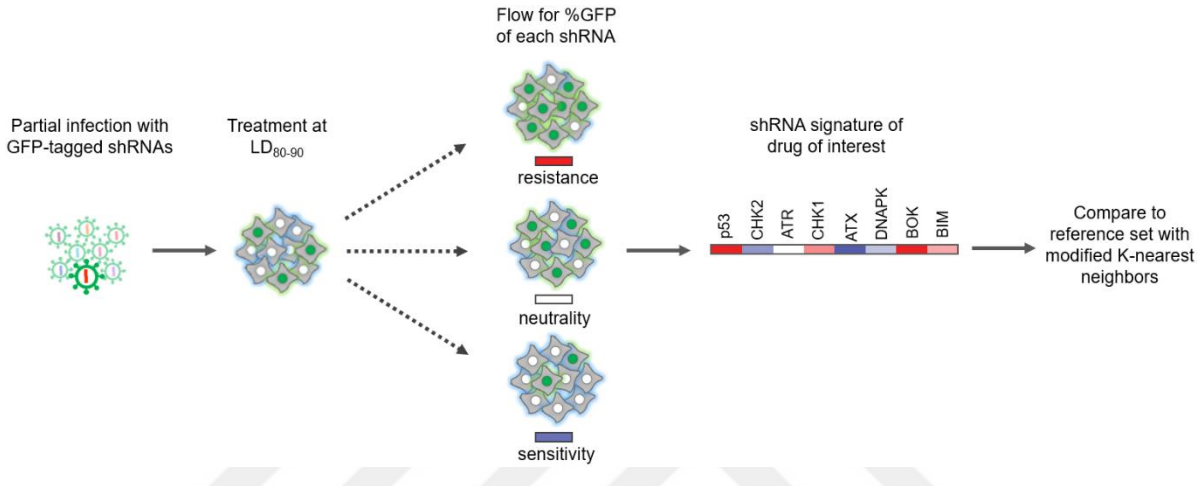

Figure 2.9: Illustration of RNAi-based signature assay. Eμ-Myc Cdkn2a$^{Arf-/-}$ lymphoma cells are infected with GFP-tagged shRNAs targeting eight specific genes. Each pool of cells containing the respective shRNAs was treated with an agent to induce 80-90% cell death. The percent GFP is determined at 48h using flow cytometry, which is used to generate an shRNA signature. This signature is then compared to the reference set using a modified K-nearest neighbors algorithm. The figure is adapted from[153].

2.8 qRT-PCR

The relative ABCG2 expression in gastric cancer cell lines was determined using qRT-PCR. RNA was extracted from 1-1.5x10^6 cells using RNA extraction kit following the manufacturer's instruction (Bio-Rad, USA). The concentration of RNA samples was measured using nanodrop.

For cDNA synthesis, the required amount of RNA was combined with 2.5μl of 2nM dNTPs (Life Technologies, USA) and 1μl of random hexamers (Invitrogen, USA) per sample. The total reaction volume was adjusted to 16.5μl

with nuclease-free H_2O. After incubation at 65°C for 5 mins, an RT mix consisting 5µl first-strand buffer (Invitrogen, USA), 2µl of 0.1M DTT (Invitrogen, USA), and 0.5µl of Rnasin (Promega, USA) was added to each tube and incubated at room temperature for 10mins. Finally, 1µl of MMLV-RT enzyme (Invitrogen, USA) was added. The reactions were incubated at 37°C for 1h and then inactivated at 70°C for 15 mins. Each reaction was diluted at a 1:10 ratio with nuclease-free H_2O for qRT-PCR experiments.

For the qRT-PCR reaction, 10µl of 2X Fast SYBR Green Master Mix (Applied Biosystems, USA), 1µl of 4µM primer mix, and 7µl nuclease-free grade H_2O were mixed with 2µl of diluted cDNA sample in each well of a 96-well optical plate (Applied Biosystems, USA). The C_T values for each reaction were determined using StepOnePlus Real-Time PCR System (Applied Biosystems). The GAPDH housekeeping gene was used to calculate the relative expression level of ABCG2. Primer sequences of ABCG2 and GAPDH primers, and melting curve analysis are provided in Figure 2.10.

Primer	Sequence (5' > 3')
ABCG2_F	AGCCACAGAGATCATAGAGCC
ABCG2_R	TTCTCACCCCCGGAAAGTTG
GAPDH_F	AGCCACATCGCTCAGACAC
GAPDH_R	GCCCAATACGACCAAATCC

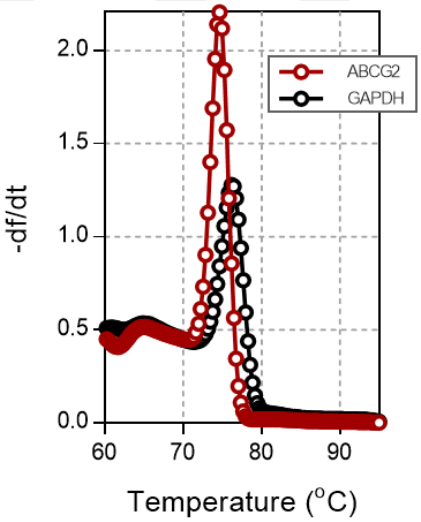

Figure 2.10: ABCG2 and GAPDH primers used in qRT-PCR. Sequences of ABCG2 and GAPDH primers are given on the left. The graph shows the melting curve analysis of qRT-PCR reactions that amplified the target regions using these primers. Both primers resulted in a single peak, the indicator of a single product generated by qRT-PCR reaction. -df/dt is a negative derivative of the fluorescence signal. F: forward. R: reverse.

2.9 Assessment of Efflux Pump Activity

$20x10^3$ of SNU5 cells were seeded in each well of 12-well plates and treated with erlotinib, osimertinib, and KO143, an ABCG2 inhibitor, at various concentrations including 10, 1, 0.1, and 0.01μM. Following day, cells were exposed to Hoechst-33342 dye, a specific substrate of ABCG2, at a final concentration of 5μg/mL for 45mins at 37°C in the dark. Cells were then washed with cold Hanks balanced saline solution (Gibco, USA) including 1mM HEPES (Gibco, USA) and 2% FBS (HBSS+) and taken into fresh media. Hoechst-33342 negativity was evaluated at three time points (T0, 1h, 16h) using FACSymphony A3 flow cytometer (BD Biosciences, USA) by recording at least 10000 events per sample. Results were analyzed using FlowJo software.

3. RESULTS

3.1 Investigation of Pharmacological Interactions Between Drug Pairs

We applied all drug pairs simultaneously to four different gastric adenocarcinoma cell models at constant ratio to identify the pharmacological interactions between drug pairs. The drug response to each treatment was evaluated using MTT assay. Sigmoidal dose-response curve optimized for each agent was presented in Figure 5.1. We used Compusyn program to calculate Combination index (CI) values at fraction-affected (fa) values ranging from 0.05 to 0.97 (Figure 3.1). A high variance in drug response to some of small molecule inhibitors was observed, which might be caused by heterogeneity in cell populations and dynamic regulation of expression or activity of molecular targets.

We selected the combination of SN38 and erlotinib for further investigation due to its consistent and robust synergy across all gastric cancer cell lines tested. Notably, this combination demonstrated the most potent synergistic effect in SNU5 cells, which are known to be highly chemoresistant, as supported by our comprehensive drug response analyses.

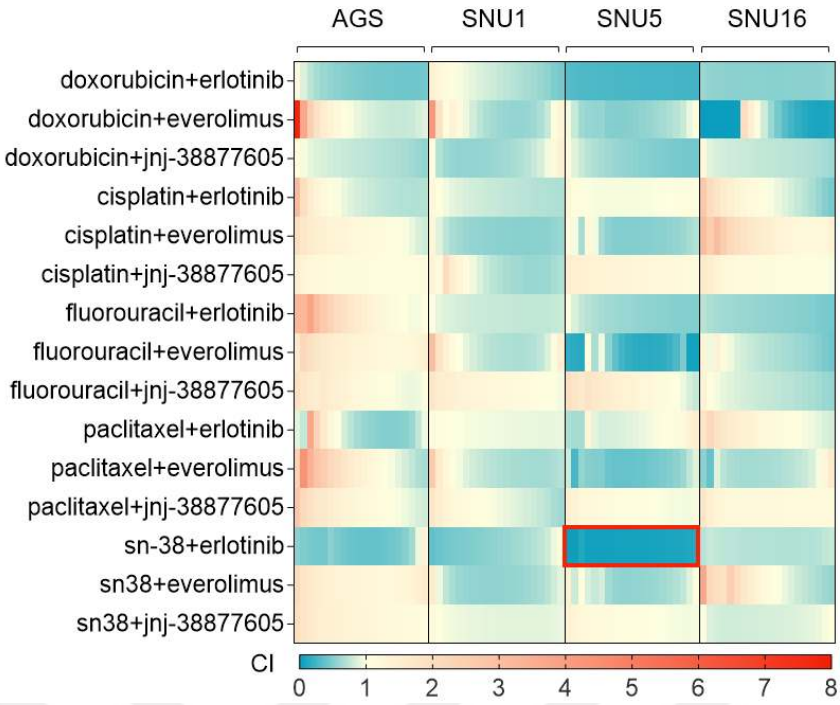

Figure 3.1: Concomitant application of drug pairs. Heat map shows CI values at fa values ranging 0.05-0.97 for each cotreatment in each cell line. Blue indicates synergism, and white and red indicate additivity and antagonism, respectively. The combination of SN38 and erlotinib in SNU5 cells is highlighted by a red box.

3.2 Evaluation of Drug Response to the Combination of SN38 and Erlotinib

Our drug screening, conducted using MTT analyses, demonstrated that the combination of SN38 and erlotinib exhibited the strongest synergistic effect when applied simultaneously across all gastric cancer cell models. This synergistic effect was particularly prominent in SNU5 cells (Figure 3.2). SNU5 cells were derived from the metastatic site of the patient after taking chemotherapy with 5-FU, doxorubicin, and mitomycin-C[165]. These cells harbor p53 mutation, MET amplification, and integrin-α hypermethylation[165]. Based on the analysis of drug response to single-agent treatments, we observed that SNU5 cells are the most chemotherapy-resistant cells to doxorubicin, 5-FU, paclitaxel, and SN38 compared to other cell lines.

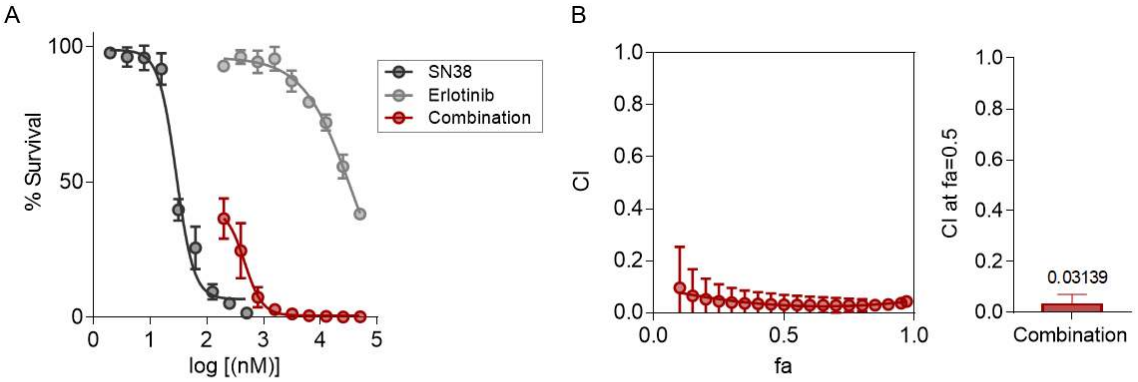

Concentrations									
SN38 (nM)	1.95	3.91	7.81	15.6	31.3	62.5	125	250	500
Erlotinib (μM)	0.19	0.39	0.78	1.56	3.13	6.25	12.5	25	50

Figure 3.2: The simultaneous application of SN38 and erlotinib in SNU5 cells. A. Dose-response curves of single and combination treatments. The concentrations of single agents applied at the constant ratio are given in the table below. B. CI-fa plot and CI value at fa:0.5 of the combination. CI: Combination index. Fa: Fraction-affected.

SN38 is an active metabolite of irinotecan, which acts as a topoisomerase I (TOPI) poison[166]. TOPI relieves both DNA negative and positive supercoiling by generating single-strand breaks during replication and then re-ligating the breaks[166]. SN38 binds both TOPI and DNA, traps the cleavage complexes generated by TOPI by blocking the re-ligation, which then leads to the replication collision and the activation of cell death pathways[166]. This mechanism explains the main cytotoxic activity of SN38 on highly replicative cancer cells[166].

We explored pharmacological interactions in the combination of erlotinib with another topoisomerase I poison, topotecan, and topoisomerase II poisons, including doxorubicin and epirubicin, by utilizing MTT assay. Simultaneous application of erlotinib with these agents achieved synergy (Figure 3.3). CF (cisplatin, 5-fluorouracil) and ECF (epirubicin, cisplatin, and 5-fluorouracil) combinations have been approved as standard treatment strategies for gastric cancer treatment. Our analysis showed that drug response to these combinations *in vitro* demonstrated that dual combination of erlotinib with topoisomerase I or II poisons achieved significantly enhanced synergistic effect compared to CF and

ECF combinations (Figure 3.3B). Interestingly, these combinations exhibited antagonistic effect in vitro.

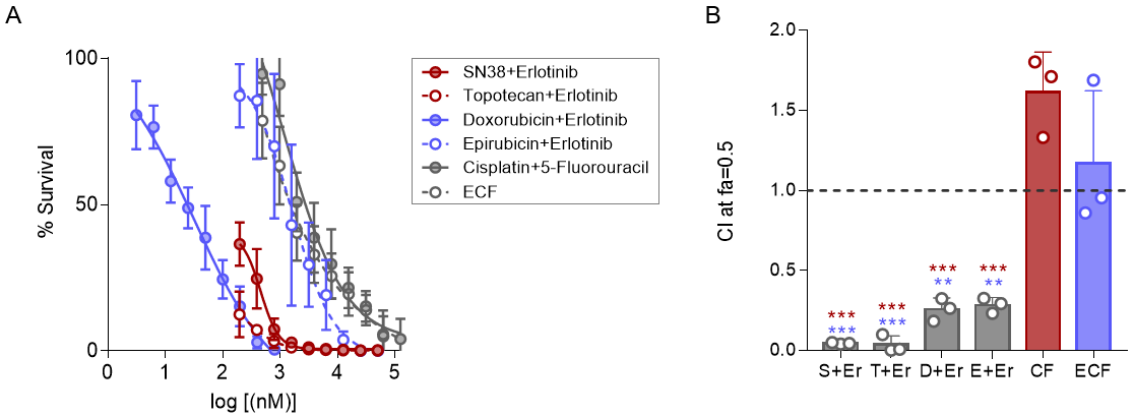

Figure 3.3: Comparison of combinations including erlotinib with CF and ECF. A. Dose-response curves of indicated combinations. B. CI value at fa:0.5 of each combination. Dunnett's multiple comparison test was used for statistical analysis. *** p<0.001, ** p=0.001. Er: erlotinib, S: SN38, T: topotecan, D: doxorubicin, E: epirubicin, C: cisplatin, F: 5-fluorouracil. CI: Combination index. Fa: Fraction-affected.

In MTT assay, drug response is evaluated based on the ratio of the relative number of live cells in treatment condition to the relative number of cells in vehicle control. This score is known as "relative viability". Relative viability (RV) is the most widely used metric to infer the drug sensitivity, which can be determined by the population-based assays like MTT[163]. Changes in RV can stem from the partial or complete inhibition of cell proliferation, increased cell death or both of these cellular processes[164]. Since RV measurement is completely based on the difference in population size of treatment group compared to control group, it does not provide any insight into the degree of cell death or arrest in cell proliferation at a given drug concentration[163].

Another metric that can be used to evaluate the drug response is the ratio of the number of live cells to the sum of live and dead cell numbers in treatment group itself, which is referred as to "fractional viability" (or its inverse, "lethal fraction" (LF))[163]. Since the fractional viability (FV) requires the measurement of the

number of dead cells in addition to live cells, it can provide direct insight into the degree of drug-induced cell death[156]. FV calculation does not require the calculation of the number of live or dead cells in different population like vehicle control, which reduces the problems related to plating bias[163].

Conventional pharmacometrics $IC_{50,}$ EC_{max} and AUC are quantified based on RV to infer drug sensitivity and resistance[164]. However, it has been realized that traditional metrics such as IC_{50} might substantially differ from one study to another[164]. One component of RV, therefore, IC_{50} calculation is the measurement of the (relative) number live cells in control group at the end of the assay duration[164]. This number can change due to the natural differences in cell proliferation rate, assay length and variations in growth conditions[163]. Therefore, all together can cause a drastic change in IC_{50} values between studies[164]. To overcome this problem, Hafner et. al. developed a new metric called the normalized growth rate inhibition (GR), which can be used as another parameter to understand drug response. GR compares the growth rate in the presence and absence of the drug[164]. $0<GR<1$ and $-1<GR<0$ are interpreted as growth arrest and cell death, respectively.

The multi-well plate-based FLICK assay developed by Richard *et al.* enables to calculate FV, GR and LF along with RV by quantifying cell death kinetics while retaining high-throughput assay format[156]. Based on the advantages of these pharmacometrics over RV, as mentioned above, we decided to evaluate the simultaneous application of SN38 and erlotinib in SNU5 cells using FLICK assay to investigate the synergy is dependent on growth arrest or cell death.

According to FLICK assay results, we observed that combination induced increased degree of cell death and caused significant decrease in population size compared to single-agent treatments, inferred by the quantification of FV and RV values, respectively (Figure 3.4). GR calculation showed that while lower doses of SN38 only treatment resulted in the drug-induced proliferative arrest, higher doses

led to cell death that was further enhanced by the combination. Additionally, erlotinib only treatment caused partial growth inhibition without cell death.

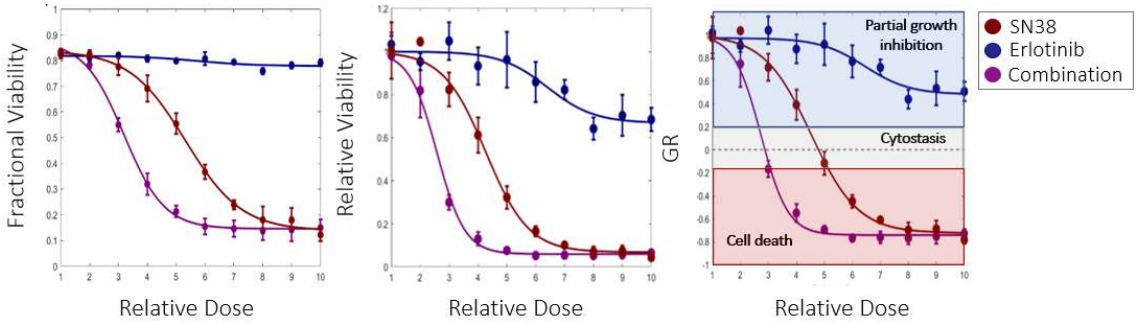

Relative Dose	1	2	3	4	5	6	7	8	9	10
SN38 (nM)	0	1.95	3.91	7.81	15.6	31.3	62.5	125	250	500
Erlotinib (μM)	0	0.19	0.39	0.78	1.56	3.13	6.25	12.5	25	50

Figure 3.4: Evaluation of SN38 and erlotinib combination via FLICK. FV, RV, and GR metrics were analyzed to assess drug response to the combination of SN38 and erlotinib. Concentrations of SN38 and erlotinib at corresponding relative doses are shown on the right. S: SN38. Er: Erlotinib. Com: Combination.

We measured cell death kinetics over time, which revealed the combination resulted in earlier death onset time and increased cell death rate compared to single treatments (Figure 3.5). Therefore, the findings obtained from the FLICK assay presented robust evidence of the synergistic effect induced by the combination of SN38 and erlotinib. Importantly, this assay revealed that this synergy was specifically reliant on cell death.

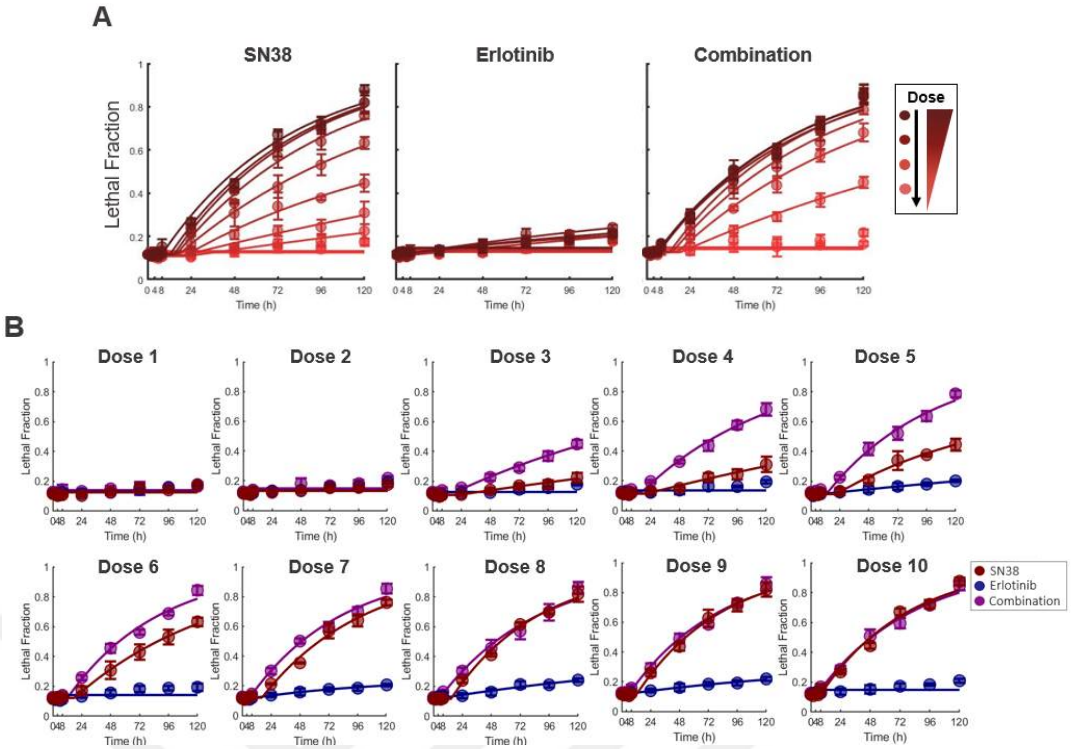

Figure 3.5: Cell death kinetics of combination and single agent treatments. A. Change in lethal fraction by concentration for each treatment over time. B. Comparison of combination with single-agent treatments at each concentration.

In addition to the combination of SN38 and erlotinib, we tested three of the top antagonistic drug pairs using the sequential application schedules via MTT assay to understand whether these schedules can transform antagonism into synergism (Figure 5.2). These drug pairs were the dual combination of everolimus with 5-FU, paclitaxel and SN38 in AGS cells. The most promising drug pair was the combination of everolimus and 5-FU which achieved synergism when 5-FU was applied 48 hours before everolimus (F48Ev) treatment according to MTT results (Figure 5.3). However, the results from the FLICK for F48Ev did not align with the findings obtained from the MTT assay (Figure 5.4).

MTT and FLICK assays analyze the two different aspects of drug response, which are metabolic activity and cell death. According to the results of both assays, we found that the combination of SN38 and erlotinib consistently achieved synergy by inducing cell death in SNU5 cells. Therefore, we decided to focus on

deciphering the molecular mechanisms behind synergy in this combination and identifying new molecular targets for gastric cancer therapy.

3.3 Assessment of Phenotypical Response to the Combination of SN38 and Erlotinib

We investigated phenotypical response to the combination compared to SN38 single treatment by analyzing cell cycle progression, DNA damage, and cell death. We conducted all these analyses under the same experiment conditions by applying SN38 and combination to SNU5 cells at low and high concentrations, given in Table 3.1.

$SN38^{low}$	3.7nM
$SN38^{high}$	13.5nM
$Combination^{low}$	3.7nM SN38 + 370nM Erlotinib
$Combination^{high}$	15.6nM SN38 + 1560nM Erlotinib

Table 3.1: SN38 and combination concentrations applied in phenotypical response experiments.

We first assessed the alterations in cell cycle progression between SN38 alone and combination at relatively low and high concentrations at different time points (0.5, 1, 4, 6, 8, and 12 hours – data is not shown). However, unequal propidium iodide (PI) staining between samples caused bias in the results of this experiment, but this experiment provided insight into the critical time points. Therefore, the same experiment was repeated at three 4h, 12h and 24h time points at low and high concentrations of SN38 only and combination treatments. We observed that while SN38 alone at low concentration did not cause any change in cell cycle profile over time, its high dose led to the arrest in cell cycle progression at S phase. Combination at high concentration resulted in the strong cell cycle arrest at the G1 phase; however, the equimolar concentration of SN38, SN38 at high dose and combination at low dose induced cell cycle arrest at the S phase. At these concentrations, it is unclear whether the presence of erlotinib only further enhanced the cellular response to SN38 or their combination resulted in the growth

arrest/cell death by activating entirely different intracellular signaling pathways (Figure 3.6, representative flow cytometry plots are presented in Figure 5.5).

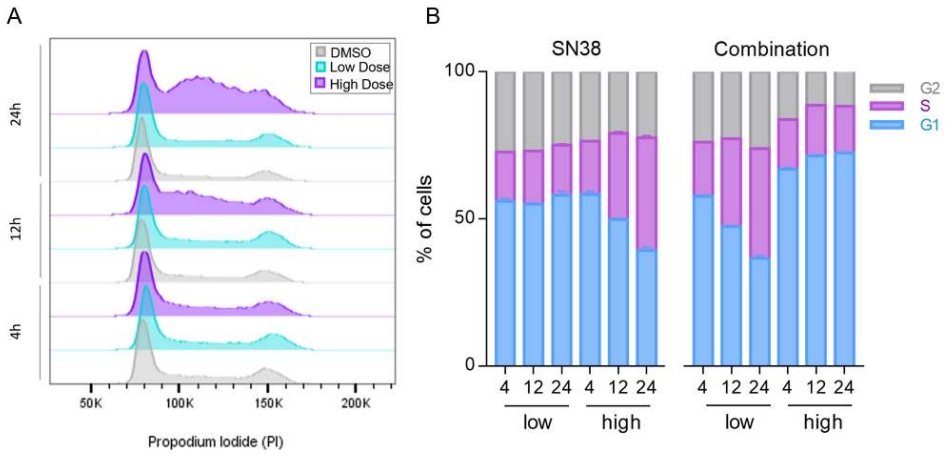

Figure 3.6: Assessment of cell cycle profile. A. Cell cycle analysis was performed via PI staining upon SN38 alone and combination treatments at low and high concentrations. Representative histogram plots of cell cycle phases of cells treated with SN38 only. B. Quantification of the results of the experiment. PI: propidium iodide. S: SN38. Er: Erlotinib.

Since SN38 is a DNA-damaging agent that inhibits topoisomerase-I, we investigated the level of DNA damage under the same treatment conditions mentioned above. We examined the level of phospho-H2AX, surrogate marker of DNA damage[167], along with cell cycle analysis since the change in DNA amount during proliferation might be misleading to infer DNA damage level (Figure 3.7, representative flow cytometry plots are presented in Figure 5.6). We observed that SN38 at the high dose and combination at the low dose elicited a similar DNA damage profile at each phase of the cell cycle and caused an increased level of DNA damage at the S phase at 24h. Combination at high doses led to the accumulation of DNA damage at G1 much higher than in other experiment groups, even at 4 hours. Results in Figure 3.7 show the analysis of DNA damage level normalized to DNA content.

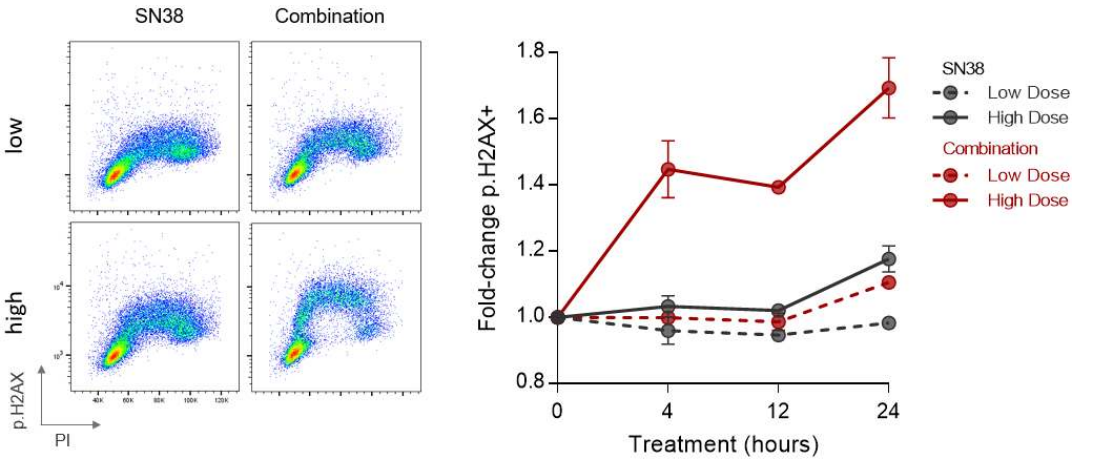

Figure 3.7: Analysis of DNA damage level. By coupling with cell cycle profiling, the degree of DNA damage was assessed by phospho-H2AX and PI stainings under SN38 alone and combination treatments at low and high concentrations. Representative flow cytometry plots (4h, left) and quantification of experiment results (right). PI: propidium iodide. p.H2AX: phospho-H2AX.

We applied small molecule inhibitors that target five different cell death pathways in the presence of SN38 only and combination to determine the type of cell death. Based on the quantification of LF kinetics over time, an intrinsic apoptosis inhibitor, Z-VAD-FMK, significantly delayed death onset time and decreased the cell death rate under both treatments (Figure 3.8). This data demonstrated that the cell death type induced by SN38 only and combination treatments was the intrinsic apoptosis pathway.

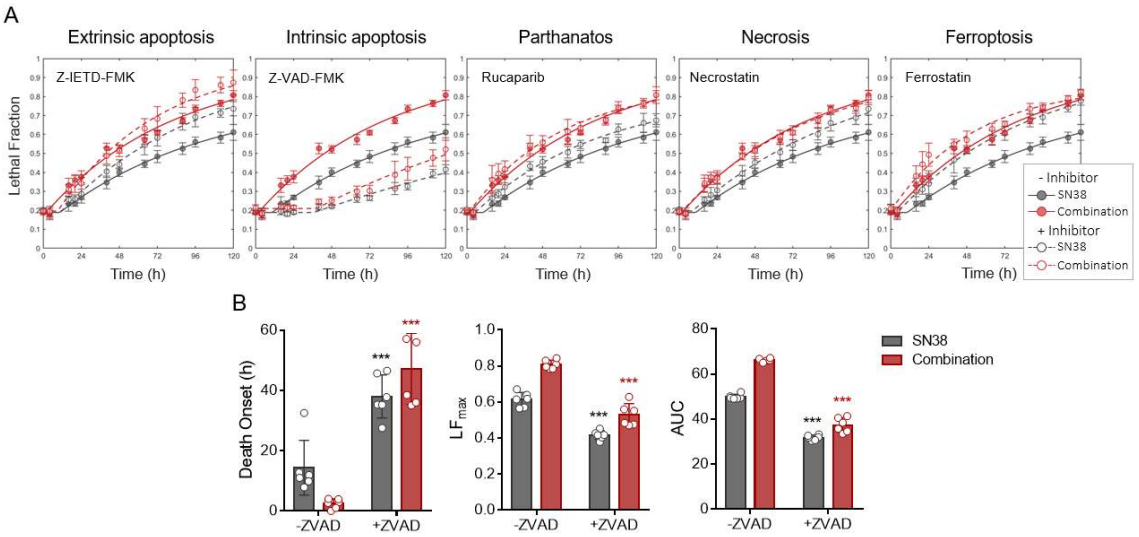

Figure 3.8: Determination of cell death type. A. LF kinetics over 120h under SN38 only (30nM) and combination (30nM SN38 + 3µM erlotinib) in the presence and absence of indicated inhibitors targeting extrinsic and intrinsic apoptosis, parthanatos, necrosis, and ferroptosis. Specific inhibitors that were used to target corresponding cell death pathway are provided at the top left. B. Quantification of the death onset time, maximum lethal fraction, and area under curve parameters of intrinsic apoptosis LF curves.

We then assessed apoptotic cell death under SN38 only and combination treatments at relatively high and low concentrations by analyzing the level of cleaved-caspase3 and cleaved-parp, of which full form is one of the key substrates of active caspase-3. Cleaved-caspase3 and cleaved-parp levels increased at 24 hours in response to SN38 at high and combination at low doses. Combination at the high dose strongly induces apoptosis even at 12 hours (Figure 3.9, representative flow cytometry plots are presented in Figure 5.7).

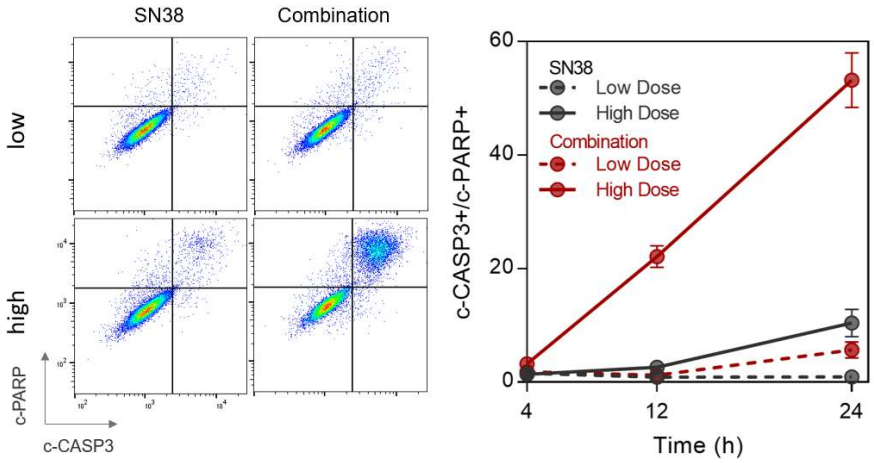

Figure 3.9: Evaluation of apoptotic cell death. The apoptotic response to SN38 only and combination treatments at relatively low and high concentrations was investigated via cleaved-caspase3 (c-CASP3) and cleaved-parp (c-PARP) co-staining. Representative flow cytometry plots (12h, left) and quantification of experiment results (right) are shown.

Based on analyses of phenotypical responses, we concluded that both SN38 and combination treatments triggered DNA damage-induced apoptotic cell death. However, whether these treatments activate cell death by employing the same intracellular signaling pathways remained elusive. Although SN38 was applied at the equimolar concentration in single and combination treatments at both low and high concentrations, incorporating erlotinib in combination led to a more efficacious response in SNU5 cells compared to SN38 alone. Therefore, we decided to investigate the relationship between EGFR inhibition by erlotinib and synergy in combination.

3.4 Analysis of Drug Response to the Combination of SN38 and EGFR Inhibitor in SNU5$^{EGFR\text{-}KO}$ Cells

We established SNU5$^{EGFR\text{-}KO}$ single-cell clones to investigate the dependency of synergy in combination on the inhibition of EGFR signaling by erlotinib. Evaluation of EGFR expression in single-cell clones via immunoblotting showed we obtained five different clones knockout for EGFR (Figure 3.10). EGFR

knockout in SNU5$^{EGFR\text{-}KO4}$ and SNU5$^{EGFR\text{-}KO20}$ clones was further confirmed using Sanger sequencing.

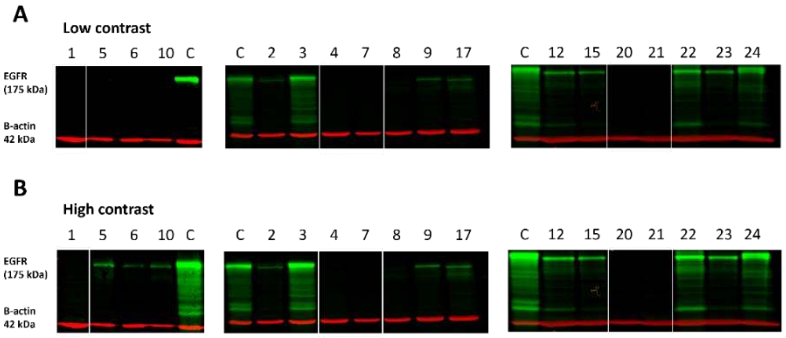

Figure 3.10: Profiling EGFR expression in single-cell clones. We established five different EGFR knockout cell lines, numbered 1,4,7,20, and 21. A. Low contrast membrane images. B. High contrast membrane images. C: Control (parental) cells.

We analyzed drug response in SNU5$^{EGFR\text{-}KO}$ single-cell clones using FLICK to understand at which level the response to the combination was dependent on the inhibition of EGFR activity, therefore, EGFR-induced signaling pathways. The combination resulted in increased cell death compared to SN38 alone, as observed in parental cells (Figure 3.11A and Figure 3.12A). Therefore, EGFR knockout could not substitute its pharmacological inhibition. This data indicated that the combination mechanism of action was not solely dependent on the inhibition of EGFR activity, which might be associated with the activity of erlotinib on molecular targets other than EGFR. It has been previously shown that erlotinib can also inhibit the activity of tyrosine receptor kinase B (TrkB) and ERK1/2 phosphorylation and the expression of signal transducer and activator of transcription 3 (STAT3)[168]. Therefore, the combination might mainly act through the inhibition of other targets of erlotinib along with the disruption of topoisomerase-I activity. RV and GR analysis of experiments in Figure 3.11 and 3.12 are presented in Figure 5.8 in the appendix section.

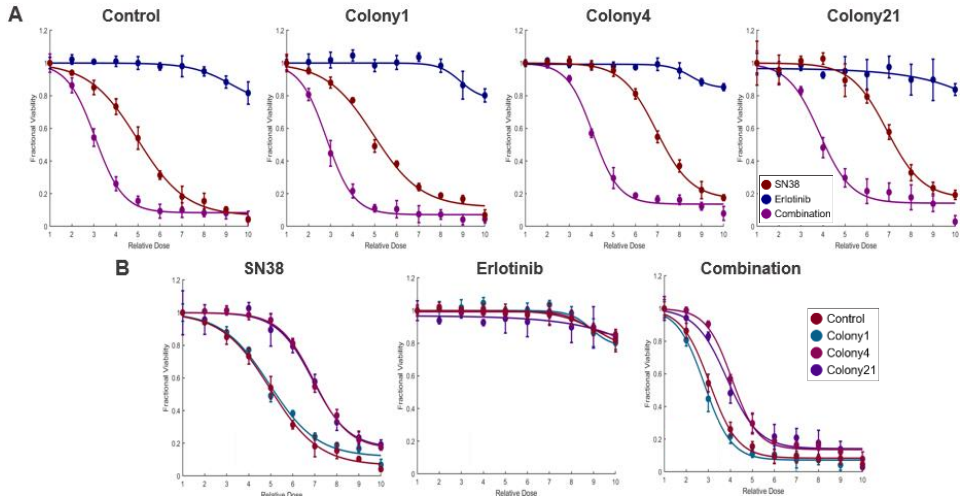

Figure 3.11: Investigation of drug response in SNU5$^{EGFR\text{-}KO}$ clones (first batch). A. Evaluation of drug response to combination and single-agent treatments for each cell line by determining fractional viability at corresponding doses (shown in Figure 3.4) B. Comparison of drug response between cell lines to each treatment. x-axis: fractional viability, y-axis: relative dose.

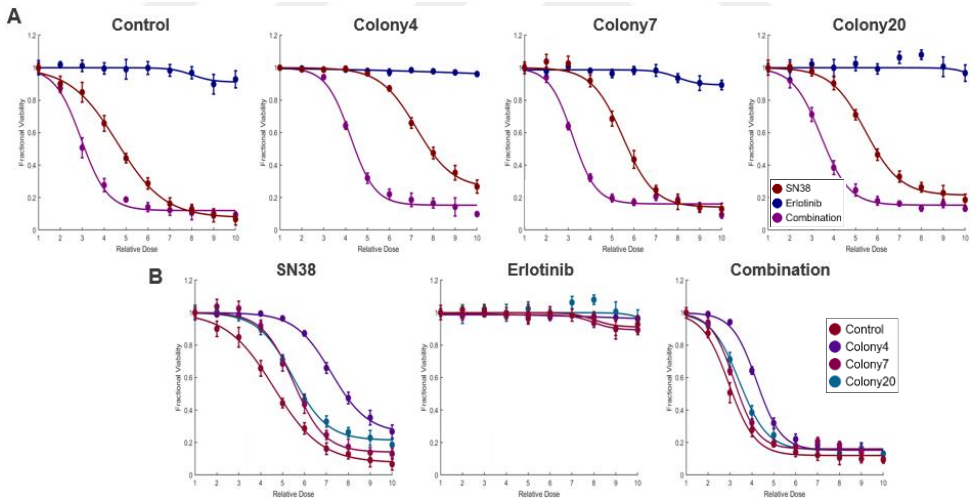

Figure 3.12: Investigation of drug response in SNU5$^{EGFR\text{-}KO}$ clones (second batch). Drug response in EGFR knockout SNU5$^{EGFR\text{-}KO4}$ was re-analyzed in this experiment. A. Evaluation of drug response to combination and single-agent treatments for each cell line by determining fractional viability at corresponding doses. B. Comparison of drug response between cell lines to each treatment. x-axis: fractional viability, y-axis: relative dose (shown in Figure 3.4).

Interestingly, some SNU5$^{EGFR\text{-}KO}$ clones, such as SNU5$^{EGFR\text{-}KO4}$ and SNU5$^{EGFR\text{-}KO21}$, developed resistance to SN38 alone and combination treatments compared to control cells (Figure 3.11B). Studies associated with radiotherapy have revealed that in addition to the canonical signaling pathways induced by EGFR, EGFR itself or its downstream signaling pathway(s) regulate DNA damage repair pathways[169]. EGFR and/or its effectors can play critical roles in the expression, activation, and intracellular localization of DNA damage repair proteins[169]. This finding might explain why some of our EGFR knockout cell lines became resistant to SN38 alone and combination treatments. Since these cells might develop the adaptation to the absence of EGFR signaling contrary to the pharmacological inhibition of EGFR by erlotinib, they might activate DNA damage repair through other intracellular signaling cascades independent of EGFR signaling.

We investigated whether SNU5$^{EGFR\text{-}KO4}$, one of the clones resistant to SN38 only and the combination, was also less sensitive to SN38 analogs, topotecan and camptothecin and a dual combination of both drugs with erlotinib (Figure 3.13). SNU5$^{EGFR\text{-}KO4}$ was also more resistant to topotecan, camptothecin, and their combination with erlotinib than SNU5 parental cells. This data further suggested that EGFR knockout might induce enhanced DNA damage response in these cells.

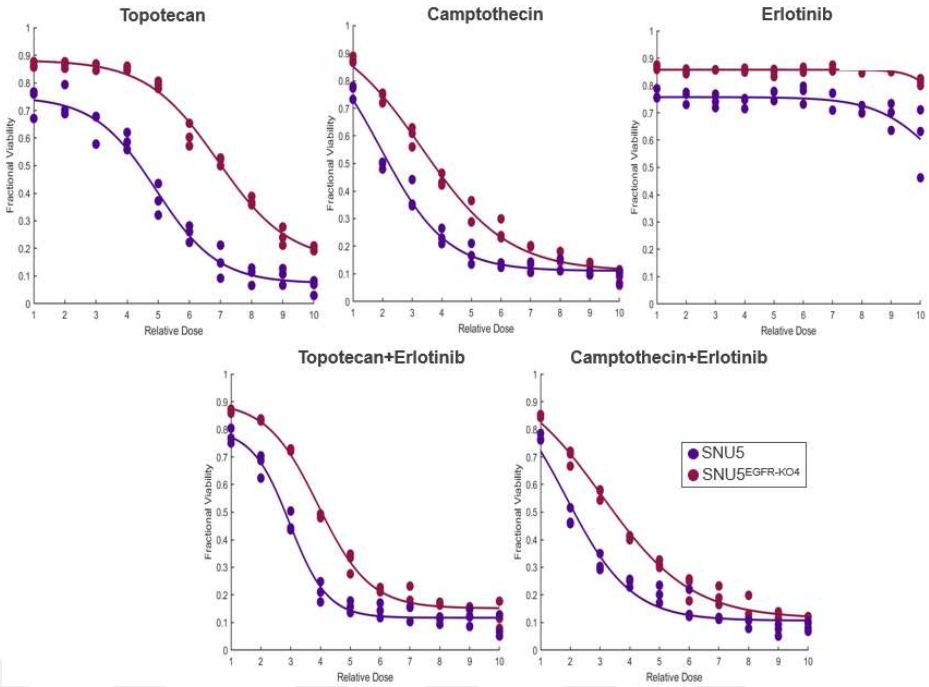

Figure 3.13: Analysis of drug response in SNU5$^{EGFR\text{-}KO4}$ and SNU5 cells to topotecan, camptothecin, and the combination of both with erlotinib. x-axis: fractional viability. y-axis: relative dose.

Drug response analyses in SNU5$^{EGFR\text{-}KO}$ single-cell clones indicated that synergy in combination was independent of EGFR inhibition by erlotinib. However, it remained unsolved how combination elicited a more efficacious response compared to SN38 alone. To answer this question, we performed a genome-wide perturbation screening coupled with annexin-V bead sorting to reveal erlotinib action in combination and the differences in the activation of cell death between SN38 alone and combination treatments.

3.5 A Genome-wide CRISPR Screening

3.5.1 Optimization Results

We decided to optimize the equipotent concentration of SN38 and the combination treatments to conduct CRISPR screening and investigate the distinctions in genetic dependencies of cell death or survival between these treatments. We tested three different doses of each treatment, which were acquired

from the FV analysis. For this purpose, the number of both live and dead cells was counted for five days (Figure 3.14).

A

	Data from FLICK	SN38 (nM)	Erlotinib (nM)	FV
Dose1	SN38-1	8.3	0	0.685
	Combination-1	2.7	270	0.685
Dose2	SN38-2	13.5	0	0.583
	Combination-2	3.7	370	0.583
Dose3	SN38-3	21.2	0	0.467
	Combination-3	5	500	0.467

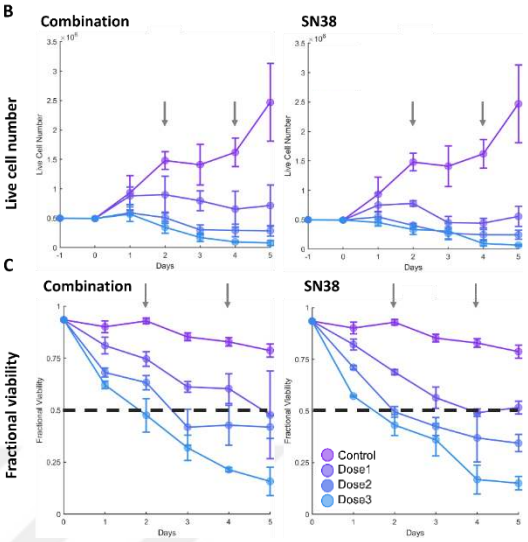

Figure 3.14: Results of the first live and dead cell counting experiment. A. Equipotent concentrations of SN38 and combination to which cells were exposed. Selected dose is indicated by red. B. Change in cell number, C. Change in FV at each day throughout 5-days treatment period. Dotted line shows FV:0.5 Arrows indicate the media change/re-treatment.

We optimized the equipotent concentration of both treatments inducing the fractional viability of around 0.5 to obtain %50 of live and dead fractions after annexin-V magnetic bead sorting at the end of the CRISPR screen. The trypan blue cell counting experiment results in 12-well plates shown in Figure 3.14 provided insight into the optimal drug exposure period and concentration, which were three days of drug exposure at *dose2* of both treatments, respectively. We then repeated the same experiment in 10 cm plates since the size of the cell population and dimensions of culture plate might affect the drug response, especially in suspension cells (Figure 3.15).

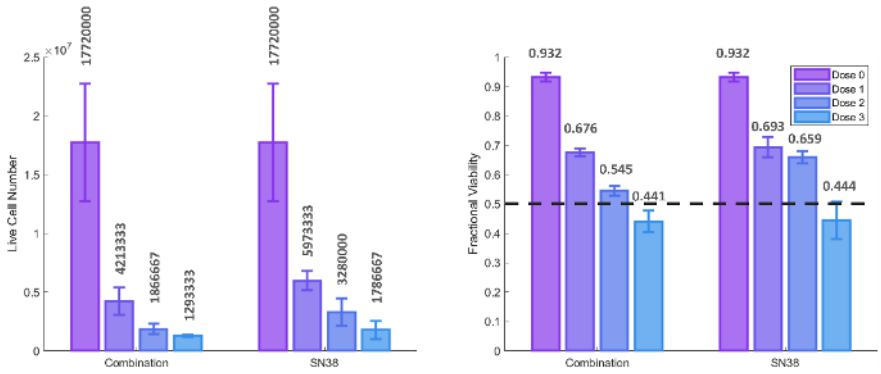

Figure 3.15: Results of the second live and dead cell counting experiment after exposing cells to equipotent doses of SN38 and combination for three days in 10 cm plates. The dotted line shows FV:0.5.

Since the longest drug exposure period in experiments assessing phenotypical response was 24h, we performed the same experiments for three days of drug exposure (Figure 3.16). We observed that cell cycle profile, DNA damage level, and apoptotic response were similar between treatment groups when SN38 and combination were applied at *dose2* concentrations.

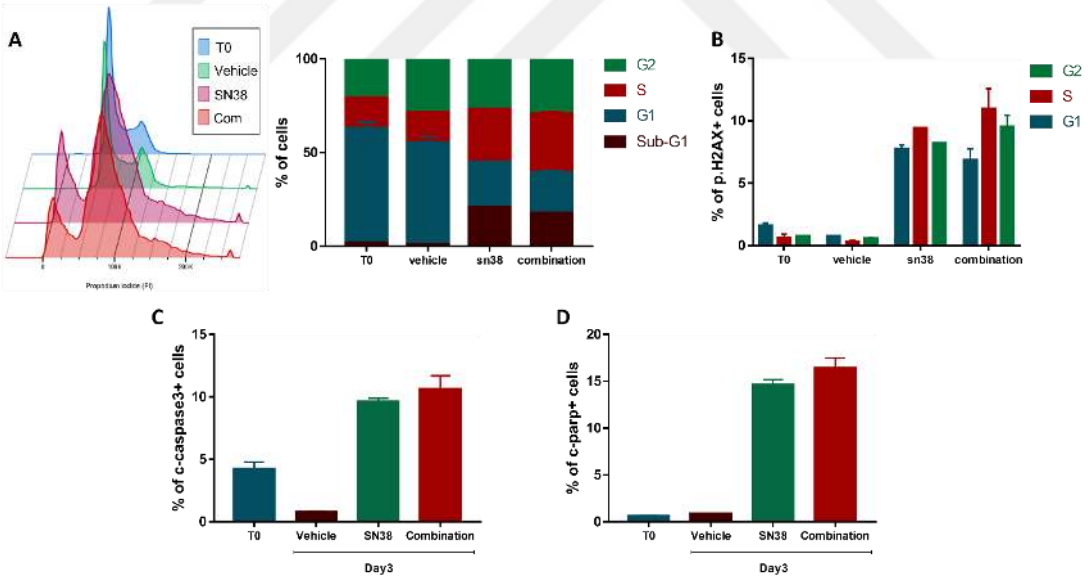

Figure 3.16: Phenotypical response to SN38 and combination applied at *dose2* for three days. A. Cell cycle distribution of the population. Representative histogram plot of flow cytometry analysis is shown at the left. B. The level of phospho-H2AX. C. Cleaved-caspase3 and D. Cleaved-parp analysis. c-caspase3: cleaved-caspase3. c-parp: cleaved-parp.

As shown in Figure 3.16A, nearly %20 of the cell population treated with either SN38 or the combination accumulated in the sub-G1 phase of the cell cycle. This result can be interpreted as another indicator of apoptosis since DNA is fractioned into small pieces by the activity of endonucleases and leaks out of cells at the late stages of apoptosis, resulting in decreased DNA content.

We conducted optimization experiments for the annexin-V magnetic bead sorting step to efficiently separate dead and live cell fractions at the end of CRISPR screening. For this purpose, annexin-V positivity of cell populations was initially evaluated by exposing cells to either SN38 or combination without bead sorting to understand whether it captured fractional viability (~0.5-0.6) results of cell counting experiments. *Dose2* of SN38 and combination treatments produced ~50% annexin-V positivity (Figure 3.17A). Since both treatments at *dose2* induced similar responses, we conducted upcoming experiments only for the combination. Next, we tested the efficiency of bead sorting and found that this technique can enrich both live and dead populations above 75% (Figure 3.17B). The number of cells recovered after the sorting is also a critical parameter for the CRISPR screen. Therefore, we established an experiment at a high cell number (~150x10^6 cells, of which ~75 x10^6 was live and ~75 x10^6 was dead based on cell counting with a hemacytometer.) to mimic the screen conditions. Then, we also calculated the number of cells after sorting in both live and dead fractions with a hemacytometer (Figure 3.17C). Nearly 30% of each population was lost during the sorting procedure. Based on this result, we sorted 180 million cells (90 million dead and 90 million live cells) for each treatment condition per replicate at the end of the screen.

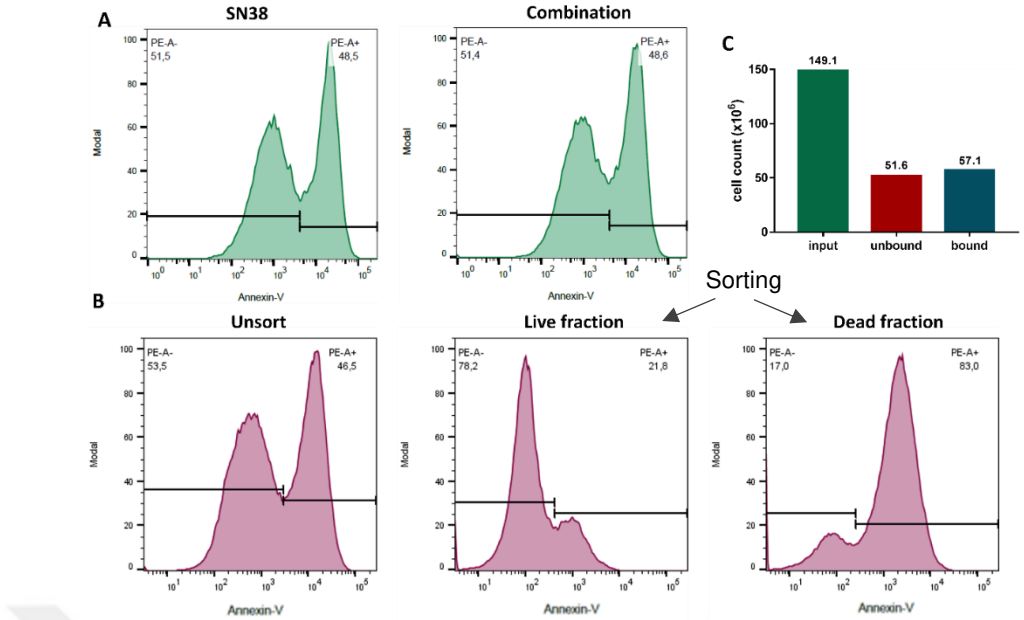

Figure 3.17: Optimization of annexin-V magnetic bead sorting experiment for CRISPR screen A. Annexin-V staining of cells treated either with SN38 alone or combination without bead sorting B. Annexin-V staining of cells treated with combination with or without bead sorting. C. The result of the cell count experiment before and after bead sorting. PE: Fluorophore conjugated to Annexin-V.

3.5.2 Experiment Procedure

We conducted genome-scale CRISPR screening in SNU5-Cas9 cells for SN38 alone and combination treatments, of which steps were mentioned in detail in the material-method section. Cells were infected with the TKOv3 library. As a control group to inspect Cas9 activity, a small number of Cas9-expressing cells were infected with EGFR sgRNA3 only, by which EGFR knockout cell lines were previously generated. At the end of the puromycin selection, we evaluated EGFR expression in these cells compared to un-transduced SNU5-Cas9 cells via immunoblotting. Cas9 activity was demonstrated by decreased EGFR expression in SNU5-Cas9 cells that were transduced with sgRNA targeting EGFR (Figure 3.18).

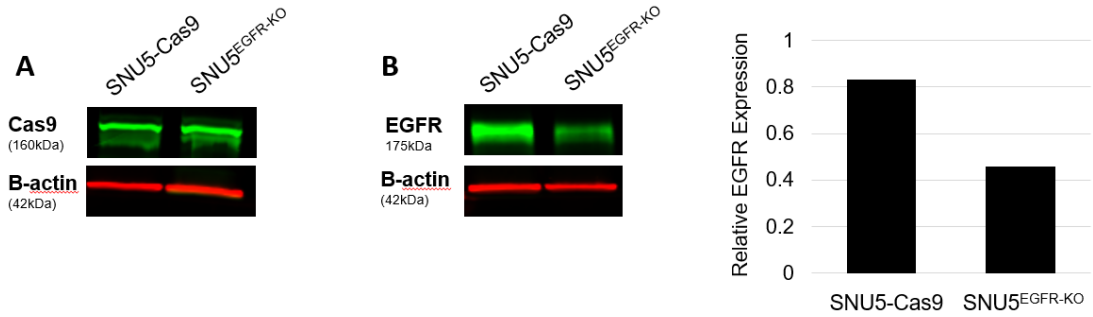

Figure 3.18: Evaluation of EGFR expression by immunoblotting. A. Image of an immunoblot showing Cas9 expression. B. Image of an immunoblot (left) showing the decrease in EGFR expression in the total population and the quantification of data (right). SNU5$^{EGFR-KO}$: Cells expressing both Cas9 and sgRNA targeting EGFR.

After expanding screen cultures to reach approximately 300-400 coverage and confirming Cas9 activity, we applied equipotent concentrations of SN38 and the combination. At the end of the treatment schedule, we conducted annexin-V bead sorting to dissect the mechanisms of cell death induced by SN38 and the combination by analyzing both dead and live cell fractions. Genomic DNA was isolated from both fractions, and the integrity of DNA was examined by running all experiment samples on agarose gel (Figure 3.19). Although all samples were loaded at equal mass, genomic DNA isolated from dead fraction samples yielded less intense bands with longer tails than other samples. We expected this result since these fractions were enriched for actively dying cells that fragment DNA into small pieces.

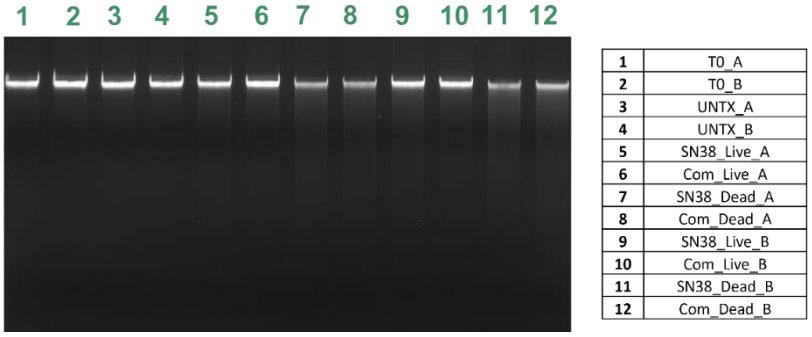

Figure 3.19: Agarose gel image showing genomic DNA of experiment samples. UNTX: Control. Com: Combination. A and B indicate the replicates.

We performed '*pseudo*-RT-PCR' to optimize the DNA input amount and cycle number for PCR1 since determining these parameters is critical to prevent the saturation of PCR reaction that can cause a biased library amplification. In this experiment, we amplified a broad range of DNA amounts with different cycle numbers from 17 to 25, and PCR products were run on the agarose gel (Figure 3.20). According to the results, we could amplify 1.5µg-3µg DNA with 23 PCR cycles without saturation. We also tested whether more DNA mass could be amplified with 23 cycles without the saturation of the reaction. For this purpose, we amplified DNA masses from 1.5µg-4µg with the same cycle numbers (Figure 3.20C, gel images are provided in Figure 5.9 in the appendix section). Only 1.5,2 and 2.5µg DNA masses followed the linear regression at the corresponding cycle number. Therefore, we decided to amplify the genomic DNA of all samples by adding 2.5µg DNA into each reaction with 23 cycles.

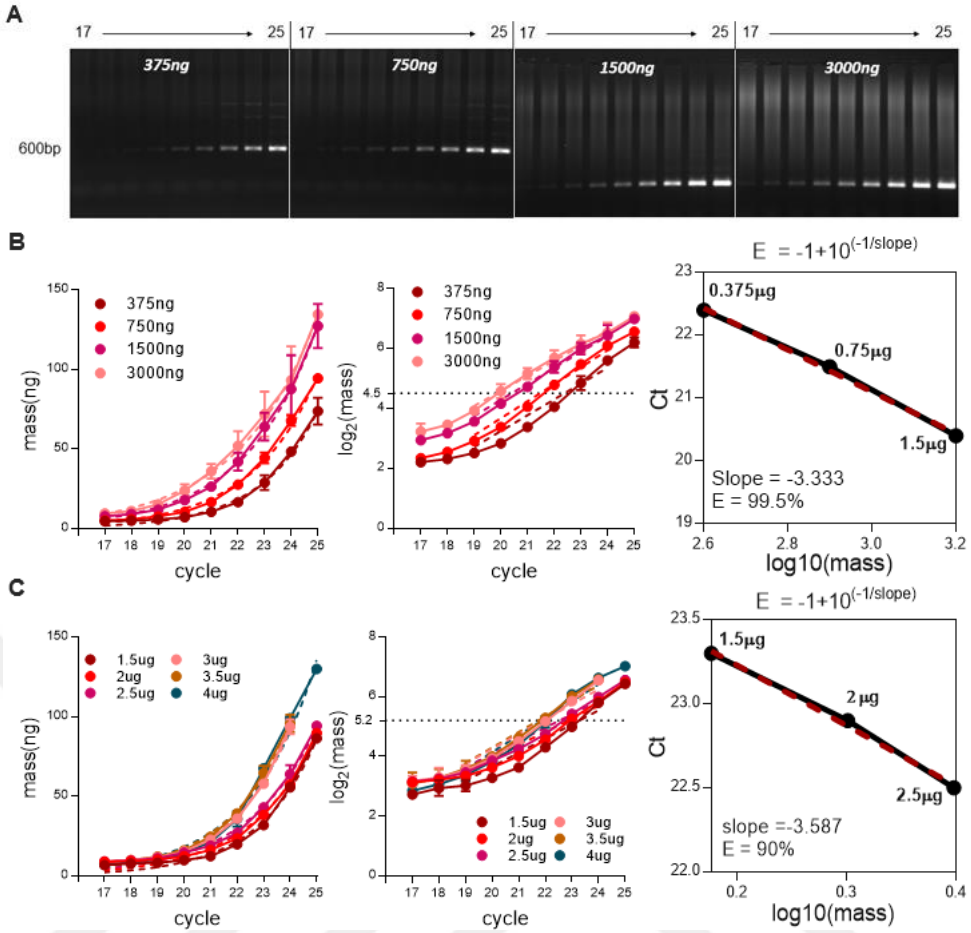

Figure 3.20: Optimization of PCR1 reaction. A. Agarose gel images of PCR1 products produced by amplifying different DNA masses with cycle numbers ranging from 17 to 25. B. Exponential increase in DNA mass by cycle (left). We evaluated the change in $\log_2$(DNA mass) by cycle number via linear regression (center). A $\log_2$(mass) at which point-to-point lines of all DNA masses followed the linear regression was selected to calculate the PCR efficiency, which was 4.5, indicated by a dotted line. Analysis of the correlation between cycle numbers corresponding to $\log_2$:4.5 and the starting DNA amount based on $\log_{10}$ (right). PCR efficiency was inferred by using the formulation shown at the top. C. The same process was followed for DNA masses ranging from 1.5µg to 4µg. Ct: Cycle threshold.

Representative agarose gel images of PCR1 and PCR2 reactions are presented in Figure 3.21. We excised 200bp PCR2 products of samples, and purified DNA from agarose gel, then sent to the next generation sequencing.

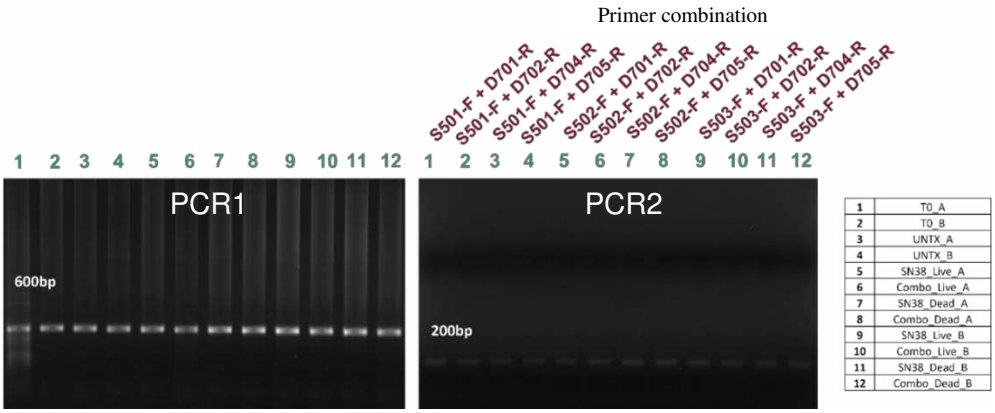

Figure 3.21: Representative agarose gel images of PCR1 and PCR2 reactions. Primer combinations used to amplify the 200bp product of interest with the sequencing adapters are shown at the top of the right gel image.

3.5.3 Analysis

In the first step, we examined the correlation between replicates of each experiment group at the $\log_2$ count level to analyze the variation between replicates. As shown in Figure 3.22, the biological replicates of experiment groups were well correlated.

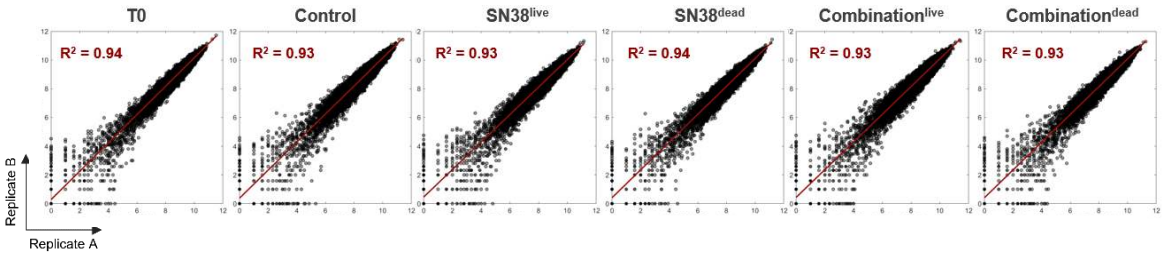

Figure 3.22: Log2 count level correlation between the biological replicates of each experiment group at the x-axis: replicate A at log2 count level. y-axis: replicate B at log2 count level.

We assessed the sgRNA distribution of randomly selected one hundred essential genes from Hart *et al.*[170] compared to the distribution of nontargeting sgRNAs in L2FC of *untreated vs T0* (Figure 3.23). This data demonstrated that sgRNAs of most of the essential genes were depleted in the untreated experiment group. The distribution of sgRNAs of a few essential genes, such as Papola and Rpa1, overlapped with the nontargeting sgRNAs' distribution. However, this result was expected since the degree of essentiality may differ between the cell types.

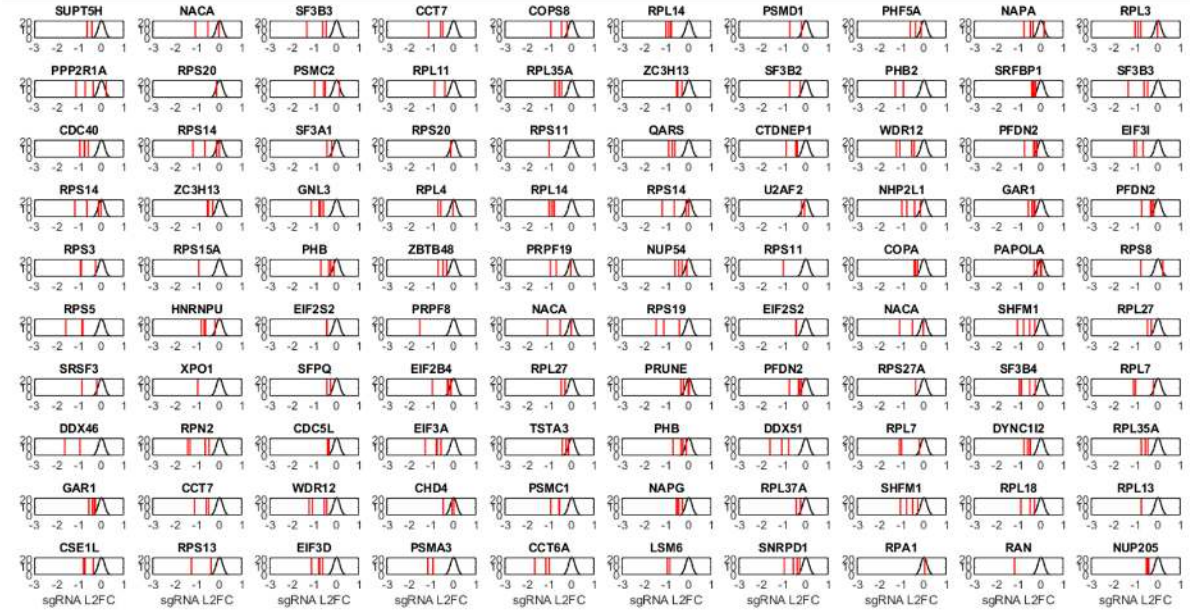

Figure 3.23: Single guide RNA distribution of randomly selected one hundred essential genes in *untreated vs T0*. Red lines indicate each sgRNA that targets the corresponding essential gene, and black curves represent the distribution of nontargeting sgRNAs.

We decided to test different analysis pipelines to collapse guide-level L2FC values into *z*-scored gene-level scores since the determination of the "best" analysis strategy tends to be dependent on the experiment conditions that can affect the distribution of targeting/nontargeting sgRNAs and the magnitude of the changes within the data. These analysis strategies included the calculations of the mean or median of all sgRNAs for a given gene with or without removing one sgRNA with L2FC closest to zero. We determined the quality of each analysis strategy by its ability to recover core essential genes in untreated cells compared

to *T0* input library assessed by ROC curves. These curves reported the recovery of core essential genes[170] (true positives) compared to nontargeting genes (false positives) at various FDR cut-offs (Figure 3.24A). We also assessed the distribution of core essential genes at *z*-scored L2FC in untreated *vs T0* comparison (Figure 3.24B). Since the ability of the *all_mean* method to recover the core essential genes in untreated cells compared to *T0* input library is statistically more powerful than other methods (Figure 3.24A), we decided to identify hit genes based on this strategy.

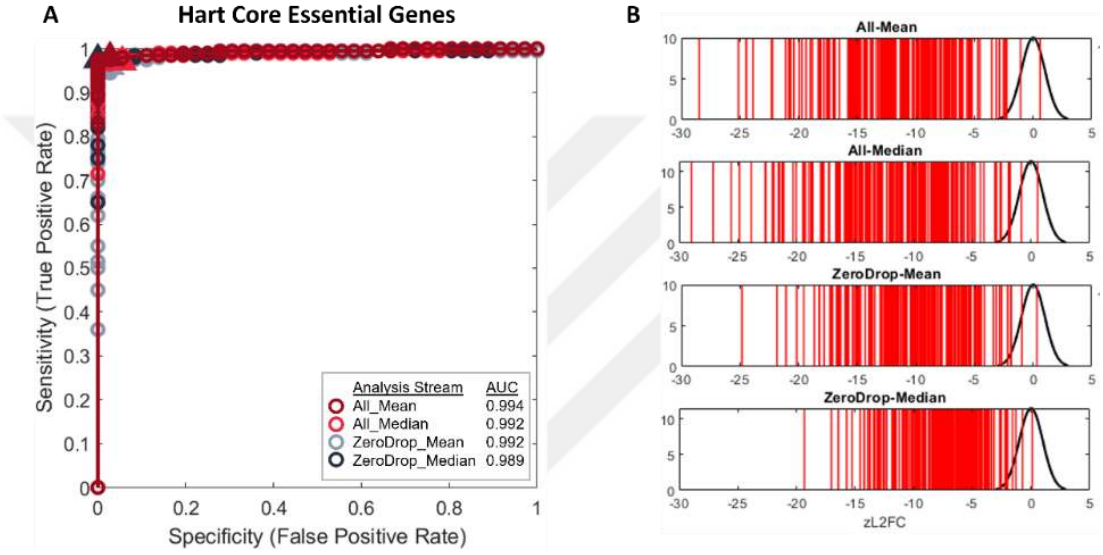

Figure 3.24: Comparison of different analysis pipelines. A. ROC curves for all analysis streams. AUC was calculated for each ROC curve. Based on this data, the strategy that calculated the mean of all sgRNAs for a given gene was selected for the downstream analyses (dark red curve). FDR = 0.05 cut-off of each curve is shown by a rectangular symbol. B. Distribution of essential genes (red) and nontargeting genes (black) in untreated cells compared to T0 input control using different analysis strategies.

To evaluate the quality of the *all_mean* strategy, we examined the depletion of core essential genes[170] at *z*-scored gene level L2FC computed by this strategy in untreated cells compared to *T0* along with all other genes and nontargeting controls (Figure 3.25A) for the quality inspection. We also compared the distribution of *z*-

scored gene level L2FC of core essential genes to the distribution of all genes (Figure 3.25B).

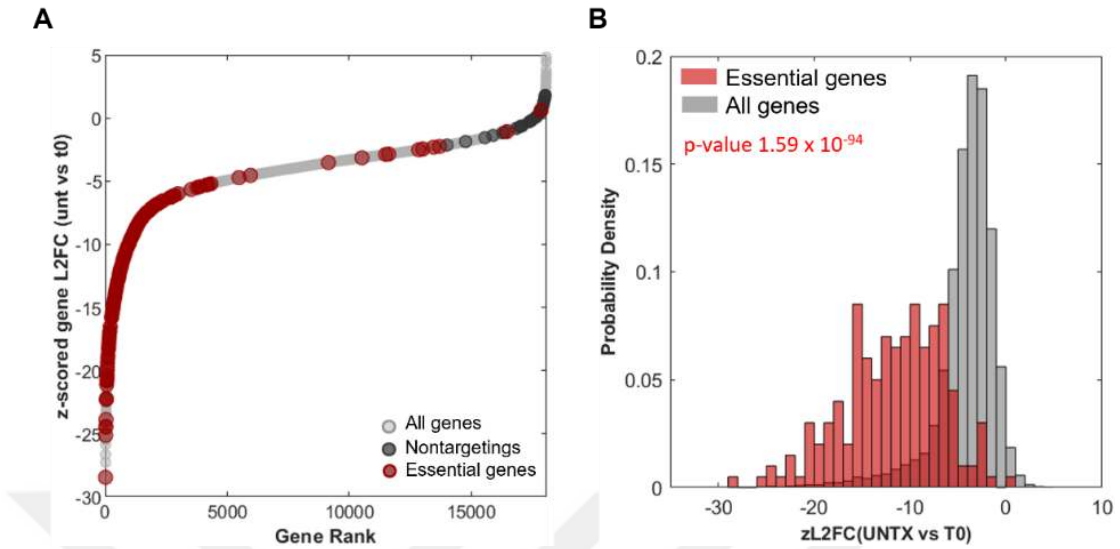

Figure 3.25: Evaluation of the quality of all_mean analysis stream. A. Depletion of core essential genes (red) from Hart *et al.*[170] at *z*-scored gene level L2FC calculated by *all_mean* analysis in untreated cells compared to T0. B. Histogram of z-scored gene level fold changes for all genes (grey) and core essential genes (pink). The *P*-value was calculated using the KS-test.

We determined the correlation between the replicates of untreated cells compared to *T0* input library at the L2FC of sgRNA level and *z*-scored gene level to examine the quality of CRISPR screen results (Figure 3.26). This analysis showed that the biological replicates of untreated cells *vs T0* comparison were positively correlated.

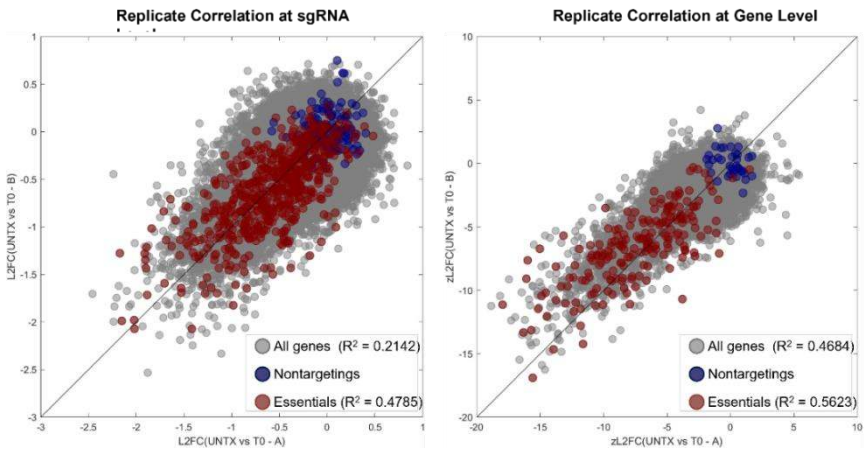

Figure 3.26: L2FC of sgRNA level and z-scored gene level correlations between the replicates of untreated cells compared to *T0* at the L2FC of sgRNA level (left) and *z*-scored gene level (right).

We computed *z*-scored gene level L2FC values of dead cells compared to live cells using the *all_mean* analysis strategy to enlighten the differences between the death mechanisms induced by SN38 only and combination treatment. GSEA of gene-level fold change scores of dead cells compared to live cells revealed the biological processes significantly upregulated in the dead populations (Figure 3.27).

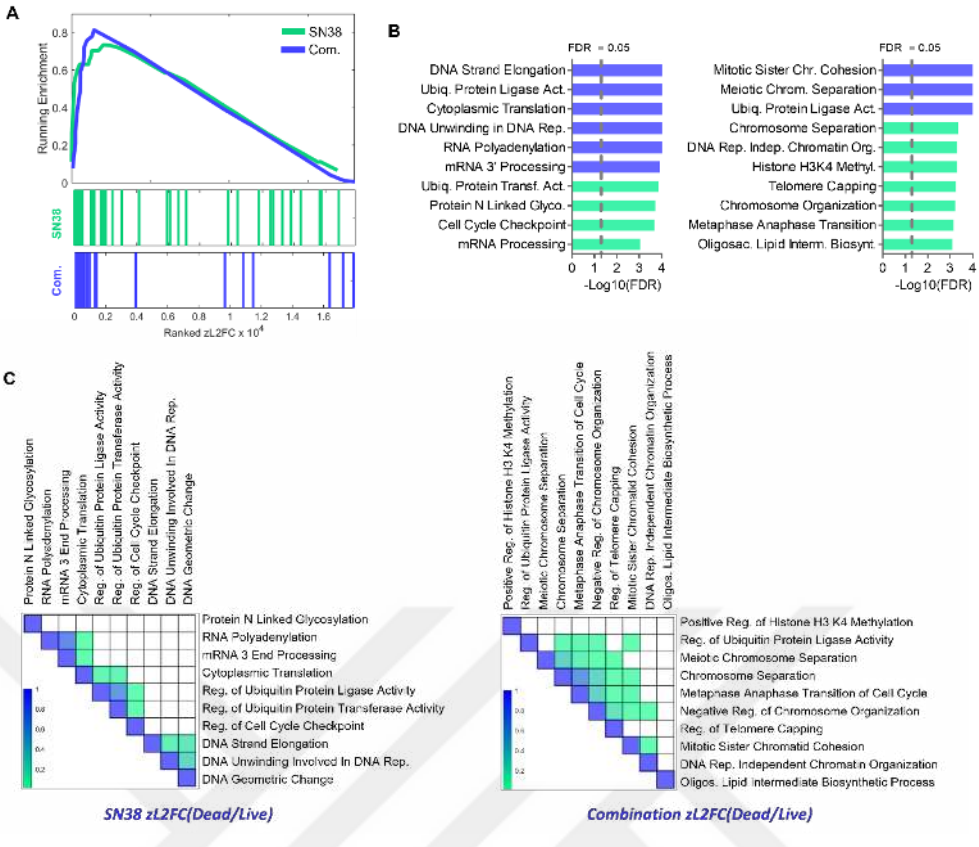

Figure 3.27: GSEA results. A. Enrichment plot of the top GO biological process of SN38 only and combination experiment groups, DNA strand elongation and mitotic sister chromatid cohesion, respectively. B. Ten most enriched GO biological processes in experiment groups treated with either SN38 only (left) or combination (right) based on gene-level fold changes dead cells compared to live cells. The dashed grey line shows the FDR significance cut-off and strongly enriched biological processes (FDR = 0) are indicated by blue. C. Correlation heap-map shows the relationship between the ten most enriched biological processes in dead cells compared to live cells for both treatment groups (left-SN38 only, right-combination). Pearson's correlation coefficient values were obtained from GSEA. Com: combination.

As previously shown, SNU5 parental cells exhibit a similar cell cycle profile under SN38 only and combination treatments applied at the equipotent concentration in the CRISPR screening. However, we observed a notable distinction between GO biological process signatures of SN38 and combination treatment. While three of the top ten signatures significantly upregulated in the

dead population of SN38-treated cells were biologically associated with the S-phase of the cell cycle, five of the ten mostly enriched signatures in the dead population of combination-treated cells were directly linked to the G2/M phase of the cell cycle. This data might indicate that the knockout of specific genes involved in the regulation of different phases of the cell cycle can induce cell death depending on the treatment type. Therefore, we used this hypothesis as a guideline for identifying the first list of candidate genes that differentially affected the cell death/survival rate under SN38 only and combination treatments. However, since the GSEA method uncovers mostly enriched or depleted gene sets, this might lead to a failure to notice a single gene of which knockout differentially affected the cell death/survival rate in only one treatment condition, not the other. For this reason, we generated the first candidate gene list based on the cell death rate differences under both treatments.

We computed the absolute difference between the z-scored gene-level L2FC of dead cells *vs* live cells of SN38 only and the combination treatments group to identify the genes of which knock-out significantly affects cell death or survival. We rank-ordered gene lists based on the absolute difference and selected candidates from the top twenty genes whose absence significantly changed cell death or survival under only one treatment condition (Figure 3.28). We also selected two additional candidates, KEAP1 and AURKB, that dramatically affected cell death/survival in the same direction under both treatments. The correlation between SN38 only and combination treatment groups was 0.368. This data indicated that the mechanisms of action of these treatments involved common features.

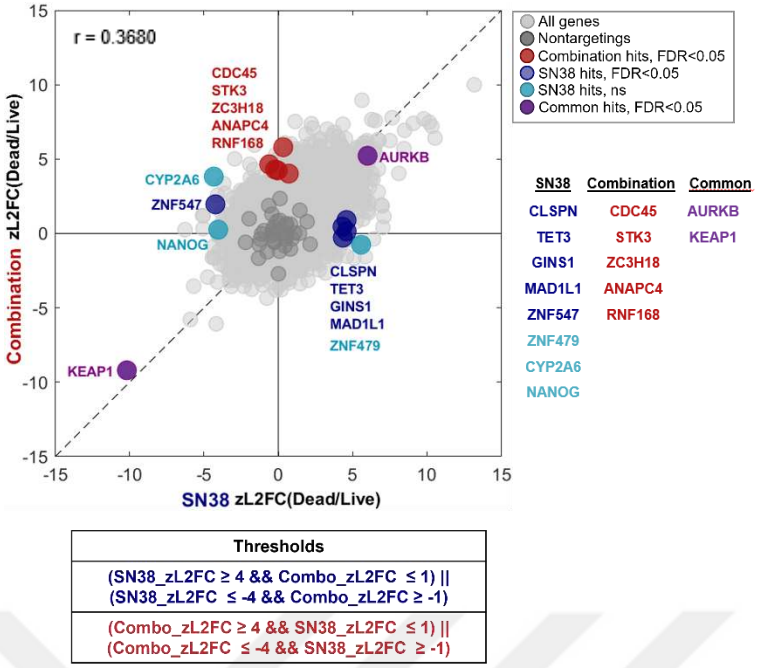

Figure 3.28: Identification of candidate genes of which knockout significantly affected the cell death/survival under SN38 only and/or combination treatment. The cell death rate was assessed by *z*-scored gene-level fold change of dead cells compared to live cells under SN38 only and combination. Knockout of genes shown by dark blue significantly increased the cell death under SN38-only treatment, not combination except for ZNF547. The knockout of ZNF547 increased cell survival. Genes indicated by light blue increase cell death (ZNF479) and survival (NANOG and CYP2A6) when abrogated only in the SN38 treatment condition; however, these effects were not statistically significant (FDR>0.05). Red data points indicate the genes of which knockout dramatically increased the cell death under the combination, not SN38-only treatment. The knockout of AURKB and KEAP1 increased cell death and survival, respectively, under both treatment conditions. *Z*-scored gene-level L2FC thresholds used to calculate the absolute differences of gene-level fold changes are summarized in the table at the bottom. Candidate genes are also listed on the right. Pearson's correlation coefficient between *z*-scored L2FC of dead cells compared to live cells in SN38 only and combination treatment groups was calculated as 0.368.

We selected sgRNAs targeting candidate genes from TKOv3 library to generate the knockout bulk populations. For this purpose, we listed all sgRNAs targeting hit genes by using CRISPick tool (https://portals.broadinstitute.org/gppx/crispick/public) that reports the on-target efficiency score of each sgRNA targeting the corresponding gene. These scores were evaluated along with sgRNA-level L2FC of dead cells compared to live cells to select sgRNAs with the highest on-target efficiency score and L2FC at the expected direction (Figure 3.29).

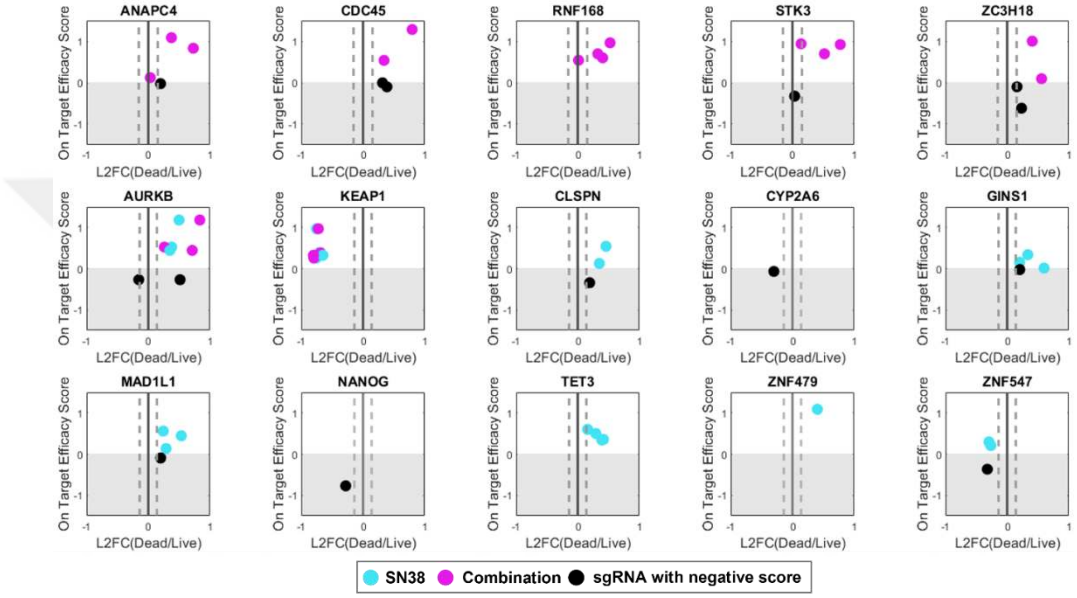

Figure 3.29: Design of the sgRNA targeting corresponding candidate gene by evaluating the on-target efficiency score and sgRNA level L2FC values. SgRNAs targeting genes that affected cell death/survival rate significantly under combination treatment are presented at the top row. The first two graphs at the left of the middle row show sgRNAs of the genes whose knockout differentially altered the cell death/survival rate under both treatments. Other plots represent the sgRNAs of SN38 hit genes. Dashed grey lines indicate the standard deviation, and grey rectangles highlight the area of negative on-target efficiency scores.

We realized that *z*-scored gene-level L2FC scores of CYP2A6, NANOG, and ZNF479 in dead cells compared to live cells were stemmed from only one single guide RNA (Figure 3.29), which can explain why these genes were reported

with insignificant FDR values while collapsing sgRNA-level data into the gene-level scores.

3.5.4 Validation Results of the First Candidate Gene List

CDC45 is a cell division cycle 45 protein. It plays a role in initiating and elongating DNA replication by acting with CLSPN and GINS1, whose knockout increased the cell death rate under SN38-only treatment[171]. It has also been shown that it is involved in DNA damage-dependent signal transduction[172]. Based on the screen results, we found that the knockout of CDC45 gene significantly increased the cell death rate under combination, not SN38-only treatment.

We generated CDC45 knock-out bulk population. For the FLICK assay, cells were treated with serially diluted nine doses of SN38, erlotinib, and combination for five days, the assay length used for generating dose-response curves throughout our study. However, we could not see the differences in the drug response of SNU5-Cas9 (control) and CDC45 knockout cells to SN38 only and combination treatments on day 5 (Figure 3.30).

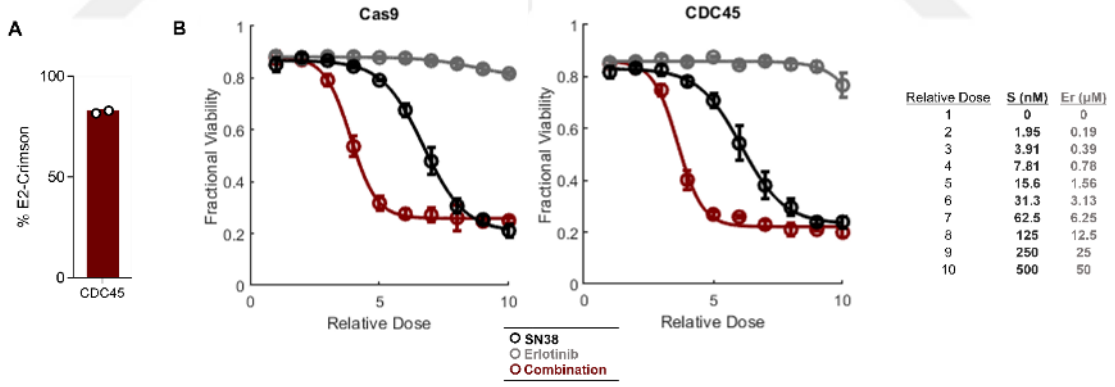

Relative Dose	S (nM)	Er (μM)
1	0	0
2	1.95	0.19
3	3.91	0.39
4	7.81	0.78
5	15.6	1.56
6	31.3	3.13
7	62.5	6.25
8	125	12.5
9	250	25
10	500	50

Figure 3.30: Analysis of CDC45 knockout effect on drug response. A. The percentage of e2-crimson positivity in the CDC45 knockout bulk population on the cell seeding day of FLICK. B. SN38, erlotinib, and combination dose-response curves of SNU5-Cas9 and CDC45 knockout cells on day 5. Doses at corresponding relative doses are listed on the right.

Since we only applied the equipotent doses of SN38 and combination treatments for three days in the CRISPR screening, we wondered whether the drug response of SNU5-Cas9 and CDC45 knockout cells were similar at earlier time points. For this purpose, we calculated the FV metric for day2 and day3 by inferring the size of the live cell population at these time points via the subtraction of kinetically measured dead cell amount from the theoretical total population size. (Figure 3.31).

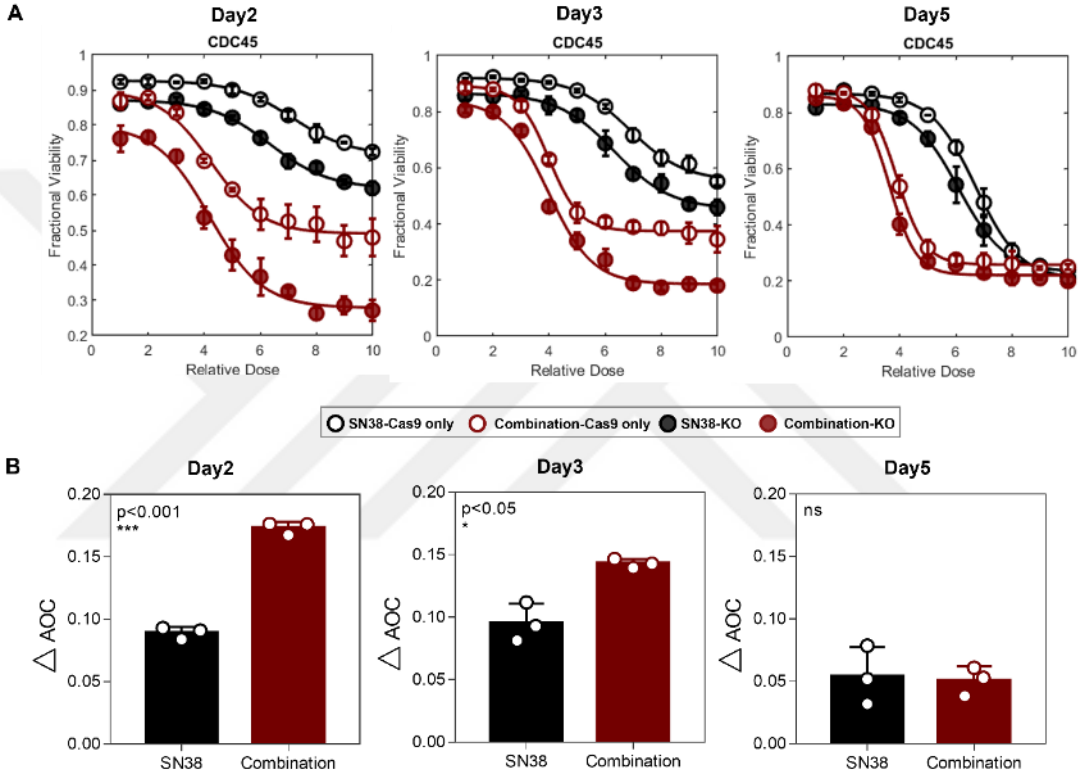

Figure 3.31: Drug response of CDC45 knockout bulk population. A. SN38 only and combination dose-response curves in CDC45 knockout cells compared to SNU5-Cas9 cells on day 2, day 3, and day 5. B. Evaluation of the differential area over the curve (AOC) of SN38 only and combination dose-response curves in CDC45 knockout cells compared to the AOC of the dose-response curve of corresponding treatment in SNU5-Cas9 cells. *P*-values were calculated using Welch's t-test.

We found that CDC45 knockout compared to SNU5-Cas9 cells increased the cell death under the combination treatment according to the dose-response curves generated for day 2 and day 3. We observed enhanced cell death under SN38-only treatment in CDC45 knockout cells compared to SNU5-Cas9 cells. However, CDC45 knockout significantly increased cell death under the combination compared to SN38-only treatment. This data demonstrated that chemo-genetic interactions substantially depended on the time at which drug response was evaluated. We also realized that the degree of gene knockout effect might differ between doses used to generate dose-response curves. Since cells were exposed to the equipotent concentrations of SN38 only and the combination with a different treatment schedule in CRISPR screen as opposed to the experimental setting of FLICK assay, it was not surprising to observe contradictions between the results of these experiments. Such differences can be explained by the drug concentration and treatment duration affecting gene expression signatures and dynamics in intracellular signaling pathways.

RNF168 is an E3 ligase RING finger 168 protein. It has been shown to link homologous recombination to DNA-break-induced chromatin ubiquitylation in S/G2 cells[173]. Based on the results of the CRISPR screen, the knockout of the RNF168 gene enhanced the cell death rate under combination treatment, not SN38 only.

We investigated the effect of RNF168 knockout on the SN38 only and combination responses using the FLICK assay (Figure 3.32). The knockout of RNF168 enhanced the cell death rate under combination treatment compared to SNU5-Cas9 cells on day 2; however, we observed a similar effect in response to SN38-only treatment. The cell death rate in RNF168 knockout cells did not significantly differ between SN38 only and combination treatments as opposed to screen results.

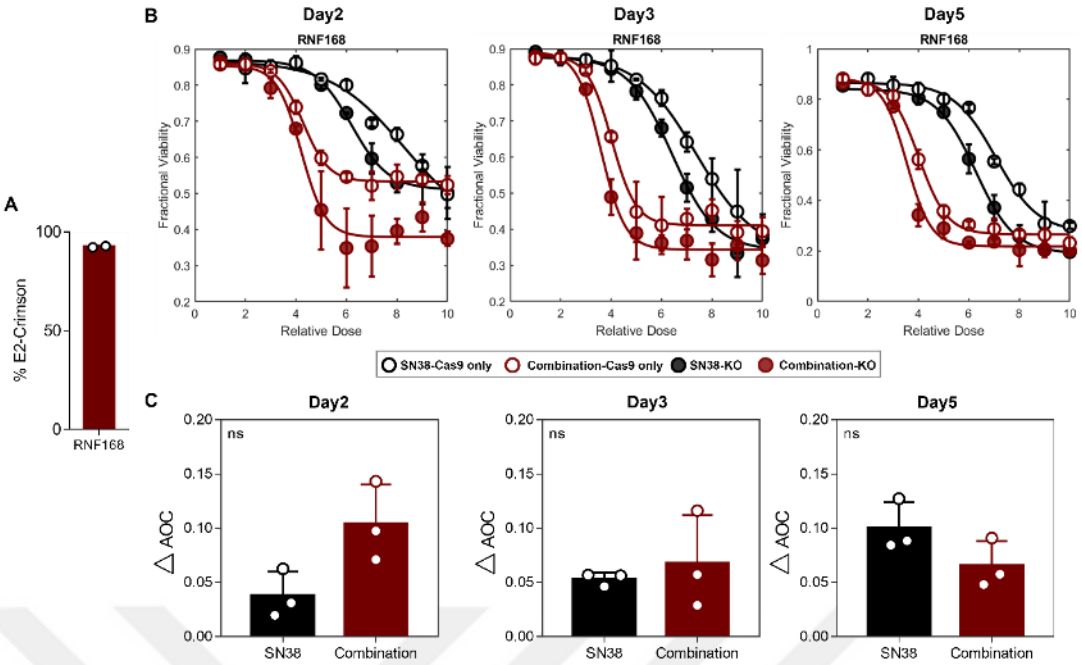

Figure 3.32: Drug response of RNF168 knockout bulk population. A. The percentage of e2-crimson positivity in the RNF168 knockout bulk population on the cell seeding day of FLICK. SN38 and combination dose-response curves in RNF168 knockout cells compared to SNU5-Cas9 cells on day 2, day 3, and day 5. B. Evaluation of the differential area over the curve (AOC) of SN38 only and combination dose-response curves in RNF168 knockout cells compared to the AOC of the dose-response curve of corresponding treatment in SNU5-Cas9 cells. *P*-values were calculated using Welch's t-test.

STK3 is the serine/threonine kinase 3 protein, also known as MST2. It has been demonstrated to promote gastric carcinogenesis by activating Ras-MAPK-mediated cell cycle progression[174]. The knockout of the STK3 gene enhanced the cell death under combination treatment but not SN38 only based on the CRISPR screening results. FLICK experiment results are presented in Figure 3.33.

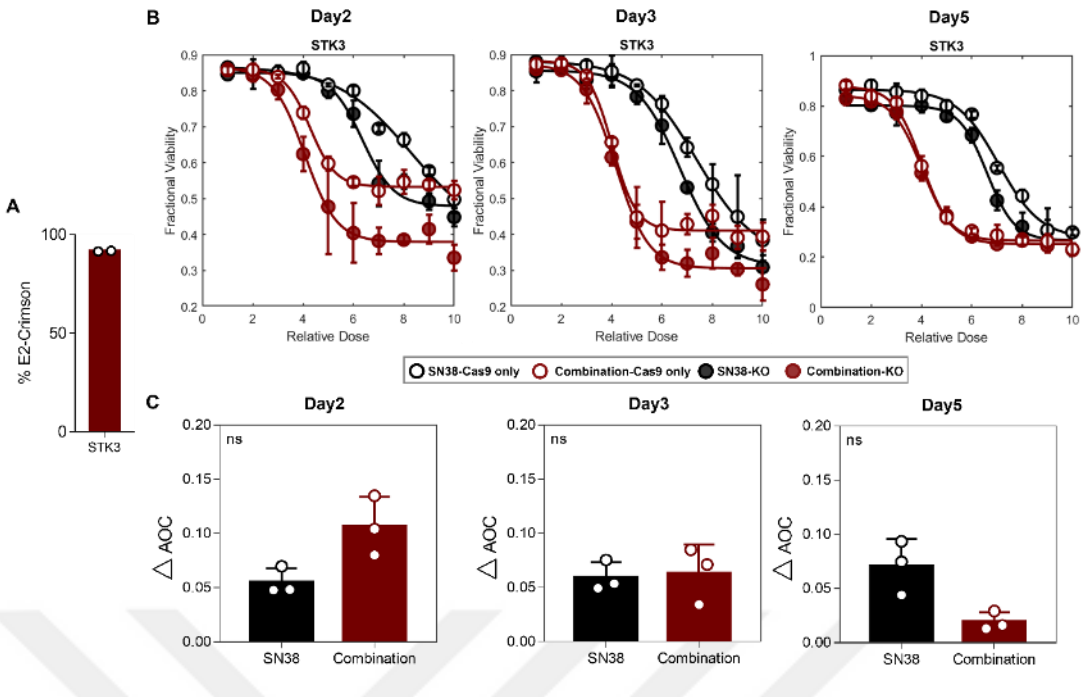

Figure 3.33: Drug response of STK3 knockout bulk population. A. The percentage of e2-crimson positivity in the STK3 knockout bulk population on the cell seeding day of FLICK. SN38 and combination dose-response curves in STK3 knockout cells compared to SNU5-Cas9 cells on day 2, day 3, and day 5. B. Evaluation of the differential area over the curve (AOC) of SN38 only and combination dose-response curves in STK3 knockout cells compared to the AOC of the dose-response curve of corresponding treatment in SNU5-Cas9 cells. *P*-values were calculated using Welch's t-test.

Although the knockout of the STK3 gene caused an increase in cell death in response to combination treatment on day2, we observed a similar result under the SN38-only treatment. In both RNF168 and STK3 knockout cells, we found that the ablation of these genes increased the cell death rate at a similar degree under SN38 and combination treatments. This might stem from the differences between the FLICK assay and the CRISPR screen mentioned above.

We also tested the knockout effect of the other two candidate genes (ANAPC4 and ZC3H18) from the combination hit gene list via FLICK assay. However, based on the dose-response curves, combination treatment failed to elicit a more efficacious response than SN38-only treatment, even at earlier time points. We realized that the e2-crimson positive cells expressing sgRNAs targeting these

genes depleted in the regular culture conditions (Figure 3.34), which indicates that these genes might be critical for cell survival. It remains unknown why these gene knockouts only increased the cell death rate under combination treatment but not SN38.

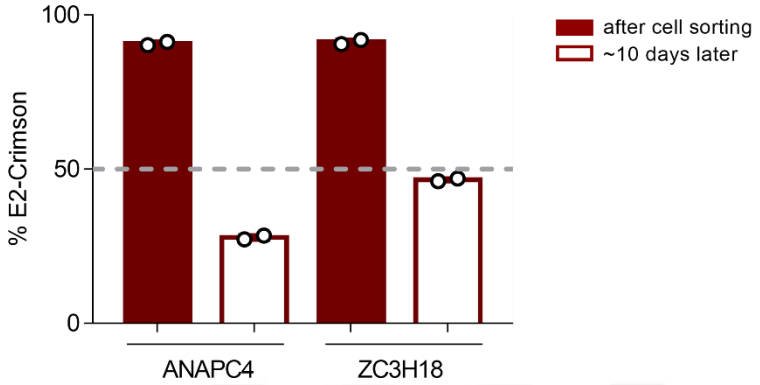

Figure 3.34: Depletion of ANAPC4 and ZC3H18 knockout cells. The percent e2-crimson positivity, an indicator of the cell population size expressing sgRNAs, decreased in ANAPC4 or ZC3H18 knockout bulk populations under the regular culture.

AURKB is aurora kinase B protein that regulates the alignment and segregation of chromosomes during mitosis[175]. It has been demonstrated that it is a critical signaling protein in mitotic DNA damage response that protects cells against DNA damage-induced chromosome segregation errors[175].

According to the results of the FLICK experiment in AURKB knockout and SNU5-Cas9 cells (Figure 3.35) on day 2 and day 3, the ablation of the AURKB gene resulted in enhanced cell death under both treatments, which confirmed the result of CRISPR screening. Dose-response curves for day 2 indicated that knockout of AURKB increased the cell death under combination significantly greater than SN38 only. However, this might be due to the assessment of the shift in the dose-response curve as a function of the gene knockout effect instead of alteration in the drug response at a single dose. Additionally, we observed that e2-crimson-positive cells in the AURKB knockout bulk population exhibited an increase in size followed by depletion under regular culture conditions. This phenomenon could be attributed to cell cycle arrest at the G2/M phase, subsequently leading to cell death.

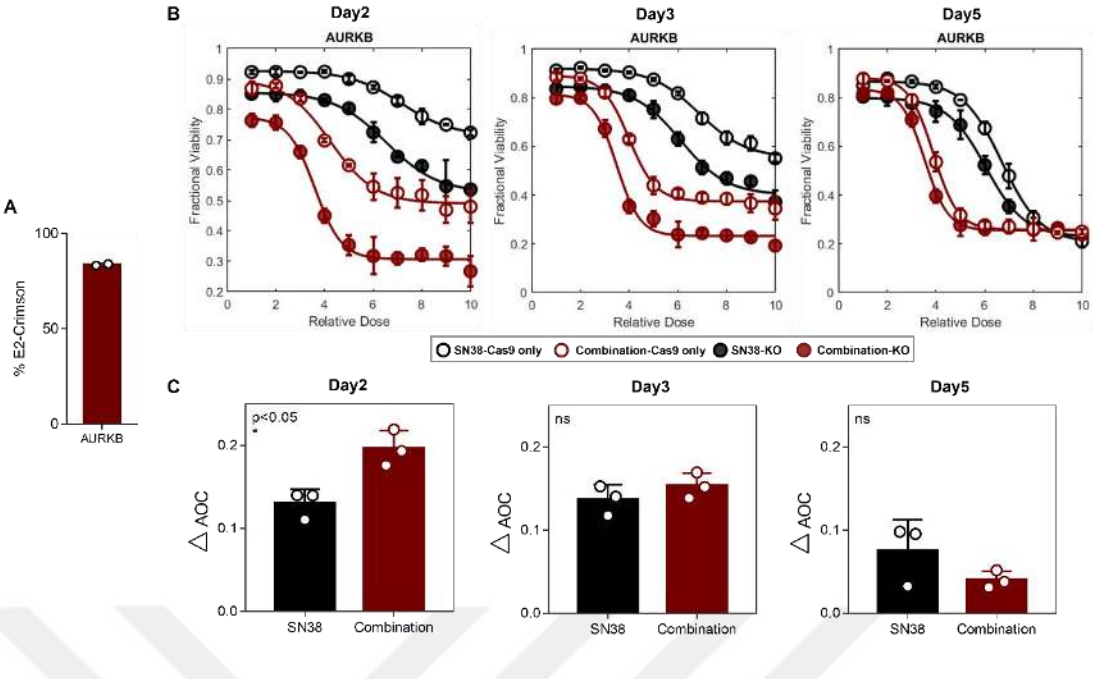

Figure 3.35: Drug response of AURKB knockout bulk population. A. The percentage of e2-crimson positivity in the AURKB knockout bulk population on the cell seeding day of FLICK. SN38 and combination dose-response curves in AURKB knockout cells compared to SNU5-Cas9 cells on day 2, day 3, and day 5. B. Evaluation of the differential area over the curve (AOC) of SN38 only and combination dose-response curves in AURKB knockout cells compared to the AOC of the dose-response curve of corresponding treatment in SNU5-Cas9 cells. *P*-values were calculated using Welch's t-test.

KEAP1 is kelch-like ECH-associated protein 1 and is a substrate adaptor for CUL3-RING ubiquitin ligase enzyme directing NRF2, a transcription factor of anti-oxidant genes, for proteasomal degradation[176]. Studies showed that KEAP1 is also involved in the regulation of DNA damage repair pathways by preventing homologous recombination in the G1 phase of the cell cycle to ensure this repair only occurs between mitotic sister chromatids[177]. In addition to its role in the metabolism of reactive oxygen species and DNA damage repair pathways, studies demonstrated that the knockout of KEAP1 leads to the development of drug resistance against tyrosine kinase inhibitors[178]. Our CRISPR screen result showed that KEAP1 knockout increased cell survival under both SN38 and combination treatments.

Results of the FLICK assay confirmed that KEAP1 knockout significantly increased cell survival under the combination. However, we did not observe a similar effect under SN38-only treatment, as opposed to screen results (Figure 3.36). The reason why its ablation did not improve the cell survival in response to SN38 remains to be solved.

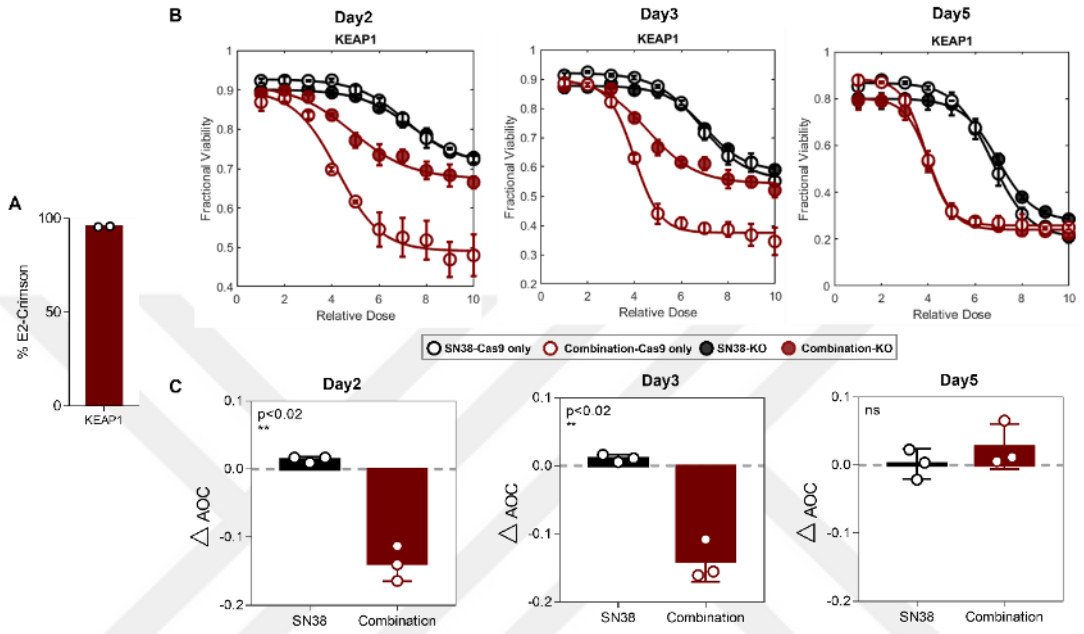

Figure 3.36: Drug response of KEAP1 knockout bulk population. A. The percentage of e2-crimson positivity in the KEAP1 knockout bulk population on the cell seeding day of FLICK. SN38 and combination dose-response curves in KEAP1 knockout cells compared to SNU5-Cas9 cells on day 2, day 3, and day 5. B. Evaluation of the differential area over the curve (AOC) of SN38 only and combination dose-response curves in KEAP1 knockout cells compared to the AOC of the dose-response curve of corresponding treatment in SNU5-Cas9 cells. *P*-values were calculated using Welch's t-test.

Claspin (CLSPN) monitors DNA replication and triggers cell cycle arrest in response to replication stress and DNA damage[179]. It activates DNA repair signaling by interacting with ATR and CHK1[180]. The knockout of CLSPN, a candidate gene in the SN38 hit list, increased the cell death rate under SN38 only, but not combination treatment based on the CRISPR screening results.

According to the results in Figure 3.37, the FLICK assay in SNU5-Cas9 and CLSPN knockout cells failed to confirm the results of CRISPR screen since there was no significant increase in cell death rate under SN38-only treatment compared to the combination.

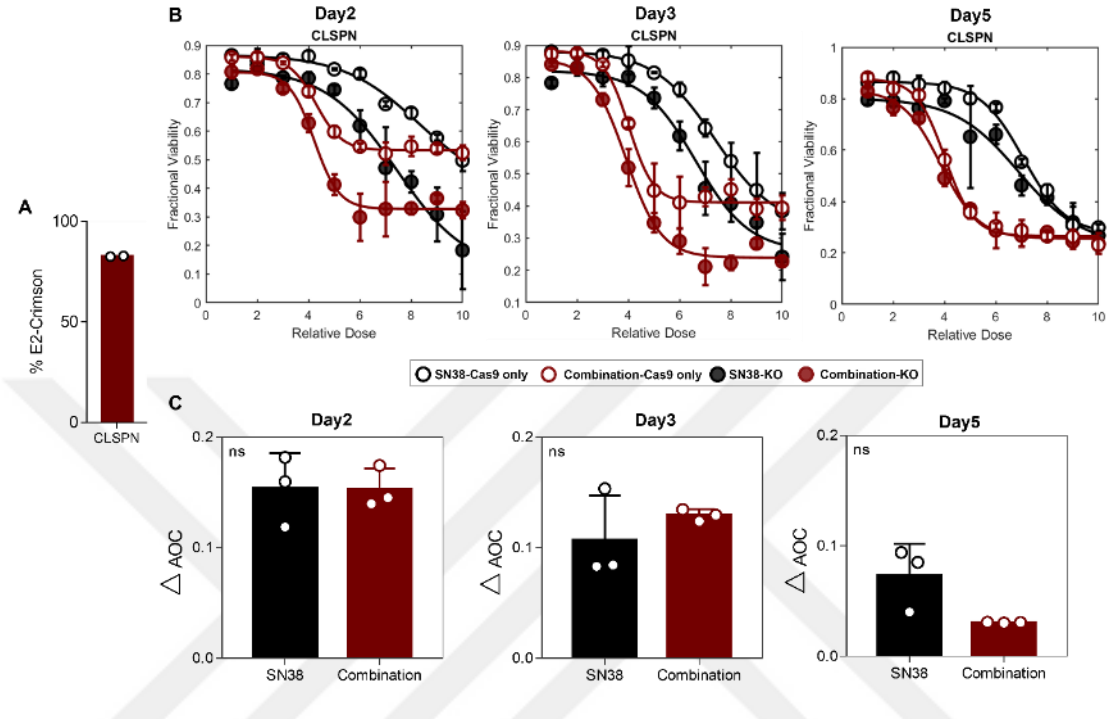

Figure 3.37: Drug response of CLSPN knockout bulk population. A. The percentage of e2-crimson positivity in the CLSPN knockout bulk population on the cell seeding day of FLICK. SN38 and combination dose-response curves in CLSPN knockout cells compared to SNU5-Cas9 cells on day 2, day 3, and day 5. B. Evaluation of the differential area over the curve (AOC) of SN38 only and combination dose-response curves in CLSPN knockout cells compared to the AOC of the dose-response curve of corresponding treatment in SNU5-Cas9 cells. *P*-values were calculated using Welch's t-test.

GINS1 is a member of GINS complex that is involved in establishing and progressing DNA replication fork[181]. It is a critical factor in DNA replication, therefore, cell survival[181]; however, we added it to the SN38 hit list since it is not represented in the core essential gene list[170]. Furthermore, we postulated that the ablation of AURKB might be compensated by the presence of other members within the GINS complex. Our screening results revealed the knockout of the

GINS1 gene only led to a significant enhancement in cell death rate under SN38 treatment.

We showed that the ablation of GINS1 caused a significant increase in the cell death rate under SN38-only treatment on day 5 but not at earlier time points in contrast to previous results (Figure 3.38). We also observed that the percentage of the e2-crimson-positive cell population instantly decreased under the regular culture conditions compared to other knockout bulk populations presented above. This might indicate that GINS1 is a critical protein for the survival of SNU5 cells even though it is not a member of the core essential gene list[170]. However, this raises the question of why the knockout of GINS1 specifically increased the death rate only in the cells treated with SN38, not the combination, which remained elusive.

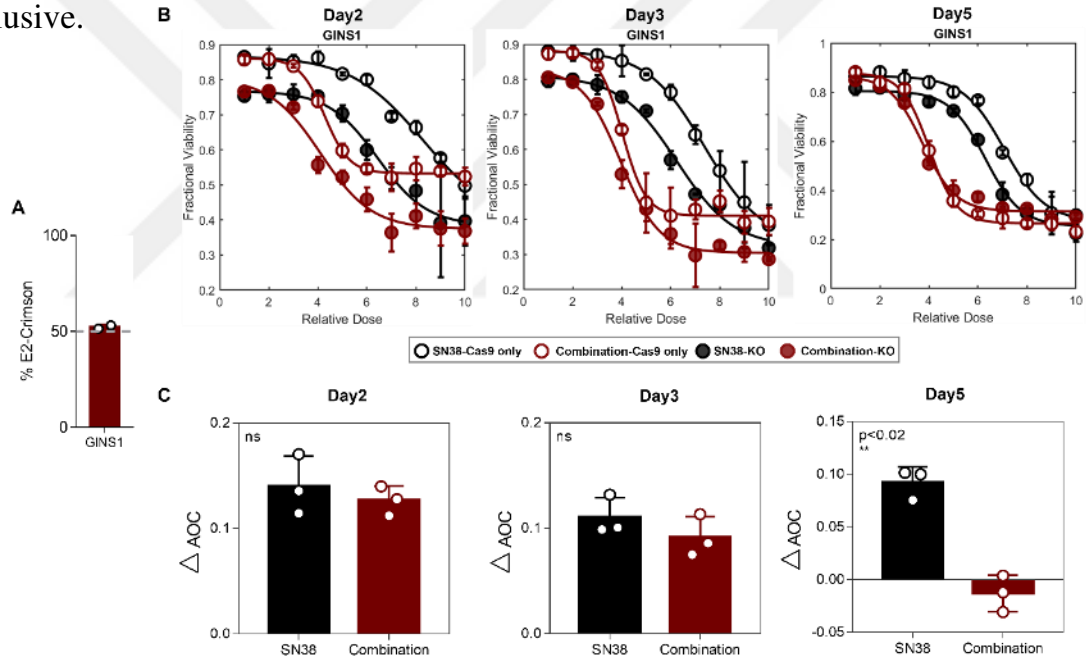

Figure 3.38: Drug response of GINS1 knockout bulk population. A. The percentage of e2-crimson positivity in the GINS1 knockout bulk population on the cell seeding day of FLICK. SN38 and combination dose-response curves in GINS1 knockout cells compared to SNU5-Cas9 cells on day 2, day 3, and day 5. B. Evaluation of the differential area over the curve (AOC) of SN38 only and combination dose-response curves in GINS1 knockout cells compared to the AOC of the dose-response curve of corresponding treatment in SNU5-Cas9 cells. *P*-values were calculated using Welch's t-test.

We also assessed the knockout effect of other SN38 hit genes on the drug response under SN38 only and combination treatments using FLICK assay. As expected, the knockout of the genes (genes indicated by light blue in Figure 3.28) of which *z*-scored gene-level L2FC scores had insignificant FDR values failed to confirm the screen results (data not shown). Although the cell death or survival rate was significantly increased by the knockout of the other three genes (TET3, MAD1L1, and ZNF547) under SN38-only treatment according to the CRISPR screen, we did not observe these effects in FLICK results.

We exposed cells knockout for candidate genes to serially diluted concentrations of SN38 and combination treatments for five days and assessed the effect of gene knockout on drug response using FLICK assay in the initial validation experiments, as mentioned above. However, the single dose of SN38 only and combination treatments inducing a similar degree of cell death was applied for three days in the CRISPR screening. Discrepancies between the FLICK assay and the CRISPR screen might explain the failure in these validation experiments.

We performed the following validation experiments under screen conditions by analyzing annexin-V positivity, used to obtain dead cell fraction in the screen. In addition, cell populations knockout for selected candidate genes, cells expressing sgRNA that targeted either TOP1 or TOP2A were generated and incorporated as additional controls since TOP1 is the primary target of SN38. In these experiments, we used either SNU-Cas9 cells or cells that expressed sgRNA targeting LacZ gene as an untargeted control group. The equipotent concentration of SN38 only and combination were applied to these cell populations for three days, followed by the evaluation of annexin-V positivity (Figure 3.39). Based on the results, the level of annexin-V positivity, therefore cell death, significantly decreased in KEAP1 knockout population compared to control cells under both treatments, which confirmed the screen results. As expected, the absence of TOP1 caused a decrease in annexin-V positivity under these treatments. However, other knockout cell populations failed to reveal differences between SN38 and

combination treatments. Moreover, the degree of cell death in these populations was similar to control cells, which might be explained by the depletion of cells expressing sgRNA for certain knockout populations, including AURKB and CLSPN. However, these results indicated variations in CRISPR screening data and underscored the requirement for another candidate list involving significantly enriched or depleted genes.

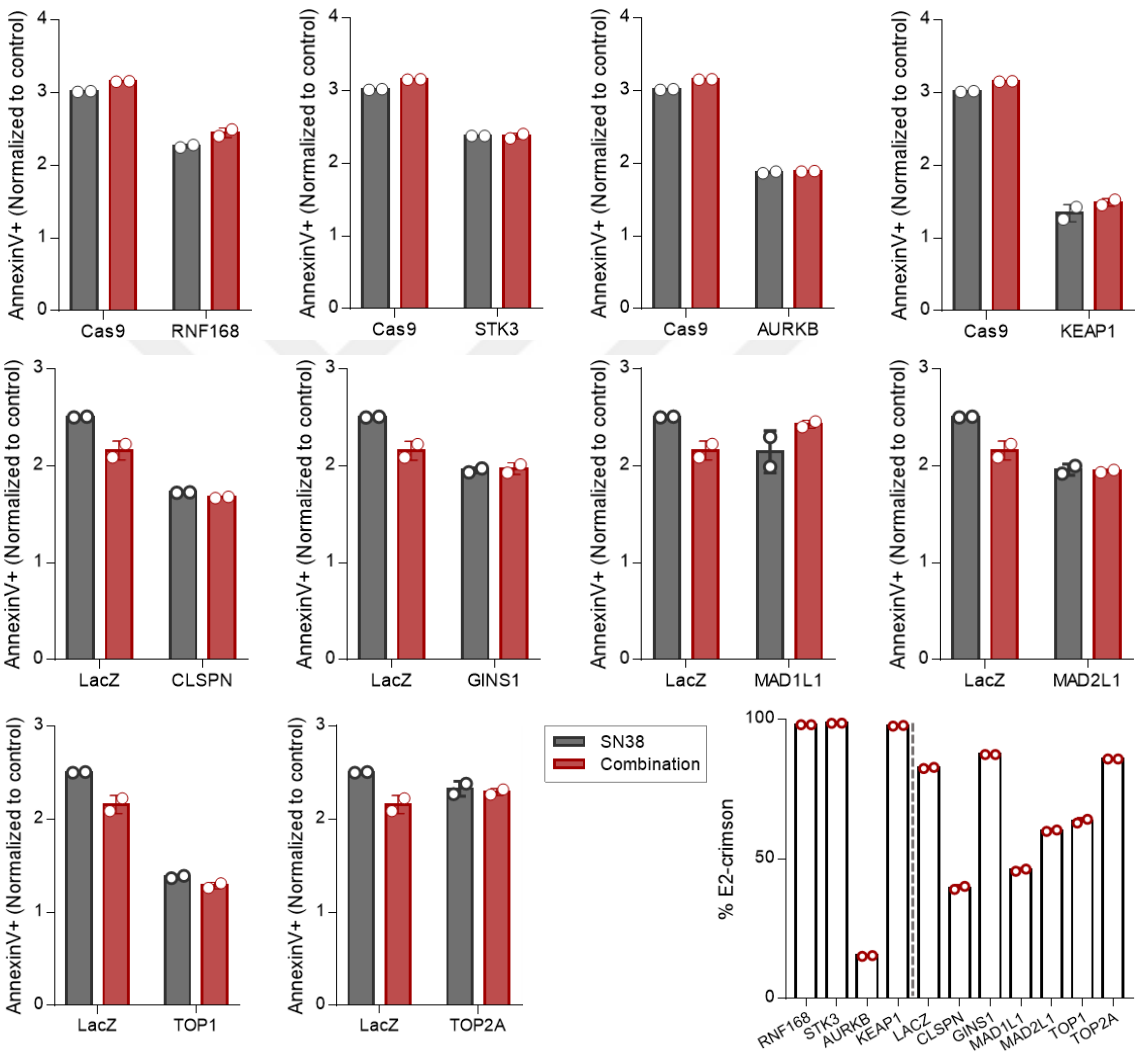

Figure 3.39: Evaluation of annexin-V positivity in cell populations knockout for candidate hit genes. Annexin-V positivity was analyzed in indicated cell populations compared to controls, treated with equipotent concentrations of SN38 and combination. The graph at the bottom right shows e2-crimson positivity in knockout bulk populations.

3.5.5 Validation Results of the Second Candidate Gene List

We generated the second candidate gene list to reveal the differences in cell death mechanisms induced by SN38 and combination treatments. Although *z*-scored gene level L2FC of dead fraction normalized the live was analyzed to determine candidate genes, we observed that the knockout of some candidate genes in the first list affected cell viability. This caused the depletion of these cell populations in regular culture conditions. Given this, we determined the second candidate gene list based on both significance and the level of depletion of these genes in untreated control normalized to *T0* input sample for feasibility (Figure 3.40)

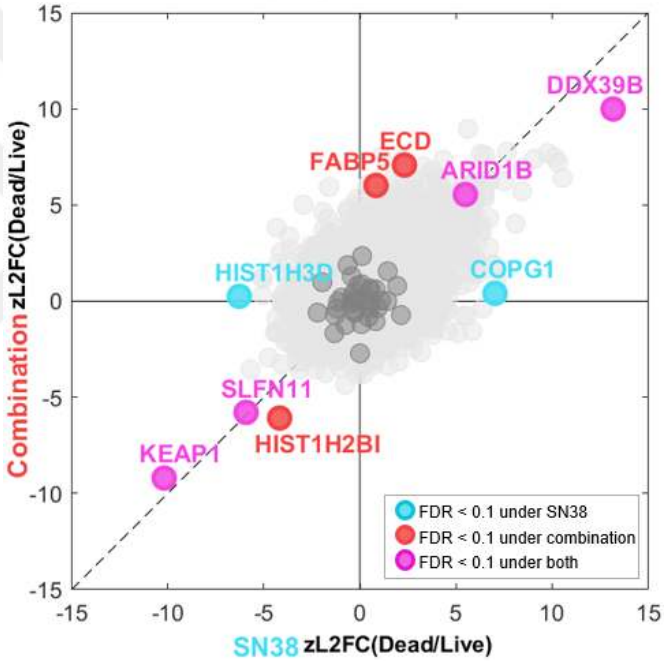

Figure 3.40: Identification of second candidate genes of which knockouts significantly affected the cell death/survival under SN38 only and/or combination treatment. The cell death rate was assessed by *z*-scored gene-level fold change of dead cells compared to live cells under SN38 only and combination. Blue, red, and purple colors indicate genes of which knockouts significantly affected cell death/survival under SN38 only, combination, and both treatments, respectively (FDR<0.1).

We conducted the FLICK assay to validate the effect of gene knockouts on the response to SN38 combination treatments applied at equipotent doses. LF metric was used to determine the alterations in the degree of cell death in knockout populations compared to the control (Figure 3.41). We observed that the gene knockouts that increased cell death or survival under both treatments confirmed the screen results. For instance, the knockout of ARID1B gene enhanced the cell death under both treatments according to the screen, which was confirmed by FLICK results based on the quantification of maximum LF values. However, gene knockouts that affected cell death or survival differentially under SN38 and combination treatments failed to validate the screen results. It can be exemplified by the unchanged cell death rate of HIST1H3D knockout cell population, which was expected to decrease under SN38 only, but not combination treatment according to screen results. Moreover, we validated these results further using a competition assay (Figure 3.42).

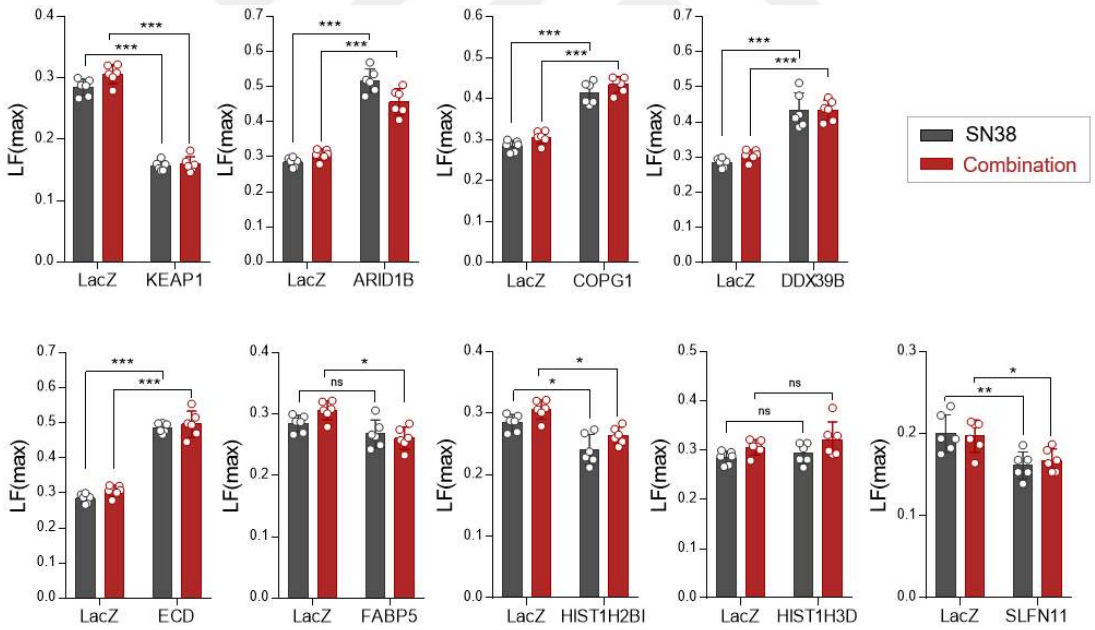

Figure 3.41: Investigation of the knockout effect of second candidate genes on drug response via FLICK. LF analysis shows alterations in the cell death rate of knockout populations compared to LacZ control cells in response to equipotent doses of SN38 and combination treatments. Dunnett's multiple comparison test was used to determine statistical significance based on adjusted *p*-values. *** <0.001,* <0.033, ns: non-significant.

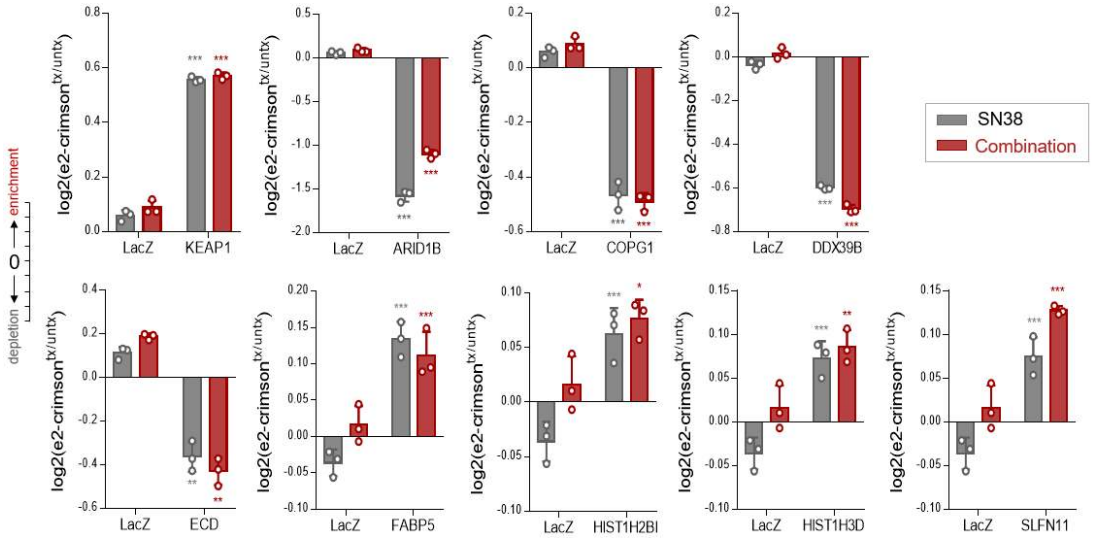

Figure 3.42: Results of competition assay that show the fitness of cells knockout for indicated genes under SN38 and combination treatments applied at equipotent concentration. Statistical significance based on adjusted *p*-values was determined using Dunnett's multiple comparison test for all graphs, except for the graph at the bottom left, evaluated by unpaired t-test with Welch's correction. *** <0.001,** 0.002, * 0.033, ns: non-significant.

In addition to validation experiments at equipotent concentrations, we evaluated the alterations in drug response to a range of SN38 and combination concentrations using FLICK assay. As opposed to other candidate genes, cells knockout for ARID1B and SLFN11 genes showed enhanced sensitivity and resistance to SN38 and combination, respectively, based on the alteration in the potency of the corresponding treatment (Figure 3.43).

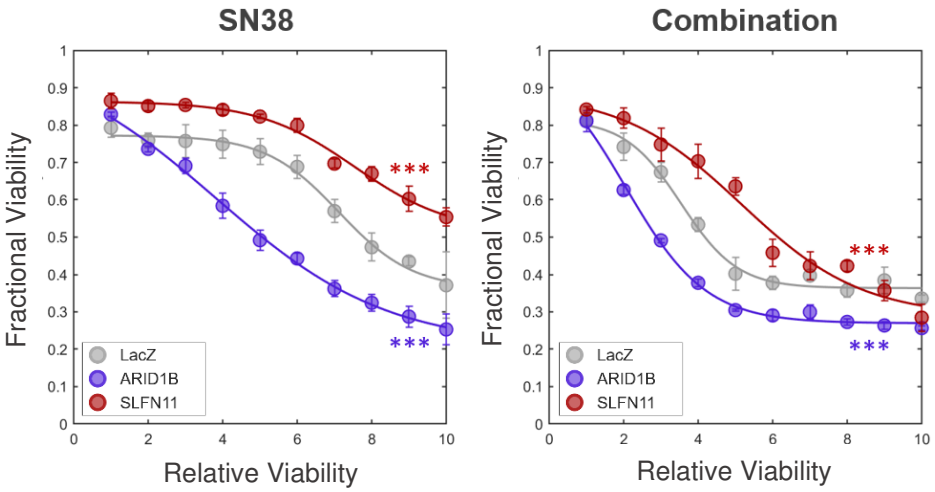

Figure 3.43: Fractional viability of ARID1B and SLFN11 knockout bulk populations. Drug response of cell populations knockout for ARID1B (blue) and SLFN11 (red), and LacZ (grey) was assessed using the FV metric. The area over the curve (AOC) metric of curves of knockout and control populations was compared using Dunnett's multiple comparison test. *** <0.001.

We investigated the differences in cell death dynamics of ARID1B and SLFN11 knockout populations by analyzing LF curves. We first defined the concentration of SN38 and combination treatments that induced cell death at the same rate based on the LF curve of control cells (Figure 3.44A). We then compared LF curves of knockout and control populations by evaluating death rate associated parameters, including LF_{max}, the death onset time, and area under LED curves (Figure 3.44B). These results confirmed that the knockout of ARID1B and SLFN11 resulted in increased and decreased cell death rates, respectively.

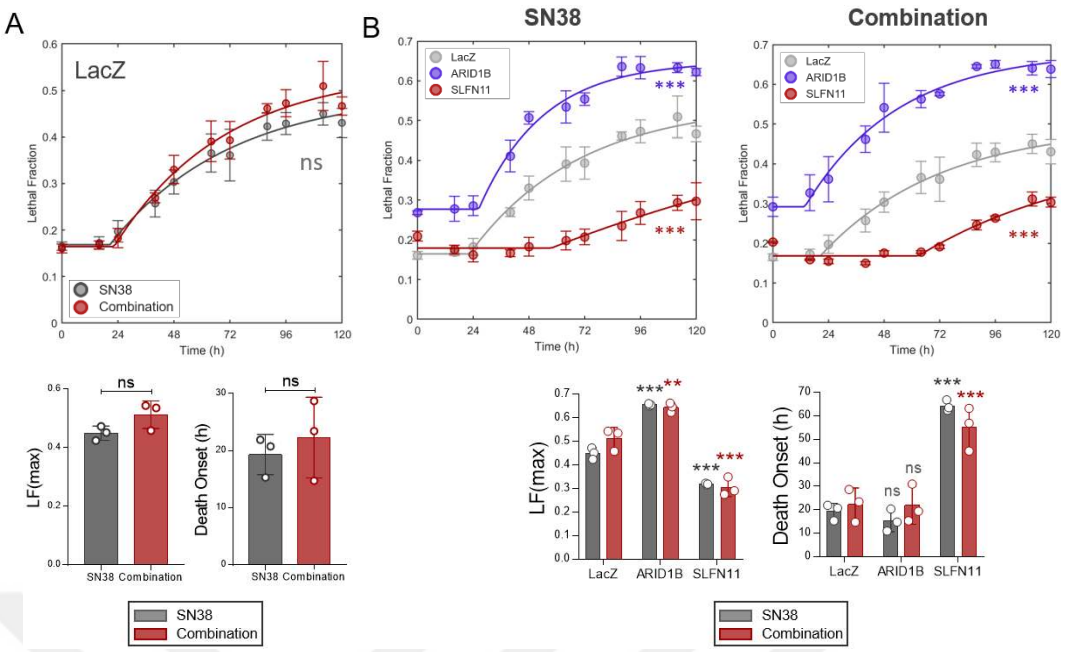

Figure 3.44: LF analysis in ARID1B and SLFN11 knockout bulk populations.A. Determination of SN38 and combination concentrations that induced cell death at the same rate (LF=0.5 at the end of the assay). Statistical testing was performed using an unpaired t-test with Welch's correction. ns: non-significant. B. Evaluation of LED curves of ARID1B and SLFN11 knockout populations compared control cells. Using Dunnett's multiple comparison test, statistical significance based on adjusted p-values was determined. *** <0.001,** 0.002, ns: non-significant. Indicators of statistical significance on the LED plots represent the comparison of area under the curve values.

Results of validation experiments, including FLICK and competition assays clearly indicated that knockout of genes that affected cell death or survival in the same direction under both treatments confirmed the screen results. This data suggested that SN38 and combination might have the same mechanisms of action and activate apoptotic cell death by employing the same cell signaling pathways. However, investigating chemo-genetic interactions for only a few genes might not suffice to consolidate this hypothesis. Therefore, RNAi-based signature assay that provides both statistical and biological generalization for anti-cancer agents was

used to test whether SN38 and combination exhibit the same mechanisms of action.

3.6 Utilization of RNAi-based Signature Assay to Explore Combination Mechanisms of Action

We conducted RNAi-based GFP competition assay to characterize combination mechanisms of action. We generated the signature of SN38, erlotinib, and combination by assembling RIs for each cell population expressing one of 8 shRNAs, which was then compared to a reference set using the modified K-NN algorithm[162] (Figure 3.45, top, signatures of all replicates are presented in Figure 5.10). Here, equipotent doses of SN38 and erlotinib were combined to achieve the same degree of cell killing induced by each single component drug. SN38 and combination were significantly classified as TOP1 poisons with LR values of 0.94 and 1, respectively. Thus, this analysis unveiled that the combination operated through the same mechanism of action as SN38, as indicated by both biological and statistical classifications.

We performed principal component analysis as another means of the data illustration to examine the variance in fewer dimensions (Figure 3.45, bottom). Categories of treatments tested and three other categories from the reference set were plotted, which clearly demonstrated the separation of EGFR inhibitors and TOP1 poisons along the first principal component (PC1). Analysis of the coefficients of the original variables from which PC1 was constructed showed that shChk2 strongly contributed to PC1 compared to other hairpins. This data indicated combination, like other members of TOP1 and TOP2A poisons, induced DNA damage response, as Chk2 is one of the key regulators of the signaling cascade that conveys the DNA damage signal to various downstream effectors.

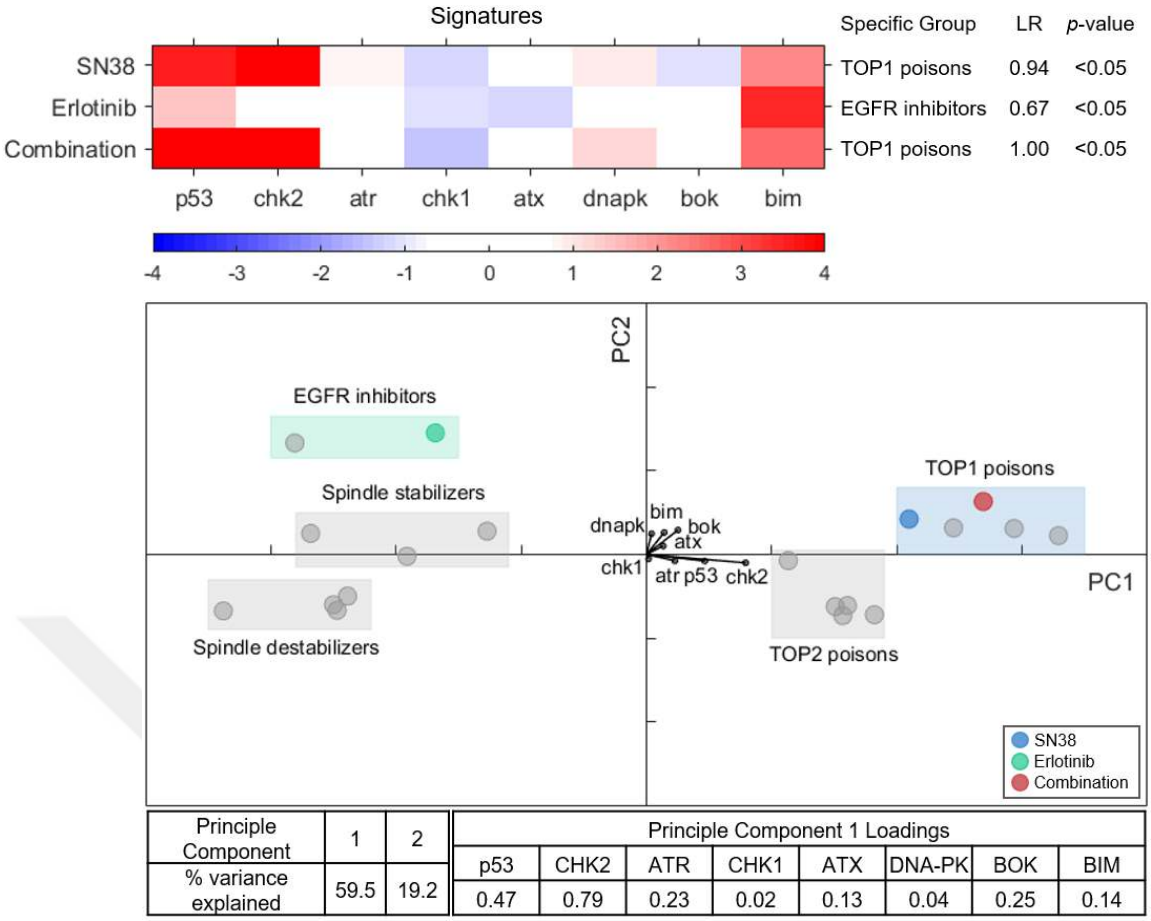

Principle Component	1	2
% variance explained	59.5	19.2

Principle Component 1 Loadings							
p53	CHK2	ATR	CHK1	ATX	DNA-PK	BOK	BIM
0.47	0.79	0.23	0.02	0.13	0.04	0.25	0.14

Figure 3.45: RNAi-based GFP competition assay. The heatmap and table at the top show the signatures of each treatment and corresponding categories with statistical values. The PCA plot at the bottom represents the results of the PCA analysis performed with the classes of TOP1 poisons, EGFR inhibitors, TOP2A poisons, spindle stabilizers, and destabilizers. As a means of visualization, the estimated spatial position of each category within the PCA is highlighted by boxes. The percentage variance explained by each principal component and PC1 loadings is presented in tables.

We also assessed the pharmacological interaction in the combination in Eμ-Myc Cdkn2a$^{Arf-/-}$ leukemia cells used as a model cell line in the signature assay. Combination elicited a strong synergistic effect in these cells (Figure 3.46).

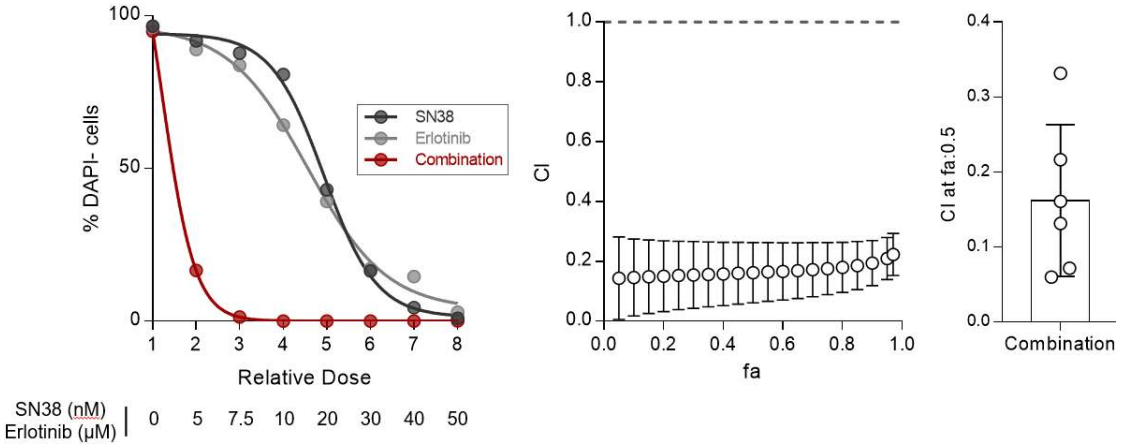

Figure 3.46: Pharmacological interaction in combination applied to Eμ-Myc cells. Dose-response curves (left), CI-fa plot (middle), and CI at fa:0.5 (right) are presented.

3.7 Examination of Drug Response to the Dual Combination of SN38 and other EGFR Inhibitors

Gefitinib, afatinib, and osimertinib are the first, second, and third-generation EGFR inhibitors that target the kinase activity of wild-type and various mutants of EGFR at different le vels of potencies. Lapatinib, a first-generation EGFR inhibitor, acts as a dual inhibitor of EGFR and HER2. We tested the dual combination of SN38, these EGFR inhibitors, and erlotinib to understand whether these combinations elicit synergistic effects. FV analysis showed that dual combinations of SN38 and EGFR inhibitors achieved an enhanced drug response compared to single agents in parental cells, except for the combination including osimertinib (Figure 3.47, top panel). We also observed similar drug responses in two different $SNU^{EGFR\text{-}KO}$ cell models; however, a slight alteration in response to the combination of SN38 and osimertinib was observed (Figure 3.47, middle and bottom panels). This data indicated that the dual combination of SN38 and EGFR inhibitors, but not osimertinib, exerted its effect without targeting EGFR activity.

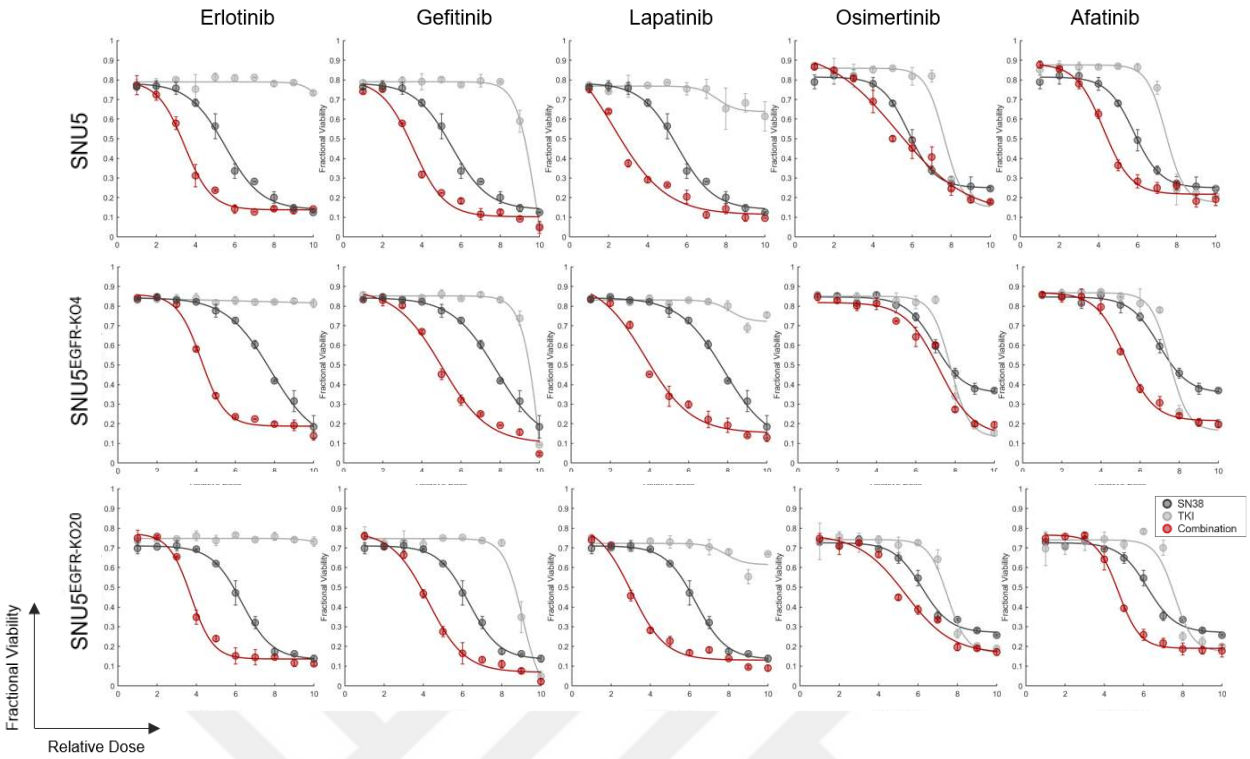

Figure 3.47: Drug response analysis in SNU$^{EGFR-KO}$ cell models.Drug response to the dual combination of SN38 and EGFR inhibitors was investigated in SNU5 (top panel) and SNU$^{EGFR-KO}$ cell models (middle and bottom panels).

The assessment of pharmacological interactions demonstrated that these dual combinations elicited a strong synergistic effect in SNU5 cells, except for the SN38 and osimertinib combination, which showed an additive effect (Figure 3.48).

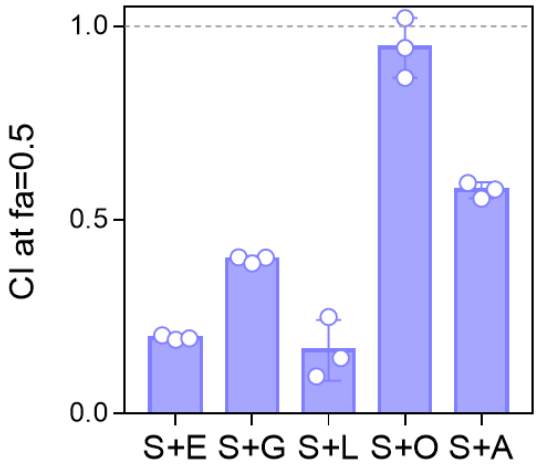

Figure 3.48: Evaluation of pharmacological interactions in the dual combination of SN38 and EGFR inhibitors. S: SN38. E: Erlotinib. G: Gefitinib. L: Lapatinib. O: Osimertinib. A: Afatinib.

As mentioned above, the drug response to dual combinations did not differ between parental and $SNU^{EGFR\text{-}KO}$ cells. This data suggested that EGFR inhibitors, except for osimertinib showed their inhibitory effect on another target but not EGFR. To further confirm these results, we examined alterations in the extracellular signal-regulated kinase (ERK) phosphorylation level upon treatment with EGFR inhibitors in a time-dependent manner since it is a critical downstream target of the EGFR signaling pathway[182]. Immunoblot analysis showed that ERK activity remained unchanged under the treatment of EGFR inhibitors, except for osimertinib (Figure 3.49A). The degree and kinetics of ERK phosphorylation under gefitinib, lapatinib, and afatinib were not different than erlotinib that slightly decreased the phosphorylation at the earlier time points, which was then recovered immediately after 4h. However, osimertinib drastically inhibited the ERK activity compared to other EGFR inhibitors, especially at 24h. Moreover, the correlation between the degree of relative ERK phosphorylation at 24h and CI showed that the inhibition of EGFR signaling interfered with the synergistic effect in the dual combination of SN38 and EGFR inhibitors in SNU5 cells (Figure 3.49B).

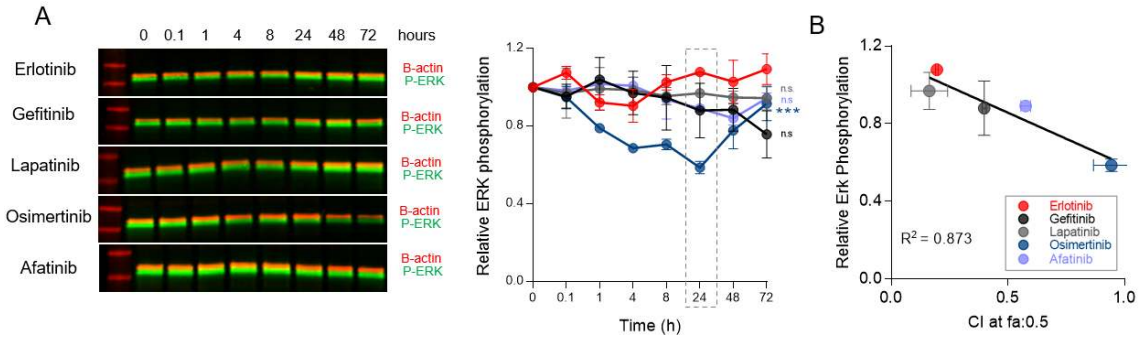

Figure 3.49: Alteration in ERK phosphorylation. A. Immunoblot analysis of time-dependent alterations in ERK activity under treatment with EGFR inhibitors. The graph at the right shows the quantification of immunoblot data. Statistical significance based on adjusted *p*-values was determined using Dunnett's post hoc analysis. ***<0.001, ns: non-significant. The dashed box indicates the time point when a significant decrease in ERK phosphorylation was observed under osimertinib compared to other EGFR inhibitors. B. Correlation between the degree of ERK phosphorylation and CI at fa:05 value of dual combinations of SN38 and EGFR inhibitors.

Analysis of changes in ERK activity in the presence of EGFR inhibitors demonstrated that these agents, except for osimertinib inhibited another target than EGFR in SNU5 cells. This data also suggested the off-target of these agents is unlikely to be other receptor tyrosine kinase(s) (RTK) since ERK is a common downstream kinase regulated by RTK-induced intracellular signaling pathways. Studies in the literature revealed that efflux pumps might be the off-target of EGFR inhibitors[183,184]. In the next step, we inspected the screen results in light of this information to understand whether synergy elicited by the combination of SN38 and erlotinib is associated with the inhibition of efflux pump activity by erlotinib.

3.8 Identification of Erlotinib Off-target

Given that previous studies identified specific types of efflux pumps as off-targets of EGFR inhibitors, we re-assessed the screen results to understand whether the knockout of any efflux pump altered the cell death or survival rate under SN38 only and combination treatments. According to the screen data, the abrogation of

the ABCG2 efflux pump enhanced the cell death rate under both treatments (Figure 3.50A). It is a member of the ATP-binding cassette (ABC) transporter superfamily, also known as breast cancer resistance protein (BCRP)[185]. Based on the publicly available data set, we found that SNU5 cells highly express ABCG2 efflux pump compared to various gastric cancer cell lines (merav.wi.mit.edu/) (Figure 3.50B).

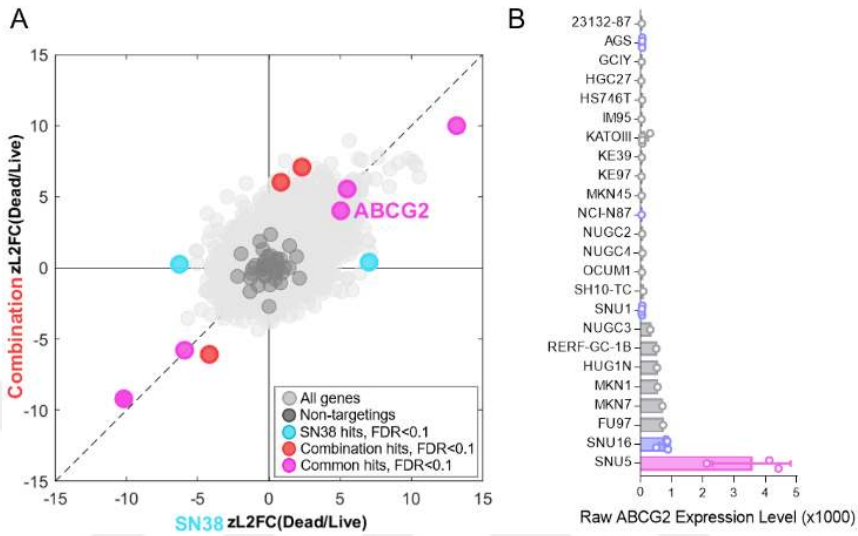

Figure 3.50: Abrogation and expression of ABCG2 in SNU5 cells. A. The screen result that shows an enhanced cell death rate under SN8 only and combination treatments in the absence of ABCG2. B. ABCG2 expression level in different gastric cancer cell lines according to the publicly available data set (merav.wi.mit.edu/).

We first analyzed the drug response to the dual combination of SN38 with different ABCG2 inhibitors using the FV metric. We observed that combinations involving ABCG2 inhibitors achieved enhanced drug response in SNU5 cells, compatible with the response to SN38 and erlotinib combination (Figure 3.51A). The combination of SN38 with verapamil, an ABCB1 inhibitor, was also evaluated to investigate the specificity of drug response to ABCG2 inhibition, as ABCB1, also known as multidrug resistance (MDR) protein, is another member of the ATP-binding cassette (ABC) transporter superfamily, frequently upregulated in the concept of chemotherapy resistance. Incorporating verapamil in the combination did not further enhance the response compared to the SN38-only treatment (Figure

3.51B). This data suggested that synergy in SN38 and erlotinib combination might be specifically dependent on the inhibition of ABCG2 efflux pump activity.

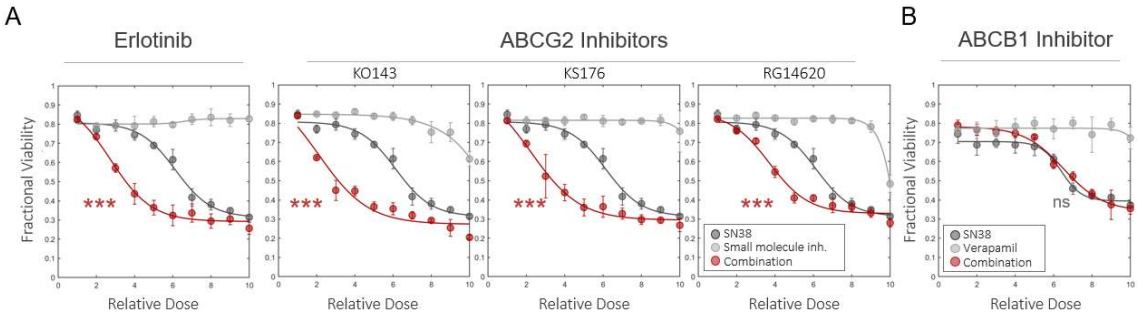

Figure 3.51: Pharmacological inhibition of ABCG2 and ABCB1 in the presence of SN38. A. FV analysis for dual combinations including SN38 and erlotinib or different ABCG2 inhibitors specified at the top of each graph. The AOC of SN38 and combinations shown in this panel was compared using Dunnett's multiple comparison test reporting *p*-values. ***<0.001. B. FV analysis of SN38 and verapamil single agents, and the combination. Welch's t-test was used to calculate the *p*-value for the AOC comparison of SN38 and combination. ns: non-significant.

CRISPR screening data indicated that the knockout of ABCG2 enhanced the cell death rate under both treatments. To confirm this result, we generated ABCG2 knockout bulk population (Figure 5.11) and performed FLICK to assess the degree of cell death over time. Control cells and ABCG2 knockout bulk population were continuously treated with the equipotent concentrations of SN38 and combination for feasibility. This data demonstrated that ABCG2 knockout increased the drug-induced cell death under both treatments (Figure 3.52A). Since cells were exposed to nearly 3.6-fold more SN38 only at the concentration achieving the same potency with the combination, it led to a higher degree of cell killing in the absence of ABCG2, as expected.

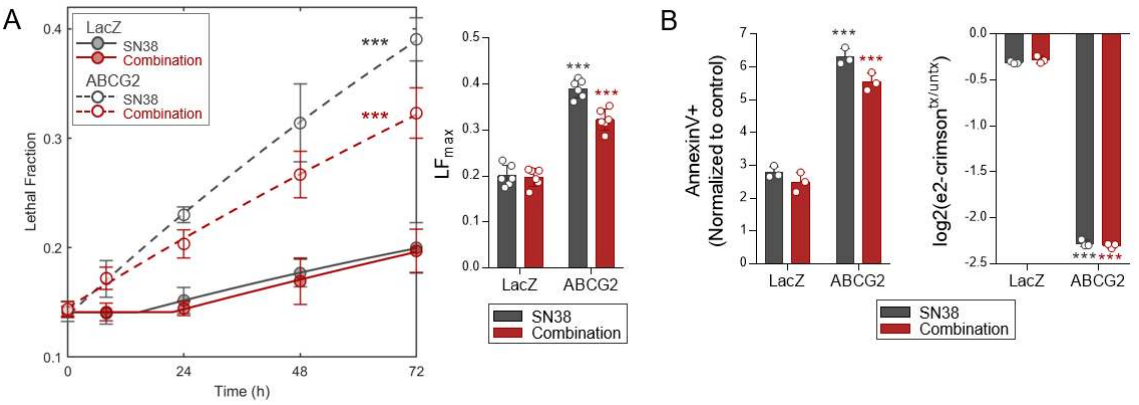

Figure 3.52: Validation of ABCG2 knockout. A. Investigation of drug-induced cell death in ABCG2 knockout and control cells treated with SN38 and combination at the equipotent concentrations by analyzing LF metric. Asterisks on the left graph indicate the comparison of the AUC value of the ABCG2 knockout population with the control for each treatment. B. Results of annexin-V positivity and competition assays. For both panels, Welch's t-test was used for statistical analysis. ****p*-value<0.001.

We evaluated annexin-V positivity since the experimental setting allowed establishing the same experimental conditions used in the screen, including the application of intermittent treatment and the quantification of cell death based on the cell surface marker. Results obtained from this experiment further confirmed the screen data (Figure 3.52B). Moreover, the fitness of the ABCG2 knockout population under SN38 and combination treatments was analyzed using competition assay. The findings of this experiment demonstrated that the survival ability of knockout cells under these treatments was significantly impaired compared to control cells (Figure 3.52B).

We analyzed the FV metric to inspect drug response to SN38 and combination at serially diluted concentrations in ABCG2 knockout and control cells. Results of this analysis demonstrated that the knockout of ABCG2 completely recapitulated the pharmacological inhibition of the protein by erlotinib, as the response to combination in control cells failed to differ from the response to SN38 in ABCG2 knockout cells (Figure 3.53).

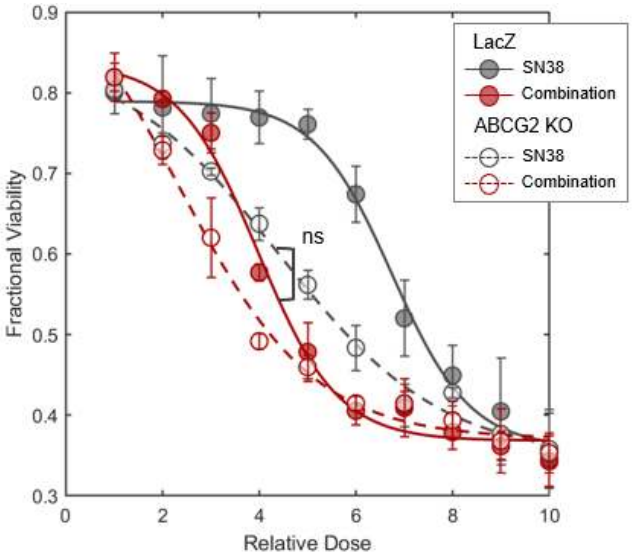

Figure 3.53: FV analysis in ABCG2 knockout cells. Drug response of ABCG2 knockout and control cells to SN38 and combination was analyzed using the FV metric. Statistical analysis was performed using Welch's t-test to compare AOC values of SN38 response in ABCG2 knockout cells and combination response in control cells. ns: non-significant.

We investigated the alteration in the ABCG2 efflux pump activity under erlotinib treatment using the Hoechst-33342 assay. Osimertinib was employed as a negative control treatment since the drug response (Figure 3.47) and immunoblot findings (Figure 3.49) suggested that osimertinib was the only EGFR inhibitor with an on-target action. KO143, a potent ABCG2 inhibitor known as fumitremorgin C, was used as a positive control. SNU5 cells were exposed to Hoechst-33342, a specific substrate for ABCG2[186], in the presence of each inhibitor. At the end of the incubation, cells were taken to the fresh media while maintaining the drug condition. The percent population negative for Hoechst-33342 was interpreted as the function of the ABCG2 efflux pump.

Results of the Hoechst-33342 assay proved that erlotinib inhibited the ABCG2 efflux activity, but not as strong as KO143, as expected. Osimertinib also had an inhibitory effect on pump activity at high concentrations. However, the quantification of the data showed that osimertinib concentration required to be increased by 13-fold to achieve the same degree of ABCG2 inhibition as erlotinib

(Figure 3.54). Thus, erlotinib was a more potent inhibitor of ABCG2 efflux pump than osimertinib in SNU5 cells. This finding explained why the combination of SN38 and osimertinib failed to induce a strong synergy compared to the combination including erlotinib.

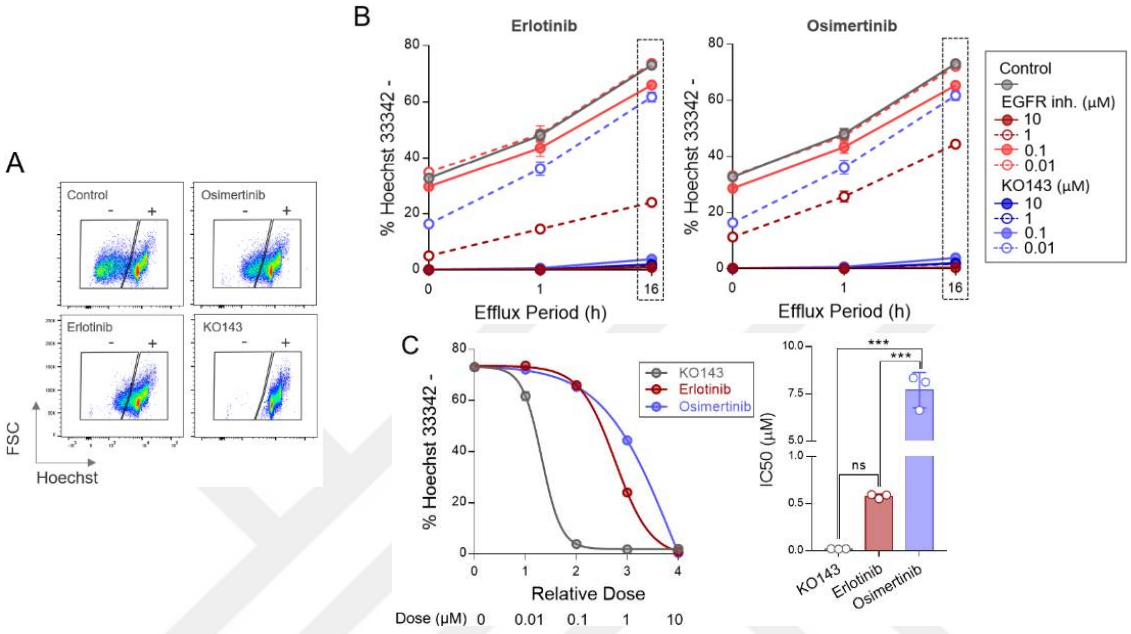

Figure 3.54: Results of Hoechst-33342 assay. A. Representative flow cytometry plots. B. Quantification of Hoechst-33342-negative population size at three different time points in the presence or absence of specified inhibitors. Dashed boxes indicate endpoints. C. Evaluation of Hoechst-33342 negativity at the endpoint with the corresponding concentration of each inhibitor. The bar plot at the right shows the IC_{50} of each sigmoidal curve. Statistical analysis was performed using Tukey's multiple comparison test. ****p*-value<0.001, ns: non-significant.

We investigated the relationship between the degree of synergy and ABCG2 expression level in six different gastric cancer cell lines in which the combination was previously tested. The ABCG2 expression level in these cell lines was quantified using qRT-PCR (Figure 3.55A). We observed that the degree of synergy was positively correlated with the ABCG2 expression level for five of these cell lines. Interestingly, although SNU16 cells exhibited the highest expression of ABCG2 compared to others, the strongest synergistic effect was not observed in these cells (Figure 3.55B). This finding suggested that the expression level of

ABCG2 could potentially serve as one of the biomarkers for predicting sensitivity to the combination treatment. However, the mutational profile of other genes is also a critical determinant of the overall drug response.

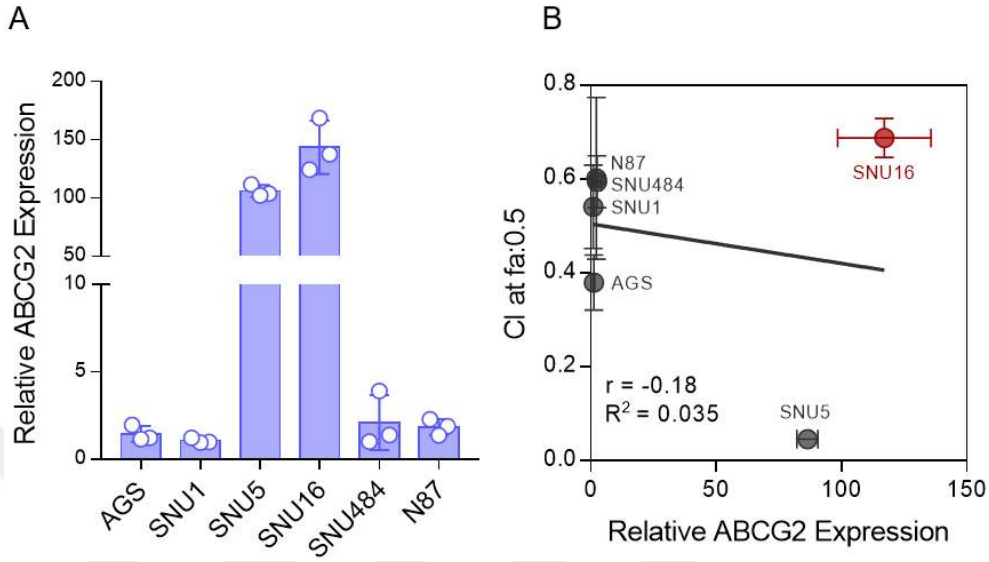

Figure 3.55: ABCG2 expression and its relation to synergy. A. Relative ABCG2 expression in six gastric cancer cell lines. B. Correlation between CI at fa:0.5 values and relative ABCG2 expression.

4. DISCUSSION

Gastric cancer is the fifth most malignant cancer type and the fourth-leading cause of cancer-associated deaths worldwide[1]. Combination chemotherapy is the main therapeutic strategy for the treatment of gastric cancer patients with resectable or metastatic tumors. Most of the clinically approved combination therapies for gastric cancer include conventional chemotherapeutics such as platinum-derived agents and fluoropyrimidines[34]. Despite the advances in identifying gastric tumor biomarkers, the targeted therapies approved for the treatment of gastric cancer patients are limited to trastuzumab[39], pembrolizumab[40], nivolumab[41], and ramucirumab[42].

The underlying principle of combination therapy is the administration of anti-cancer agents from different groups with non-overlapping toxicities to increase anti-tumor efficacy and decrease toxicity to healthy tissues. Since conventional therapeutics show a high risk of non-selective toxicities in patients, incorporating small molecule inhibitors in combination regimens has allowed the administration of conventional chemotherapeutics at lower doses while preserving therapeutic efficiency. Thus, the combination molecular-targeted agents and conventional chemotherapeutics has become an attractive approach to cancer therapy.

Many experimental and theoretical studies have been conducted to define pharmacological interactions in drug combinations, as it provides information about the treatment efficacy[81]. Pharmacological interactions in combination therapies encompass three main phenomena: synergy, antagonism, and additivity[81]. Synergy and antagonism are defined as an effect greater or lesser than the additivity, respectively[81]. In the concept of cancer therapy, it is crucial to achieve synergy in drug combinations, as it is a prerequisite for developing efficacious combination chemotherapies that are non-toxic to healthy tissues.

In this thesis study, we aimed to identify a novel combination chemotherapy that elicits synergistic interaction for gastric cancer treatment and define its mechanisms of action. We evaluated the dual combination of small molecule

inhibitors that target EGFR, mTOR, and c-MET and five different conventional chemotherapeutics widely used in clinics for cancer therapy. Although EGFR, mTOR, and c-MET are known to involve in gastric cancer tumorigenesis and progression, the incorporation of small molecule inhibitors targeting these proteins failed to improve therapeutic response, which was the main reason for selecting these molecular-targeted agents.

In the first step, we identified the pharmacological interactions in 15 different dual combinations applied to four gastric cancer cell lines using the combination index theorem developed by Chou and Talalay[101]. The combination index theorem is a dose-effect-based approach that quantitatively measures pharmacological interactions in combination treatments[81]. By this theorem, additivity is described by the CI equal to 1[101]. CI>1 and CI<1 indicate antagonistic and synergistic effects, respectively[101]. To reliably calculate CI values, we tested at least seven serially diluted concentrations of each component for all CI calculations performed using the Compusyn program. In addition, we applied molecular-targeted agents and conventional chemotherapeutics at the constant ratio since this program simulates CI-fa curves using observed data and provides CI values for a range of response levels when drugs are combined constantly. This allowed us to calculate CI values at a given response rate without testing the data point experimentally.

We initially performed drug pair screening by examining the drug response via MTT assay and identified drug combinations that elicited strong antagonistic and synergistic effects. We selected three antagonistic drug pairs to test whether the sequential application schedule can transform antagonism into synergy. Ten different sequential application schedules comprised of five time points (1h, 4h, 8h, 24h and 48h) and two different orders were employed to investigate this hypothesis. According to RV measurement by MTT assay, the most promising drug pair was the combination of 5-FU and everolimus that achieved synergy through the sequential application schedule in which 5-FU was applied 48h prior to everolimus.

RV metric measured by MTT is agnostic to the type of cellular processes responsible for the enhanced drug response that might result from partial or complete growth inhibition, cell death, or both. However, previous studies demonstrated that cancer cells whose growth is inhibited by treatment might continue to participate in disease progression upon the cessation of the therapy sessions[187]. It was also shown that chemotherapies inhibiting the proliferation of cancer cells might lead to the emergence of tumor subclones resistant to therapy[188]. Therefore, it is crucial to quantify cell death rate and kinetics rather than relative cell viability, which improves the evaluation of drug response. Following this information, we performed FLICK assay that effectively distinguishes cell death from growth inhibition to test F48Ev schedule showing synergy based on MTT assay. FLICK enables the measurement of FV, its inverse LF, GR, and RV metrics. Briefly, FV, or LF, provides direct insight into the degree of drug-induced cell death, and GR reveals the growth rate alterations in the presence and absence of the drug. FLICK results revealed that the degree of cell death in F48Ev schedule failed to differ from the simultaneous application of these agents in AGS cells. It was observed that the decrease in population size was due to partial growth inhibition, but not cell death. The measurement of cell death kinetics over time demonstrated that the death rate was not enhanced by either simultaneous or time-staggered applications.

Initial drug pair screening revealed the simultaneous application of SN38 and erlotinib elicited the strongest synergistic effect in all cell models, especially in SNU5 cells. SNU5 cells were obtained from a patient who received chemotherapy including 5-FU, doxorubicin and mitomycin-C[165]. Dose-response analysis of single-agent treatments showed that SNU5 was the most chemoresistant cell line against doxorubicin, 5-FU, paclitaxel, and SN38 compared to others. In addition to SN38, the dual combination of another TOP1 poison, topotecan, and TOP2 poisons, doxorubicin and epirubicin, induced the strong synergy. Moreover, according to MTT results, the dual combination of erlotinib with TOP1 and TOP2 poisons significantly enhanced the drug response in SNU5 cells compared to CF and ECF combinations, clinically approved

standard treatment regimens for gastric cancer therapy. Although the efficiency of combination therapies differs between *in vitro* studies and clinical applications, these results suggested that the combination of SN38 and erlotinib might be a promising treatment regimen for gastric cancer therapy.

We performed a FLICK assay to understand whether the synergy elicited by SN38 and erlotinib combination resulted from enhanced cell death or growth inhibition, or both, compared to single agents. FV and RV measurements uncovered that the combination increased drug-induced cell death and decreased population size, respectively. GR calculation indicated that combination increased the cell death at all concentrations compared to single agents, except for the lowest concentration that induced the growth arrest. It also showed that while SN38 triggered both growth inhibition and cell death in a dose-dependent manner, erlotinib treatment caused growth arrest without cell death at all concentrations. LF analysis performed by monitoring cell death kinetics over time showed that the combination resulted in earlier death onset time and increased cell death rate compared to single treatments. Therefore, we demonstrated that synergy in SN38 and erlotinib combination was consistent across the different assays and dependent on enhanced cell death and improved death kinetics. In this thesis study, we focused on understanding the combination mechanisms of action and identifying new molecular targets in gastric cancer.

We were intrigued by the molecular mechanisms underlying the synergy in combination. First, the changes in cell cycle progression were assessed under SN38 and combination at relatively low and high concentrations at different time points (4h, 12h, and 24h). While SN38 at low concentration did not affect the cell cycle progression, its high concentration led to S-phase arrest, which was also observed under combination at low concentration. Combination at high concentration induced strong cell cycle arrest at G1-phase. At these concentrations, it was unclear whether the presence of erlotinib only further enhanced the cellular response to SN38 or their combination resulted in enhanced growth arrest/cell death by activating entirely different intracellular signaling pathways.

Second, as SN38 is a DNA-damaging agent, we investigated the accumulation of DNA damage under the same conditions by assessing the phospho-H2AX level. The quantification of DNA damage level normalized to DNA content showed that SN38 at the high concentration and the combination at the low concentration induced DNA damage at 24h. On the other hand, combination at high concentration led to the accumulation of DNA damage significantly higher than other experiment groups, even at 4 hours.

Next, we decided to identify the type of cell death under SN38 and combination using five different cell death inhibitors, as it was previously shown that erlotinib only caused growth inhibition in SNU5 cells. According to the analysis of LF kinetics over time in the presence of death inhibitors, we found that SN38 and combination activated the intrinsic apoptosis since the inhibition of this pathway significantly delayed death onset time and decreased the death rate induced by these treatments.

As the last of phenotypical analyses, we investigated the degree of apoptotic cell death under SN38 and combination by assessing the level of cleaved-caspase3 and cleaved-PARP. Apoptosis was enhanced at 24h in response to SN38 at high concentration and the combination at low concentration. Combination at the high concentration strongly activated apoptotic cell death even at 12h. Along with all these results, we concluded that DNA damage-induced apoptosis was responsible for the cellular response to SN38 and combination, heavily dependent on the drug exposure period and the concentration applied. Although the high concentration of SN38 and the combination contained the same amount of SN38, the presence of erlotinib significantly altered the cellular response to the combination compared to SN38 alone. However, erlotinib mechanisms of action in combination remained elusive.

We generated $SNU^{EGFR\text{-}KO}$ single-cell clones to describe erlotinib mechanisms of action in combination and to investigate whether synergy in combination was linked to the inhibition of EGFR signaling by erlotinib. We analyzed drug response to the combination and single agents in $SNU^{EGFR\text{-}KO}$

compared to parental cells using FLICK. Surprisingly, the response of $SNU^{EGFR\text{-}KO}$ cells to SN38 remained unchanged in the absence of EGFR, which indicated that the genetic ablation of EGFR did not recapitulate its pharmacological inhibition by erlotinib. Therefore, we concluded that synergy in combination might be attributed to the off-target effects of erlotinib.

In line with optimization experiments, we performed a genome-scale CRISPR screening coupled with annexin-V bead sorting to elucidate the differences in cell death mechanisms induced by the equipotent concentrations of SN38 alone and the combination treatment. Our phenotypic response analyses demonstrated that these treatments, at the equipotent concentrations, elicited similar mechanisms as evidenced by the evaluation of well-known DNA damage and apoptosis markers. However, it is crucial to reveal whether the activation of these molecules, therefore, cell death is regulated by different intracellular signaling pathways under SN38 alone and the combination or not.

We performed GSEA analysis to uncover the gene sets that were significantly up- or downregulated in dead cells compared to live cells under both treatments. We realized that while three of the ten most enriched gene sets for SN38-only were associated with the S phase of the cell cycle, five of the top ten gene sets for combination were linked to the G2/M phase. Since our previous results showed that SN38-only and combination treatments caused cell cycle arrest at the S phase at concentrations used in the screen, we wondered why cells treated with combination were more sensitive to the ablation of genes regulating the G2/M phase. This might indicate that although the cell cycle profile is similar under both treatments at given concentrations, the cell death mechanism, orchestrated through cell cycle arrest, may differ between these treatments. This hypothesis established the basis for the selection of the first candidate gene list. To identify the genes, we used dead *vs* live cell comparisons for both treatment conditions to reveal the differences between death mechanisms induced by these treatments.

We employed the FLICK assay to validate the knockout effects of the first candidate gene list. However, since the CRISPR screen and FLICK assay were

performed under different experimental conditions, including the assay length, drug concentration, and the number of drug applications during the assay, these factors caused discrepancies between both experiments. Therefore, we decided to assess annexin-V positivity in knockout bulk populations under equipotent concentrations of SN38 and combination as in the screen to obtain consistent results. The findings of these evaluations indicated that, except for KEAP1 knockout cells, all populations knocked out for candidate genes failed to confirm the screening results. The knockout of genes, which were found to have different impacts on the cell death rate under SN38 and combination treatments, did not reveal any significant differences in the death rate between the two treatments. Moreover, the degree of cell death in these populations was similar to that of control cells. This could be attributed to the depletion of cells expressing sgRNA in populations with certain candidate genes knocked out. These results pinpointed the requirement for another candidate list involving more significantly enriched or depleted genes.

We listed second candidate genes using dead *vs* live cell comparisons considering enrichment/depletion levels in untreated cells compared to T0 input control. After generating the knockout bulk population for each candidate, we performed validation experiments using FLICK and competition assays under screen conditions. It is worth noting that intermittent treatments were not applied in the FLICK since it might cause significant variation in experiment results due to the nature of the assay. Both FLICK and competition assays showed that the knockout of genes that increased cell death or survival under both treatments confirmed the screen results. Moreover, the drug response of cells knockout for ARID1B and SLFN11 was still consistent when we exposed these knockout populations to serially diluted concentrations of SN38 and combination. The enhanced sensitivity of ARID1B knockout population and increased resistance of SLFN11 knockout population to both treatments were supported by the observed alterations in the potency of treatments.

Our literature review revealed that SNU5 cells harbor mutant ARID1A[189], an SWI/SNF chromatin remodeling complex member, participating in DNA damage response and functioning as a tumor suppressor[190]. Previous studies demonstrated that ATR and PARP inhibitors had enhanced the therapeutic response in ARID1A-deficient tumors by exploiting synthetic lethality[190]. Here, we suggest ARID1B inhibition in the presence of TOP1 poisons might be a therapeutic option for ARID1A-mutant gastric cancer tumors. On the other hand, SLFN11, a DNA/RNA helicase, leads to cell cycle arrest at S-phase, followed by cell death upon DNA damage[191]. Recent studies showed the high expression of SLFN11 is associated with sensitivity to platinum-derived agents in gastric cancer treatment[191]. Our findings propose that increased SLFN11 expression might also be a prospective biomarker for sensitivity to TOP1 poisons in gastric cancer therapy.

Gene knockouts that affected cell death or survival differentially under SN38 and combination failed to validate the screen data. We confirmed the screen results only for the genes whose knockouts resulted in enhanced cell death or survival under both treatments. This indicated that SN38 and combination might exhibit the same mechanisms of action. However, investigating chemo-genetic interactions for only a few genes might not suffice to consolidate this hypothesis.

We employed an RNAi-based signature assay that provides both statistical and biological generalization for anti-cancer agents to test whether SN38 and combination have the same mechanisms of action. The results showed that SN38 and combination significantly belonged to the TOP1 poisons category in the reference set. Thus, this analysis revealed that the combination exhibited the same mechanism of action as SN38 based on the biological and statistical classifications.

Functional genomics approaches, including perturbation screen and signature assay, failed to provide an insight into the erlotinib mechanisms of action in combination. Therefore, we decided to analyze drug response to the dual combination of SN38 and different EGFR inhibitors along with erlotinib in $SNU^{EGFR\text{-}KO}$ compared to parental cells. We observed similar drug responses in

$SNU^{EGFR\text{-}KO}$ cell models compared to the parental cells. These results demonstrated that the synergy observed in these combinations, with the exception of the SN38 and osimertinib combination, was not reliant on the inhibition of EGFR signaling. Alterations in ERK activity, a critical downstream target of the EGFR signaling pathway, were also evaluated under these EGFR inhibitors in a time-dependent manner. It showed that the degree and kinetics of ERK phosphorylation, indirectly the EGFR signaling pathway, was insensitive to the treatment with EGFR inhibitors, except for osimertinib in SNU5 cells. The results of these experiments were complementary to each other and demonstrated that synergy in the combination of SN38 and erlotinib was associated with the off-target effect of erlotinib.

Studies in the literature pointed out that other RTKs might be the off-targets of EGFR inhibitors[192]. However, this possibility was eliminated due to the unchanged ERK phosphorylation level, commonly regulated by RTK signalling pathways. Other off-targets proposed in the literature are specific efflux pumps belonging to the ABC transporter superfamily[183,184]. We inspected screen results based on this information to understand whether the knockout of any efflux pump altered the cell death/survival rate under SN38 and combinations treatments. We realized that ABCG2 knockout enhanced the cell death rate under both treatments in the screen. We also investigated the basal expression level of the ABCG2 efflux pump in different gastric cancer cell lines using a publicly available data set, which revealed that SNU5 is the cell line with the highest expression level of ABCG2 compared to the others. These results aligned with the hypothesis suggesting that synergy elicited by the combination of SN38 and erlotinib might depend on the ABCG2 inhibition by erlotinib.

We first analyzed the drug response to the dual combination of SN38 and three different ABCG2-specific inhibitors using the FLICK assay. These combinations showed a strong synergistic effect compatible with the combination of SN38 and erlotinib. Moreover, we evaluated the combination of SN38 and ABCB1 inhibitor, since ABCB1 is one of the efflux pumps highly upregulated in

chemoresistant cell lines. This combination failed to achieve a similar degree of synergy, indicating that synergy was highly specific to ABCG2 inhibition.

Next, we analyzed LF metric and annexin-V positivity in ABCG2 knockout bulk populations under SN38 and combination treatments. These results demonstrated that the knockout of ABCG2 enhanced the cell death rate under both treatments, confirming screen results. In addition, our competition assay results showed that the survival ability of ABCG2 knockout cells treated with SN38 and combination significantly declined compared to control cells. Moreover, we analyzed the drug response to SN38 and the combination in ABCG2 knockout and control cells using the FV metric. This analysis revealed that SN38 applied to ABCG2 knockout cells achieved the same drug response induced by combination in control cells. Therefore, the absence of ABCG2 expression completely recapitulated the erlotinib action in variety.

To inspect the mechanistic effect of erlotinib on ABCG2 activity, we performed a Hoechst-33342 assay in SNU5 cells. By analyzing Hoechst-33342 efflux kinetics, we observed that erlotinib strongly interfered with the pump activity of ABCG2. This result further demonstrated a synergistic effect in the combination of SN38 and erlotinib resulting from ABCG2 inhibition by erlotinib.

We investigated whether the expression level of ABCG2 is a predictive marker for the degree of synergy. For this purpose, we compared ABCG2 expression levels with CI values for six gastric cancer cell lines in which the combination was previously tested. A positive correlation between the expression level and synergy was observed for five of these cell models. However, although SNU16 cells exhibited the highest expression of ABCG2 compared to others, the strongest synergistic effect was not observed in these cells. This data indicated that the degree of synergy is not solely dependent on the ABCG2 expression level, which is likely to be associated with each cell line's repertoire of mutational signatures. For instance, the publicly available data set assessment revealed that SLFN11 expression level is strongly decreased in SNU16 cells compared to SNU5 cells. As supported by our perturbation screen and previous studies, decreased

SLFN11 expression is responsible for developing drug resistance against DNA-damaging agents. This might be the one possible explanation for the low degree of synergy in SNU16 cells despite the high ABCG2 expression. Therefore, we concluded while ABCG2 expression level showed promise as a predictive biomarker, a comprehensive understanding of the mutational landscape of other genes is necessary for a more accurate assessment of treatment response to the combination of SN38 and erlotinib.

In summary, we have successfully identified a novel combination chemotherapy that involved SN38 and erlotinib, and demonstrated strong synergy in the treatment of gastric cancer. We have unravelled the molecular mechanism underlying this synergy through comprehensive functional genomics approaches including a genome-wide perturbation screen and an RNAi-based signature assay. Our investigation, combined with existing literature, has identified the ABCG2 efflux pump as a specific target of erlotinib applied in combination therapy. This study marks the first discovery of ABCG2 as an off-target of erlotinib and a potential mechanism of drug resistance against TOP1 poison in gastric cancer, employing powerful functional genomics methodologies. ABCG2 has previously been implicated in the development of acquired drug resistance to cisplatin and fluoropyrimidines in the context of gastric cancer therapy[193,194]. Other resistance mechanisms, such as alterations in DNA damage repair or drug inactivation, can potentially be overcome by challenging cancer cells with chemotherapeutics that exhibit different mechanisms of action. However, the resistance mechanism relying on enhanced expression or activity of efflux pumps might decrease the therapeutic efficiency of a broad spectrum of chemotherapeutics since it directly affects intracellular drug accumulation. Our findings demonstrate that combining SN38 with erlotinib, which acts as an ABCG2 inhibitor, can achieve robust synergy by facilitating pharmacodynamic actions. Therefore, based on the insights provided by this thesis study, we propose that ABCG2 inhibition by erlotinib in the presence of TOP1 poison represents a promising therapeutic strategy for the treatment of both naïve and chemoresistant gastric cancer tumors.

5. APPENDIX

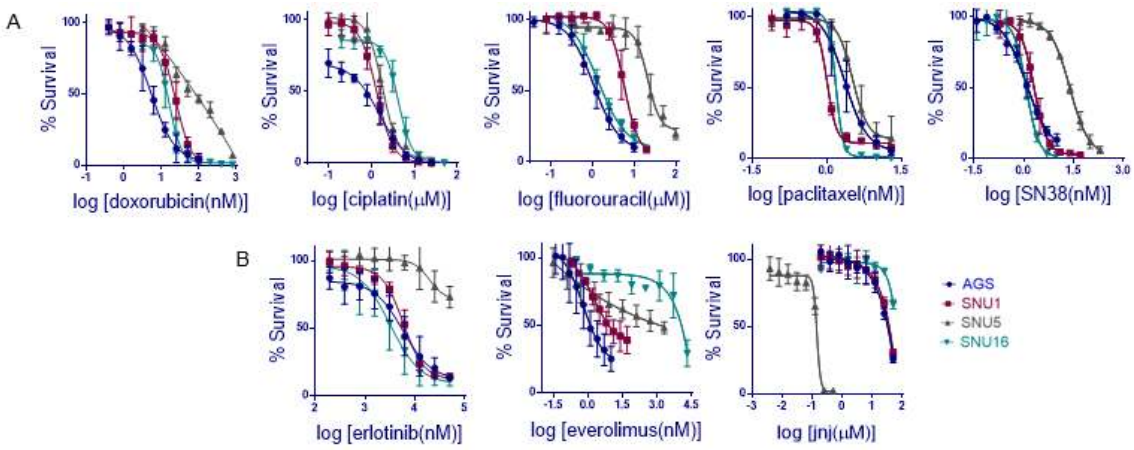

Figure 5.1: Individual dose-response curves of molecular-targeted agents and conventional chemotherapeutics in gastric cancer cell lines.

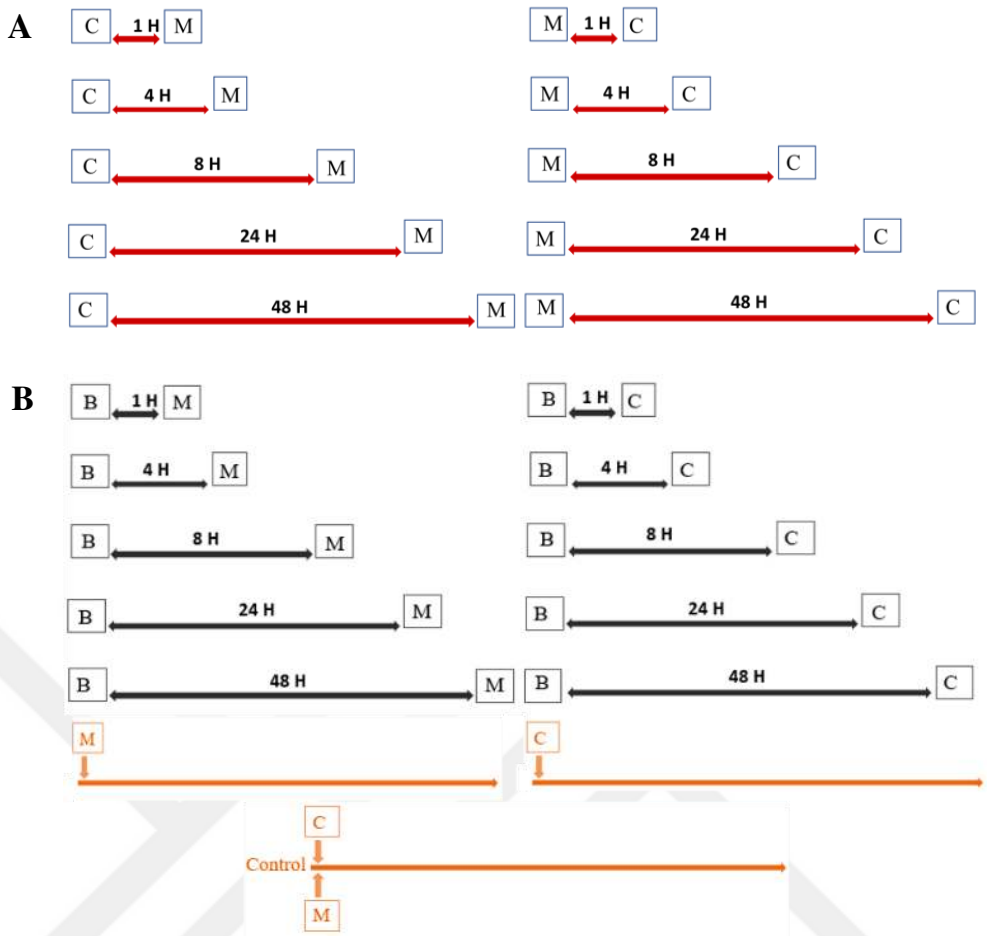

Figure 5.2: Sequential application schedules. **A.** Experiment groups. **B.** Control groups. MTT was performed 5 days after the first treatment, and therefore experiment groups shown in A were exposed to the second agent less than 5 days. For this reason, a time-matched control for each experiment group was generated, indicated by dark grey color in B. C: Conventional chemotherapeutic. M: Molecular-targeted agent. B: Blank.

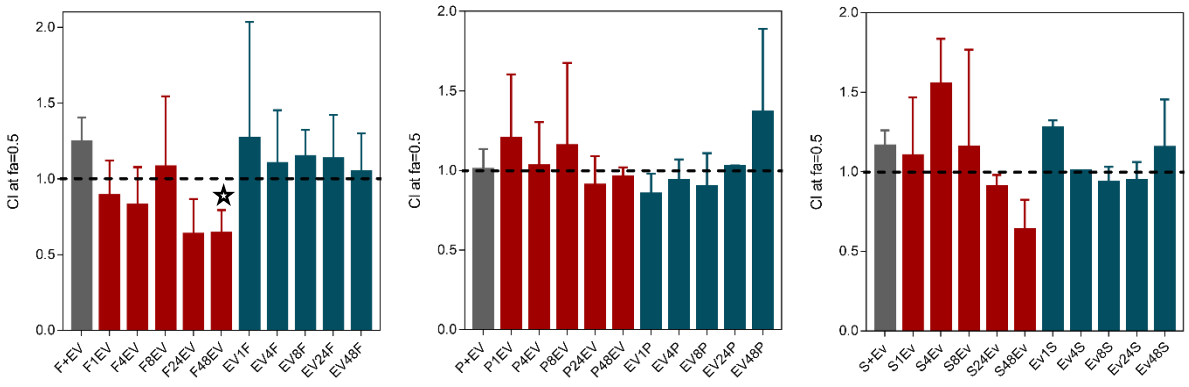

Figure 5.3: Time-staggered application of antagonistic drug pairs using MTT. CI at fa:0.5 graphs for each the sequential application schedule that combines everolimus either with 5-FU, paclitaxel or SN38. F48Ev schedule indicated on the left graph achieved to transform antagonism observed in the concomitant application (F+Ev) into synergism based on MTT results. F: 5-FU. P: Paclitaxel. S: SN38. Ev: Everolimus.

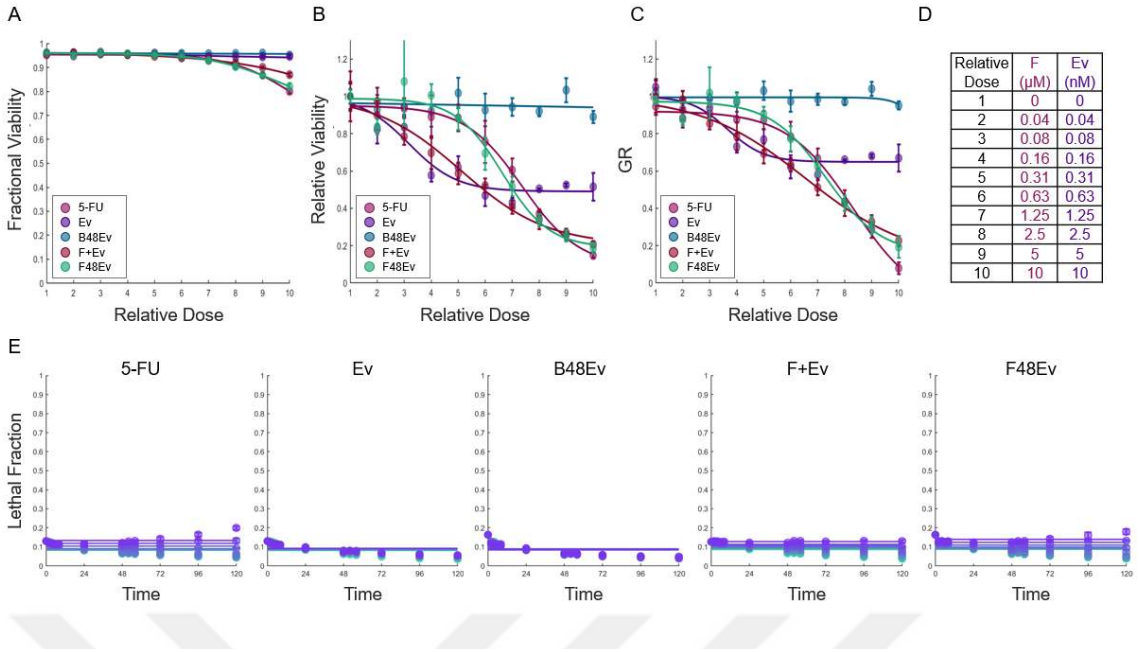

Relative Dose	F (μM)	Ev (nM)
1	0	0
2	0.04	0.04
3	0.08	0.08
4	0.16	0.16
5	0.31	0.31
6	0.63	0.63
7	1.25	1.25
8	2.5	2.5
9	5	5
10	10	10

Figure 5.4: Results from FLICK assay for F48Ev schedule. A. FV did not significantly differ between F+Ev and F48Ev schedules B. According to RV measurements, the population size decreased in both F+Ev and F48Ev ; however, F+Ev induced a more efficacious response than F48Ev. C. GR quantification showed that the change in population size was due to the partial inhibition of cell growth, not cell death. D. 5-FU (F) and everolimus (Ev) concentrations at corresponding relative doses. E. The measurement of LF metric demonstrated that the death rate was not increased by either different treatments or different doses. B: Blank.

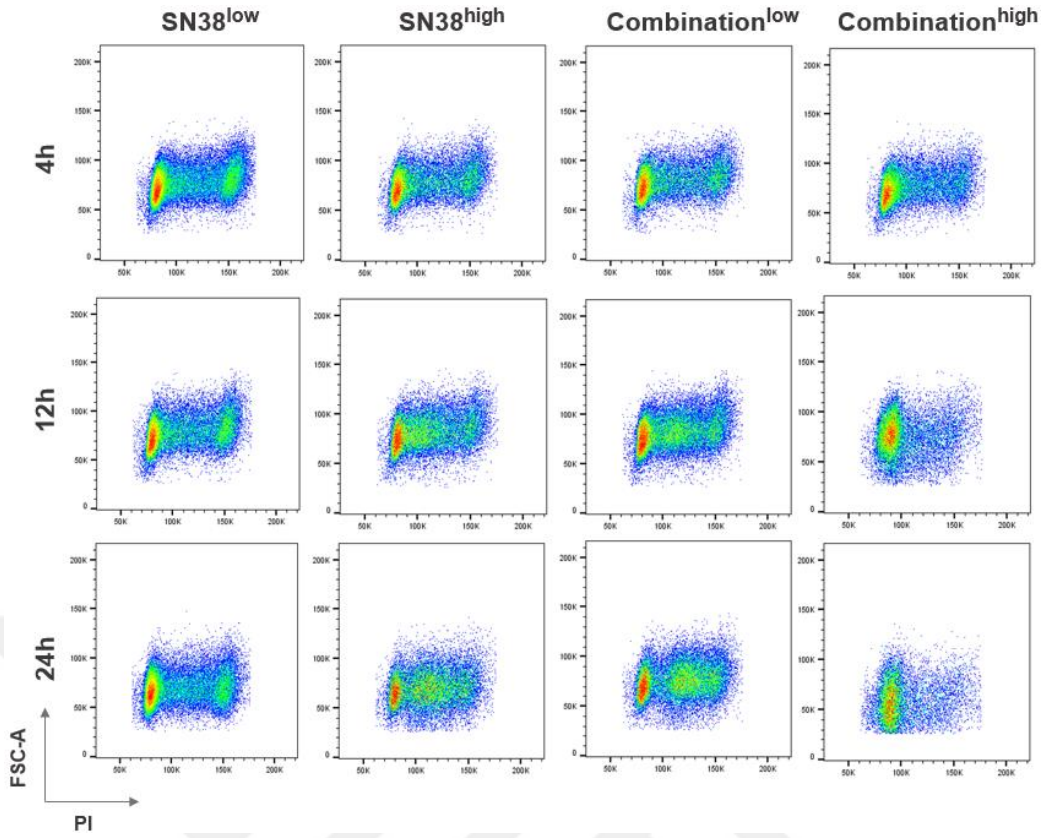

Figure 5.5: Representative flow cytometry plots of cell cycle analysis. PI: propidium iodide.

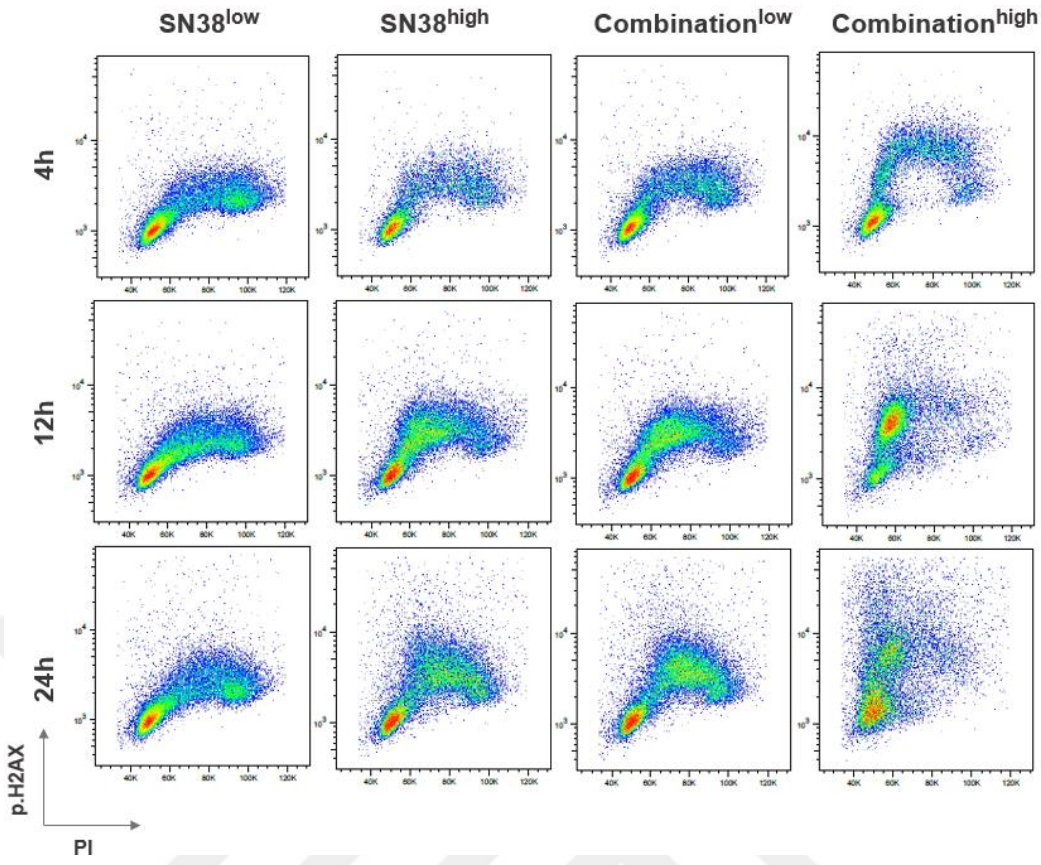

Figure 5.6: Representative flow cytometry plots of DNA damage profiling coupled with cell cycle analysis. p.H2AX: phospho-H2AX. PI: propidium iodide.

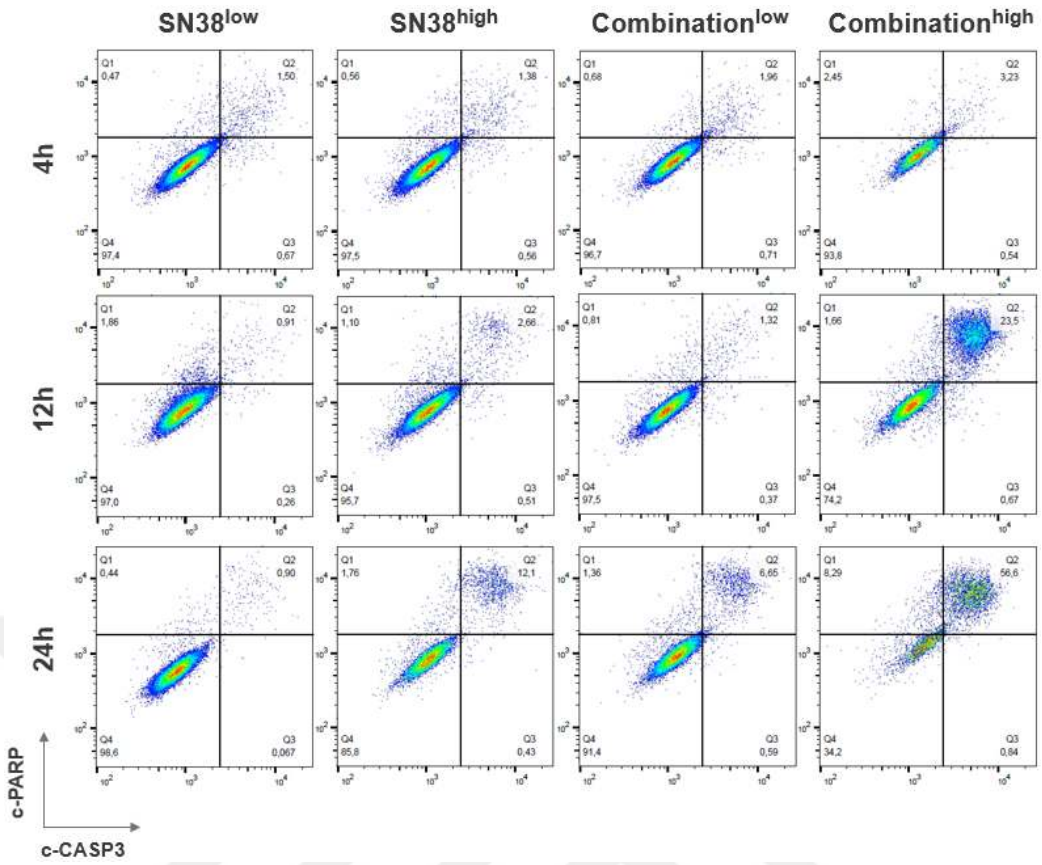

Figure 5.7: Representative flow cytometry plots of apoptotic cell death analysis. c-PARP: cleaved-PARP. c-CASP3: cleaved-CASPASE3.

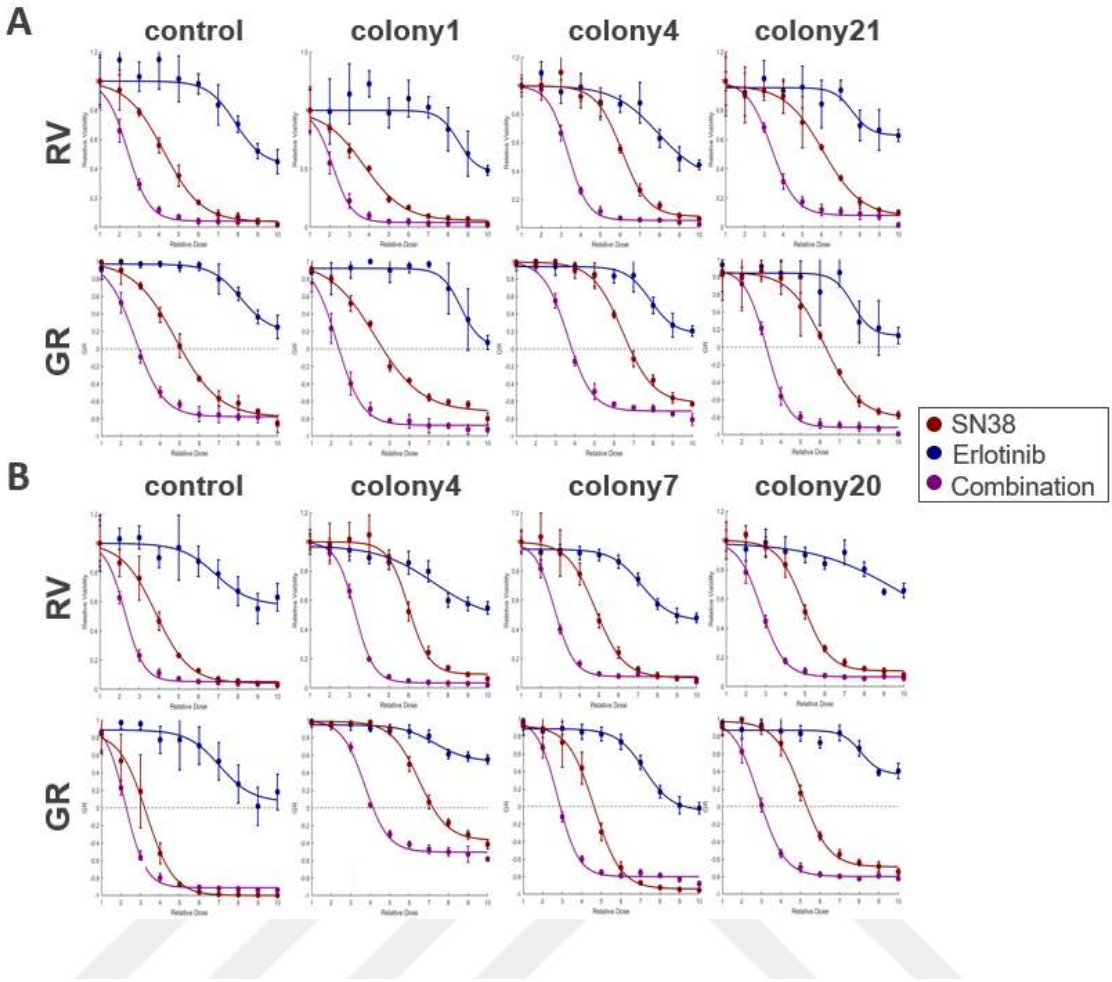

Figure 5.8: RV and GR analysis in SNU$^{EGFR-KO}$ single-cell clones. A. The first batch of SNU$^{EGFR-KO}$ single-cell clones. B. The second batch of SNU$^{EGFR-KO}$ single-cell clones. x-axis: relative dose.

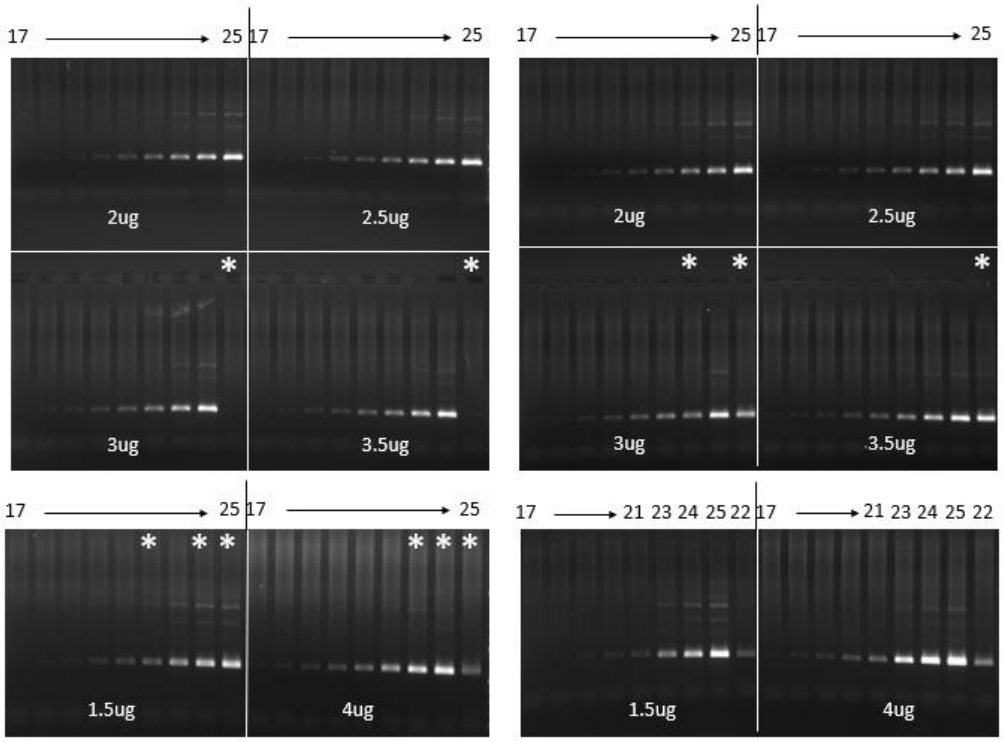

Figure 5.9: Optimization of PCR1 reaction. Agarose gel images show PCR1 products produced by amplifying indicated DNA masses with cycle numbers ranging from 17 to 25.

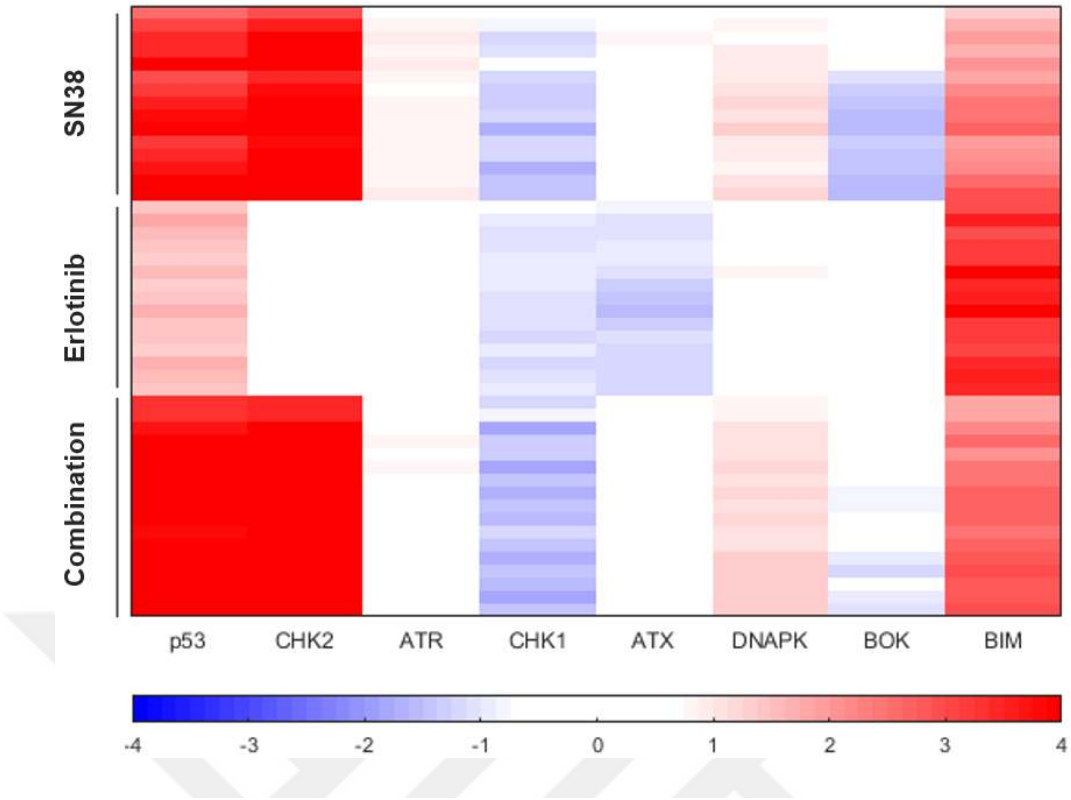

Figure 5.10: Heatmap showing the signatures of all replicates of each treatment condition.

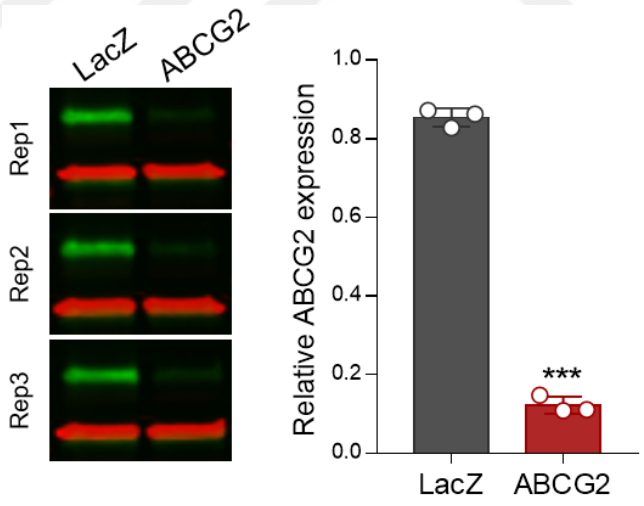

Figure 5.11: ABCG2 expression in ABCG2 knockout bulk population. Immunoblots show the ABCG2 expression level in untargeted and ABCG2 knockout bulk populations. The data quantification is provided on the right. Welch's t-test was used for statistical testing. ***<0.001.Rep: replicate.

Gene Name	Sequence (5' → 3')
ABCG2_F	GCTGCAAGGAAAGATCCAAG
ABCG2_R	CTTGGATCTTTCCTTGCAGC
ANAPC4_F	AAAGCAATGAGATCCCGCTT
ANAPC4_R	AAGCGGGATCTCATTGCTTT
ARID1B_F	TCATCTCTCCAGCATCCCGG
ARID1B_R	CCGGGATGCTGGAGAGATGA
AURKB_F	AGGCCACCATACCTCAGGGA
AURKB_R	TCCCTGAGGTATGGTGGCCT
CDC45_F	TGACCACGTGCAATATACGC
CDC45_R	GCGTATATTGCACGTGGTCA
CLSPN_F	ATAGTGCCATGGCATTTCCG
CLSPN_R	CGGAAATGCCATGGCACTAT
COPG1_F	AATGCAAGACATCTCCTTGA
COPG1_R	TCAAGGAGATGTCTTGCATT
CYP2A6_F	CCCAATGAAGAGGTTCAACG
CYP2A6_R	CGTTGAACCTCTTCATTGGG
DDX39B_F	TCTTTGTGAAGTCTGTGCAG
DDX39B_R	CTGCACAGACTTCACAAAGA
ECD_F	GCTGTGAATAGGCGCATCAG
ECD_R	CTGATGCGCCTATTCACAGC
FABP5_F	GACTTAACATTCTACAGGAG
FABP5_R	CTCCTGTAGAATGTTAAGTC
GINS1_F	TGAAGGTTTGGACATTACAC
GINS1_R	GTGTAATGTCCAAACCTTCA
HIST1H2BI_F	GTAACTAGTTTACTTGGAGC
HIST1H2BI_R	GCTCCAAGTAAACTAGTTAC

Gene Name	Sequence (5' → 3')
HIST1H3D_F	CAGTTTGCGAATCAGCAGCT
HIST1H3D_R	AGCTGCTGATTCGCAAACTG
KEAP1_F	GAGGACACACTTCTCGCCCA
KEAP1_R	TGGGCGAGAAGTGTGTCCTC
LacZ_F	TGCGAATACGCCCACGCGAT
LacZ_R	ATCGCGTGGGCGTATTCGCA
MAD1L1_F	GTTGTTCAAAGATCTCAGGG
MAD1L1_R	CCCTGAGATCTTTGAACAAC
MAD2L1_F	AATGTGGTGGAACAACTGAA
MAD2L1_R	TTCAGTTGTTCCACCACATT
NANOG_F	AGCCTACCTGTTTGTAGCTG
NANOG_R	CAGCTACAAACAGGTAGGCT
RNF168_F	GAGTCCACGACGATACCCGG
RNF168_R	CCGGGTATCGTCGTGGACTC
SLFN11_F	GTATATCGCAAATATCCTGG
SLFN11_R	CCAGGATATTTGCGATATAC
STK3_F	TGAGCTGGATTCCCACACCA
STK3_R	TGGTGTGGGAATCCAGCTCA
TET3_F	GAGGCTGGGAACAACAGCAG
TET3_R	CTGCTGTTGTTCCCAGCCTC
ZC3H18_F	AAGAGGCATCACGCACCCAA
ZC3H18_R	TTGGGTGCGTGATGCCTCTT
ZNF479_F	AATTCCGCTGAGCACAATCC
ZNF479_R	GGATTGTGCTCAGCGGAATT
ZNF547_F	TGGGTAGATAGACAGGGCTT
ZNF547_R	AAGCCCTGTCTATCTACCCA

Table 5.1: sgRNA sequences used in validation experiments.

shRNA	Target Sequence
p53	CCACTACAAGTACATGTGTAA
CHK2	CAGAAACACATAATCATTAAA
ATR	ACCCATGTTCTTGACATTGAA
CHK1	CAGGAATATTCTGATTGGAAA
ATX	CAGGATAGCAATAAAGATGAA
DNA-PK	CAGGCCTATACTTACAGTTAA
BOK	CTGGCCTCTGTGACTGCTCTA
BIM	TAGGAACAGAGAAATATGCAA

Table 5.2: shRNA sequences used in RNAi-based signature assay.

6. BIBLIOGRAPHY

1. Thrift, A. P., Wenker, T. N. & El-Serag, H. B. Global burden of gastric cancer: epidemiological trends, risk factors, screening and prevention. *Nat. Rev. Clin. Oncol.* 20, 338–349 (2023).
2. Morgan, E. *et al.* The current and future incidence and mortality of gastric cancer in 185 countries, 2020–40: A population-based modelling study. *eClinicalMedicine* 47, (2022).
3. Sung, H. *et al.* Global Cancer Statistics 2020: GLOBOCAN Estimates of Incidence and Mortality Worldwide for 36 Cancers in 185 Countries. *CA. Cancer J. Clin.* 71, (2021).
4. Fock, K. M. Review article: The epidemiology and prevention of gastric cancer. *Alimentary Pharmacology and Therapeutics* 40, (2014).
5. González, C. A. *et al.* Helicobacter pylori infection assessed by ELISA and by immunoblot and noncardia gastric cancer risk in a prospective study: The Eurgast-EPIC project. *Ann. Oncol.* 23, (2012).
6. Parsonnet, J. *et al.* Helicobacter pylori infection in intestinal- and diffuse-type gastric adenocarcinomas. *J. Natl. Cancer Inst.* 83, (1991).
7. Plummer, M., Franceschi, S., Er^ Ome Vignat, J., Forman, D. & De Martel, C. Global burden of gastric cancer attributable to Helicobacter pylori Helicobacter pylori in gastric cancer. *Int. J. Cancer* 136, (2015).
8. Karimi, P., Islami, F., Anandasabapathy, S., Freedman, N. D. & Kamangar, F. Gastric cancer: Descriptive epidemiology, risk factors, screening, and prevention. *Cancer Epidemiology Biomarkers and Prevention* 23, (2014).
9. Na, H. K. & Lee, J. Y. Molecular basis of alcohol-related gastric and colon cancer. *International Journal of Molecular Sciences* 18, (2017).
10. Jelski, W., Chrostek, L., Zalewski, B. & Szmitkowski, M. Alcohol dehydrogenase (ADH) isoenzymes and aldehyde dehydrogenase (ALDH) activity in the sera of patients with gastric cancer. *Dig. Dis. Sci.* 53, (2008).
11. D'Elia, L., Rossi, G., Ippolito, R., Cappuccio, F. P. & Strazzullo, P. Habitual salt intake and risk of gastric cancer: A meta-analysis of prospective studies. *Clin. Nutr.* 31, (2012).
12. Zhao, Z., Yin, Z. & Zhao, Q. Red and processed meat consumption and gastric cancer risk: A systematic review and meta-analysis. *Oncotarget* 8, (2017).
13. Kim, W., Kidambi, T., Lin, J. & Idos, G. Genetic Syndromes Associated with Gastric Cancer. *Gastrointestinal Endoscopy Clinics of North America* 32, (2022).
14. Berlth, F., Bollschweiler, E., Drebber, U., Hoelscher, A. H. & Moenig, S. Pathohistological classification systems in gastric cancer: Diagnostic relevance and prognostic value. *World J. Gastroenterol.* 20, 5679–5684 (2014).
15. Vauhkonen, M., Vauhkonen, H. & Sipponen, P. Pathology and molecular biology of gastric cancer. *Best Pract. Res. Clin. Gastroenterol.* 20, 651–674 (2006).
16. LAUREN, P. THE TWO HISTOLOGICAL MAIN TYPES OF GASTRIC CARCINOMA: DIFFUSE AND SO-CALLED INTESTINAL-TYPE CARCINOMA. AN ATTEMPT AT A HISTO-CLINICAL CLASSIFICATION. *Acta Pathol. Microbiol. Scand.* 64, (1965).
17. Leocata P, Ventura L, Giunta M, Guadagni S, Fortunato C, Discepoli S, V. T. Carcinoma gastrico: studio istopatologico di 705 casi [Gastric carcinoma: a histopathological study of 705 cases]. *Ann Ital Chir.* 69, 331–7 (1998).
18. Tang, C. T., Zeng, L., Yang, J., Zeng, C. & Chen, Y. Analysis of the Incidence and Survival of Gastric Cancer Based on the Lauren Classification: A Large Population-Based Study Using SEER. *Front. Oncol.* 10, (2020).
19. Perrot-Applanat, M. *et al.* Differential gene expression in growth factors, epithelial mesenchymal transition and chemotaxis in the diffuse type compared with the intestinal type of gastric cancer. *Oncol. Lett.* 18, (2019).
20. Machlowska, J. *et al.* State of the art for gastric signet ring cell carcinoma: From classification, prognosis, and genomic characteristics to specified treatments. *Cancer Management and Research* 11, (2019).
21. Oliveira, C. *et al.* Screening E-cadherin in gastric cancer families reveals germline mutations only in hereditary diffuse gastric cancer kindred. *Hum. Mutat.* 19, (2002).
22. Hansson, L. E., Lindgren, A. & Nyrén, O. Can endoscopic biopsy specimens be used for reliable Lauren classification of gastric cancer? *Scand. J. Gastroenterol.* 31, (1996).
23. Flucke, U. *et al.* Differences between biopsy- or specimen-related Laurén and World Health Organization classification in gastric cancer. *World J. Surg.* 26, (2002).
24. Bass, A. J. *et al.* Comprehensive molecular characterization of gastric adenocarcinoma. *Nature* 513, 202–209 (2014).

25. Macdonald, J. S. & Smalley, S. R. Chemoradiotherapy After Surgery Compared With Surgery Alone For Adenocarcinoma Of The Stomach Or Gastroesophageal Junction. *English J.* 345, 725–730 (2001).
26. Cunningham, D. & Allum, W. H. Perioperative Chemotherapy versus Surgery Alone for Resectable Gastroesophageal Cancer. *N. Engl. J. Med.* 355, 609–619 (2006).
27. Arai, H. & Nakajima, T. E. Recent developments of systemic chemotherapy for gastric cancer. *Cancers (Basel).* 12, 1–30 (2020).
28. Al-Batran, S. E. *et al.* Perioperative chemotherapy with fluorouracil plus leucovorin, oxaliplatin, and docetaxel versus fluorouracil or capecitabine plus cisplatin and epirubicin for locally advanced, resectable gastric or gastro-oesophageal junction adenocarcinoma (FLOT4): a randomised, phase 2/3 trial. *Lancet* 393, (2019).
29. Yang, Y. *et al.* Perioperative chemotherapy more of a benefit for overall survival than adjuvant chemotherapy for operable gastric cancer: An updated Meta-analysis. *Sci. Rep.* 5, (2015).
30. Noh, S. H. *et al.* Adjuvant capecitabine plus oxaliplatin for gastric cancer after D2 gastrectomy (CLASSIC): 5-year follow-up of an open-label, randomised phase 3 trial. *Lancet Oncol.* 15, 1389–1396 (2014).
31. Pasini, F., Fraccon, A. P. & De Manzoni, G. The role of chemotherapy in metastatic gastric cancer. *Anticancer Research* 31, (2011).
32. Ford, H. E. R. *et al.* Docetaxel versus active symptom control for refractory oesophagogastric adenocarcinoma (COUGAR-02): An open-label, phase 3 randomised controlled trial. *Lancet Oncol.* 15, (2014).
33. Thuss-Patience, P. C. *et al.* Survival advantage for irinotecan versus best supportive care as second-line chemotherapy in gastric cancer - A randomised phase III study of the Arbeitsgemeinschaft Internistische Onkologie (AIO). *Eur. J. Cancer* 47, (2011).
34. Lordick, F. *et al.* Gastric cancer: ESMO Clinical Practice Guideline for diagnosis, treatment and follow-up. *Ann. Oncol.* 33, (2022).
35. Alsina, M., Arrazubi, V., Diez, M. & Tabernero, J. Current developments in gastric cancer: from molecular profiling to treatment strategy. *Nat. Rev. Gastroenterol. Hepatol.* 20, 155–170 (2023).
36. Van Cutsem, E. *et al.* Phase III study of docetaxel and cisplatin plus fluorouracil compared with cisplatin and fluorouracil as first-line therapy for advanced gastric cancer: A report of the V25 study group. *J. Clin. Oncol.* 24, 4991–4997 (2006).
37. Shah, M. A. *et al.* Randomized multicenter phase II study of modified docetaxel, cisplatin, and fluorouracil (DCF) versus DCF plus growth factor support in patients with metastatic gastric adenocarcinoma: A study of the US gastric cancer consortium. *J. Clin. Oncol.* 33, (2015).
38. Wang, J. *et al.* Randomized multicenter phase III study of a modified docetaxel and cisplatin plus fluorouracil regimen compared with cisplatin and fluorouracil as first-line therapy for advanced or locally recurrent gastric cancer. *Gastric Cancer* 19, 234–244 (2016).
39. Bang, Y. J. *et al.* Trastuzumab in combination with chemotherapy versus chemotherapy alone for treatment of HER2-positive advanced gastric or gastro-oesophageal junction cancer (ToGA): A phase 3, open-label, randomised controlled trial. *Lancet* 376, 687–697 (2010).
40. Chung, H. C. *et al.* First-line pembrolizumab/placebo plus trastuzumab and chemotherapy in HER2-positive advanced gastric cancer: KEYNOTE-811. *Futur. Oncol.* 17, (2021).
41. Janjigian, Y. Y. *et al.* First-line nivolumab plus chemotherapy versus chemotherapy alone for advanced gastric, gastro-oesophageal junction, and oesophageal adenocarcinoma (CheckMate 649): a randomised, open-label, phase 3 trial. *Lancet* 398, (2021).
42. Wilke, H. *et al.* Ramucirumab plus paclitaxel versus placebo plus paclitaxel in patients with previously treated advanced gastric or gastro-oesophageal junction adenocarcinoma (RAINBOW): A double-blind, randomised phase 3 trial. *Lancet Oncol.* 15, 1224–1235 (2014).
43. Al-Batran, S.-E. *et al.* 1421MO Final results and subgroup analysis of the PETRARCA randomized phase II AIO trial: Perioperative trastuzumab and pertuzumab in combination with FLOT versus FLOT alone for HER2 positive resectable esophagogastric adenocarcinoma. *Ann. Oncol.* 31, (2020).
44. Shitara, K., Doi, T., Dvorkin, M., Mansoor, W. & Arkenau, Hendrik-Tobias Prokharau, Aliaksandr Alsina, M. et al. Trifluridine/tipiracil versus placebo in patients with heavily pretreated metastatic gastric cancer (TAGS): a randomised, double-blind, placebo-controlled, phase 3 trial. *The Lancet Oncology* 19, 1437–1448 (2018).
45. Alexandrov, L. B. *et al.* Signatures of mutational processes in human cancer. *Nature* 500, (2013).
46. Hanahan, D. Hallmarks of Cancer: New Dimensions. *Cancer Discovery* 12, (2022).
47. Fuchs, C. S. *et al.* Ramucirumab monotherapy for previously treated advanced gastric or gastro-oesophageal junction adenocarcinoma (REGARD): An international, randomised, multicentre,

placebo-controlled, phase 3 trial. *Lancet* 383, 31–39 (2014).
48. Salomon, D. S., Brandt, R., Ciardiello, F. & Normanno, N. Epidermal growth factor-related peptides and their receptors in human malignancies. *Crit. Rev. Oncol. Hematol.* 19, 183–232 (1995).
49. Wang, Y. K. *et al.* Assessment of ERBB2 and EGFR gene amplification and protein expression in gastric carcinoma by immunohistochemistry and fluorescence in situ hybridization. *Mol. Cytogenet.* 4, 2–7 (2011).
50. Weng, X. *et al.* Hypermethylated epidermal growth factor receptor (EGFR) promoter is associated with gastric cancer. *Sci. Rep.* 5, 1–10 (2015).
51. Nagatsuma, A. K. *et al.* Expression profiles of HER2, EGFR, MET and FGFR2 in a large cohort of patients with gastric adenocarcinoma. *Gastric Cancer* 18, 227–238 (2015).
52. Ema, A. *et al.* Identification of EGFR expression status association with metastatic lymph node density (ND) by expression microarray analysis of advanced gastric cancer. *Cancer Med.* 4, 90–100 (2015).
53. Zhen, Y., Guanghui, L. & Xiefu, Z. Knockdown of EGFR inhibits growth and invasion of gastric cancer cells. *Cancer Gene Ther.* 21, 491–497 (2014).
54. Hotz, B., Keilholz, U., Fusi, A., Buhr, H. J. & Hotz, H. G. In vitro and in vivo antitumor activity of cetuximab in human gastric cancer cell lines in relation to epidermal growth factor receptor (EGFR) expression and mutational phenotype. *Gastric Cancer* 15, (2012).
55. Matar, P. *et al.* Combined epidermal growth factor receptor targeting with the tyrosine kinase inhibitor Gefitinib (ZD1839) and the monoclonal antibody Cetuximab (IMC-C225): Superiority over single-agent receptor targeting. *Clin. Cancer Res.* 10, (2004).
56. Liu, X. *et al.* Cetuximab enhances the activities of irinotecan on gastric cancer cell lines through downregulating the EGFR pathway upregulated by irinotecan. *Cancer Chemother. Pharmacol.* 68, 871–878 (2011).
57. Luo, H.-Y., Wei, W. & Shi, Y.-X. Cetuximab enhances the effect of oxaliplatin on hypoxic gastric cancer cell lines. *Oncol. Rep.* 23, 1735–1745 (2010).
58. Park, J. K. *et al.* Synergistic interaction between gefitinib (Iressa, ZD1839) and paclitaxel against human gastric carcinoma cells. *Anticancer. Drugs* 15, 809–818 (2004).
59. Pinto, C. *et al.* Phase II study of cetuximab in combination with cisplatin and docetaxel in patients with untreated advanced gastric or gastro-oesophageal junction adenocarcinoma (DOCETUX study). *Br. J. Cancer* 101, 1261–1268 (2009).
60. Kim, C. *et al.* A prospective phase II study of cetuximab in combination with XELOX (capecitabine and oxaliplatin) in patients with metastatic and/or recurrent advanced gastric cancer. *Invest. New Drugs* 29, 366–373 (2011).
61. Lordick, F. *et al.* Capecitabine and cisplatin with or without cetuximab for patients with previously untreated advanced gastric cancer (EXPAND): A randomised, open-label phase 3 trial. *Lancet Oncol.* 14, 490–499 (2013).
62. Rojo, F. *et al.* Pharmacodynamic studies of gefitinib in tumor biopsy specimens from patients with advanced gastric carcinoma. *J. Clin. Oncol.* 24, 4309–4316 (2006).
63. Maron, S. B. *et al.* Targeted therapies for targeted populations: Anti-EGFR treatment for EGFR-amplified gastroesophageal adenocarcinoma. *Cancer Discov.* 8, (2018).
64. Laplante, M. & Sabatini, D. M. MTOR signaling in growth control and disease. *Cell* 149, 274–293 (2012).
65. Tapia, O. *et al.* The PI3K/AKT/mTOR pathway is activated in gastric cancer with potential prognostic and predictive significance. *Virchows Arch.* 465, 25–33 (2014).
66. Byeon, S. J., Han, N., Choi, J., Kim, M. A. & Kim, W. H. Prognostic implication of TSC1 and mTOR expression in gastric carcinoma. *J. Surg. Oncol.* 109, 812–817 (2014).
67. Lang, S. A. *et al.* Mammalian target of rapamycin is activated in human gastric cancer and serves as a target for therapy in an experimental model. *Int. J. Cancer* 120, 1803–1810 (2007).
68. Cejka, D. *et al.* Everolimus (RAD001) and anti-angiogenic cyclophosphamide show long-term control of gastric cancer growth in vivo. *Cancer Biol. Ther.* 7, 1377–1385 (2008).
69. Yoon, D. H. *et al.* Phase II study of everolimus with biomarker exploration in patients with advanced gastric cancer refractory to chemotherapy including fluoropyrimidine and platinum. *Br. J. Cancer* 106, 1039–1044 (2012).
70. Doi, T. *et al.* Multicenter phase II study of everolimus in patients with previously treated metastatic gastric cancer. *J. Clin. Oncol.* 28, 1904–1910 (2010).
71. Lee, J. *et al.* Phase II trial of capecitabine and everolimus (RAD001) combination in refractory gastric cancer patients. *Invest. New Drugs* 31, 1580–1586 (2013).
72. Shen, Y. C. *et al.* Phase ii multicentered study of low-dose everolimus plus cisplatin and weekly

24-hour infusion of high-dose 5-fluorouracil and leucovorin as first-line treatment for patients with advanced gastric cancer. *Oncol.* 87, 104–113 (2014).
73. Peruzzi, B. & Bottaro, D. P. Targeting the c-Met signaling pathway in cancer. *Clinical Cancer Research* 12, (2006).
74. Inokuchi, M. Clinical significance of MET in gastric cancer. *World J. Gastrointest. Oncol.* 7, 317 (2015).
75. Wang, X. L., Chen, X. M., Fang, J. P. & Yang, C. Q. Lentivirus-mediated RNA silencing of c-Met markedly suppresses peritoneal dissemination of gastric cancer in vitro and in vivo. *Acta Pharmacol. Sin.* 33, 513–522 (2012).
76. Yashiro, M. *et al.* A c-Met inhibitor increases the chemosensitivity of cancer stem cells to the irinotecan in gastric carcinoma. *Br. J. Cancer* 109, 2619–2628 (2013).
77. Egile, C. *et al.* The selective intravenous inhibitor of the MET tyrosine kinase SAR125844 inhibits tumor growth in MET-amplified cancer. *Mol. Cancer Ther.* 14, 384–394 (2015).
78. Hack, S. P., Bruey, J. M. & Koeppen, H. HGF/MET-directed therapeutics in gastroesophageal cancer: A review of clinical and biomarker development. *Oncotarget* 5, 2866–2880 (2014).
79. Doshi, S. *et al.* Rilotumumab exposure-response relationship in patients with advanced or Metastatic gastric cancer. *Clin. Cancer Res.* 21, 2453–2461 (2015).
80. Cunningham, D. *et al.* Phase III, randomized, double-blind, multicenter, placebo (P)-controlled trial of rilotumumab (R) plus epirubicin, cisplatin and capecitabine (ECX) as first-line therapy in patients (pts) with advanced MET-positive (pos) gastric or gastroesophageal junction (G/GEJ) cancer: RILOMET-1 study. *J. Clin. Oncol.* 33, (2015).
81. Foucquier, J. & Guedj, M. Analysis of drug combinations: current methodological landscape. *Pharmacol. Res. Perspect.* 3, (2015).
82. Cetin, R., Quandt, E. & Kaulich, M. Functional genomics approaches to elucidate vulnerabilities of intrinsic and acquired chemotherapy resistance. *Cells* 10, 1–27 (2021).
83. Pommier, Y. Drugging topoisomerases: Lessons and Challenges. *ACS Chemical Biology* 8, (2013).
84. Pommier, Y., Leo, E., Zhang, H. & Marchand, C. DNA topoisomerases and their poisoning by anticancer and antibacterial drugs. *Chemistry and Biology* 17, (2010).
85. Larsen, A. K., Escargueil, A. E. & Skladanowski, A. Catalytic topoisomerase II inhibitors in cancer therapy. *Pharmacology and Therapeutics* 99, (2003).
86. Fortune, J. M. & Osheroff, N. Merbarone inhibits the catalytic activity of human topoisomerase IIα by blocking DNA cleavage. *J. Biol. Chem.* 273, 17643–17650 (1998).
87. Deng, S. *et al.* Dexrazoxane may prevent doxorubicin-induced DNA damage via depleting both Topoisomerase II isoforms. *BMC Cancer* 14, (2014).
88. Hsiang, Y. H., Hertzberg, R., Hecht, S. & Liu, L. F. Camptothecin induces protein-linked DNA breaks via mammalian DNA topoisomerase I. *J. Biol. Chem.* 260, (1985).
89. Ross, W., Glisson, B., Yalowich, J., Rowe, T. & Liu, L. Role of Topoisomerase II in Mediating Epipodophyllotoxin-induced DNA Cleavage. *Cancer Res.* 44, (1984).
90. Werkheiser, W. C. Specific Binding of 4-Amino Folic Acid Analogues by Folic Acid Reductase. *J. Biol. Chem.* 236, (1961).
91. Nuno M. F. S. A. Cerqueira & Ramos, M. J. Ribonucleotide Reductase: A Critical Enzyme for Cancer Chemotherapy and Antiviral Agents. *Recent Pat. Anticancer. Drug Discov.* 2, (2008).
92. Galmarini, C. M., Mackey, J. R. & Dumontet, C. Nucleoside analogues: Mechanisms of drug resistance and reversal strategies. *Leukemia* 15, (2001).
93. Gascoigne, K. E. & Taylor, S. S. How do anti-mitotic drugs kill cancer cells? *Journal of Cell Science* 122, (2009).
94. Sudo, T., Nitta, M., Saya, H. & Ueno, N. T. Dependence of Paclitaxel Sensitivity on a Functional Spindle Assembly Checkpoint. *Cancer Res.* 64, 2502–2508 (2004).
95. Nieuwenhuis, S., Forstmann, B. U. & Wagenmakers, E. J. Erroneous analyses of interactions in neuroscience: A problem of significance. *Nature Neuroscience* 14, (2011).
96. Berenbaum, M. C. Synergy, additivism and antagonism in immunosuppression. A critical review. *Clin. Exp. Immunol.* 28, (1977).
97. Slinker, B. K. The statistics of synergism. *Journal of Molecular and Cellular Cardiology* 30, (1998).
98. BLISS, C. I. the Toxicity of Poisons Applied Jointly. *Ann. Appl. Biol.* 26, 585–615 (1939).
99. Loewe, S. & Muischnek, H. Über Kombinationswirkungen. *Exp Pathol* 313–326 (1926).
100. Tallarida, R. J. An overview of drug combination analysis with isobolograms. *J. Pharmacol. Exp. Ther.* 319, 1–7 (2006).
101. Chou, T. C. Drug combination studies and their synergy quantification using the chou-talalay

method. *Cancer Res.* 70, 440–446 (2010).
102. Chou, T. C. Theoretical basis, experimental design, and computerized simulation of synergism and antagonism in drug combination studies. *Pharmacol. Rev.* 58, 621–681 (2006).
103. Jia, J. *et al.* Mechanisms of drug combinations: Interaction and network perspectives. *Nat. Rev. Drug Discov.* 8, 111–128 (2009).
104. Sun, X., Vilar, S. & Tatonetti, N. P. High-throughput methods for combinatorial drug discovery. *Sci. Transl. Med.* 5, (2013).
105. Alloza, I., Baxter, A., Chen, Q., Matthiesen, R. & Vandenbroeck, K. Celecoxib inhibits interleukin-12 αβ and β2 folding and secretion by a novel COX2-independent mechanism involving chaperones of the endoplasmic reticulum. *Mol. Pharmacol.* 69, (2006).
106. Van Waardenburg, R. C. A. M. *et al.* Platinated DNA adducts enhance poisoning of DNA topoisomerase I by camptothecin. *J. Biol. Chem.* 279, (2004).
107. Cottagnoud, P., Cottagnoud, M. & Täuber, M. G. Vancomycin acts synergistically with gentamicin against penicillin-resistant pneumococci by increasing the intracellular penetration of gentamicin. *Antimicrob. Agents Chemother.* 47, (2003).
108. Pemovska, T., Bigenzahn, J. W. & Superti-Furga, G. Recent advances in combinatorial drug screening and synergy scoring. *Curr. Opin. Pharmacol.* 42, 102–110 (2018).
109. Schaffer, M. *et al.* Identification of potential ibrutinib combinations in hematological malignancies using a combination high-throughput screen. *Leuk. Lymphoma* 59, (2018).
110. Branka, R. S. *et al.* Combinatorial drug screening identifies ewing sarcoma-specific sensitivities. *Mol. Cancer Ther.* 16, (2017).
111. Wassermann, A. M., Camargo, L. M. & Auld, D. S. Composition and applications of focus libraries to phenotypic assays. *Front. Pharmacol.* 5 JUN, 1–12 (2014).
112. Kurtz, S. E. *et al.* Molecularly targeted drug combinations demonstrate selective effectiveness for myeloid- and lymphoid-derived hematologic malignancies. *Proc. Natl. Acad. Sci. U. S. A.* 114, E7554–E7563 (2017).
113. Tentler, J. J. *et al.* Patient-derived tumour xenografts as models for oncology drug development. *Nature Reviews Clinical Oncology* 9, (2012).
114. Gao, H. *et al.* High-throughput screening using patient-derived tumor xenografts to predict clinical trial drug response. *Nat. Med.* 21, (2015).
115. Drost, J. & Clevers, H. Organoids in cancer research. *Nature Reviews Cancer* 18, (2018).
116. Van De Wetering, M. *et al.* Prospective derivation of a living organoid biobank of colorectal cancer patients. *Cell* 161, (2015).
117. Jabs, J. *et al.* Screening drug effects in patient-derived cancer cells links organoid responses to genome alterations. *Mol. Syst. Biol.* 13, (2017).
118. Zappasodi, R., Merghoub, T. & Wolchok, J. D. Emerging Concepts for Immune Checkpoint Blockade-Based Combination Therapies. *Cancer Cell* 33, (2018).
119. Pemovska, T., Bigenzahn, J. W. & Superti-Furga, G. Recent advances in combinatorial drug screening and synergy scoring. *Curr. Opin. Pharmacol.* 42, 102–110 (2018).
120. Fire, A. *et al.* Potent and specific genetic interference by double-stranded RNA in caenorhabditis elegans. *Nature* 391, (1998).
121. Tuschl, T. *et al.* Duplexes of 21-nucleotide RNAs mediate RNA interference in cultured mammalian cells. *Nature* 411, (2001).
122. Brummelkamp, T. R., Bernards, R. & Agami, R. A system for stable expression of short interfering RNAs in mammalian cells. *Science (80-.).* 296, (2002).
123. Carthew, R. W. & Sontheimer, E. J. Origins and Mechanisms of miRNAs and siRNAs. *Cell* 136, (2009).
124. Kim, Y. K. & Kim, V. N. Processing of intronic microRNAs. *EMBO J.* 26, (2007).
125. Bernstein, E., Caudy, A. A., Hammond, S. M. & Hannon, G. J. Role for a bidentate ribonuclease in the. *Nature* 409, 363–366 (2001).
126. Meister, G. *et al.* Human Argonaute2 mediates RNA cleavage targeted by miRNAs and siRNAs. *Mol. Cell* 15, (2004).
127. Heigwer, F., Port, F. & Boutros, M. Rna interference (RNAi) screening in Drosophila. *Genetics* 208, (2018).
128. Cowley, G. S. *et al.* Parallel genome-scale loss of function screens in 216 cancer cell lines for the identification of context-specific genetic dependencies. *Sci. Data* 1, (2014).
129. Barrangou, R. *et al.* CRISPR provides acquired resistance against viruses in prokaryotes. *Science (80-.).* 315, (2007).
130. Jinek, M. *et al.* A programmable dual-RNA-guided DNA endonuclease in adaptive bacterial immunity. *Science (80-.).* 337, (2012).

131. Shmakov, S. *et al.* Diversity and evolution of class 2 CRISPR-Cas systems. *Nat. Rev. Microbiol.* 15, (2017).
132. Hsu, P. D., Lander, E. S. & Zhang, F. Development and applications of CRISPR-Cas9 for genome engineering. *Cell* 157, (2014).
133. Jiang, F. & Doudna, J. A. CRISPR-Cas9 Structures and Mechanisms. *Annual Review of Biophysics* 46, (2017).
134. Palmer, A. C., Chidley, C. & Sorger, P. K. A curative combination cancer therapy achieves high fractional cell killing through low cross resistance and drug Additivity. *Elife* 8, 1–36 (2019).
135. Wang, T., Wei, J. J., Sabatini, D. M. & Lander, E. S. Genetic screens in human cells using the CRISPR-Cas9 system. *Science (80-.).* 343, (2014).
136. Burgess, D. J. *et al.* Topoisomerase levels determine chemotherapy response in vitro and in vivo. *Proc. Natl. Acad. Sci. U. S. A.* 105, (2008).
137. Rafiee, R. *et al.* Genome-Scale CRISPR-Cas9 Synthetic Lethal Screening of AML Cell Line Identified Functional Modulators of Etoposide Resistance Predictive of Clinical Outcome in AML Patients. *Blood* 134, (2019).
138. Rubnitz, J. E. *et al.* Minimal residual disease-directed therapy for childhood acute myeloid leukaemia: Results of the AML02 multicentre trial. *Lancet Oncol.* 11, (2010).
139. Ha, J. S., Byun, J. & Ahn, D. R. Overcoming doxorubicin resistance of cancer cells by Cas9-mediated gene disruption. *Sci. Rep.* 6, 1–7 (2016).
140. Wang, K. *et al.* Targeting uPAR by CRISPR/Cas9 System Attenuates Cancer Malignancy and Multidrug Resistance. *Front. Oncol.* 9, (2019).
141. Goodspeed, A., Jean, A. & Costello, J. C. A Whole-genome CRISPR Screen Identifies a Role of MSH2 in Cisplatin-mediated Cell Death in Muscle-invasive Bladder Cancer. *Eur. Urol.* 75, (2019).
142. Giroux, V., Iovanna, J. & Dagorn, J. Probing the human kinome for kinases involved in pancreatic cancer cell survival and gemcitabine resistance. *FASEB J.* 20, (2006).
143. Ng, S. S. W., Tsao, M. S., Chow, S. & Hedley, D. W. Inhibition of phosphatidylinositide 3-kinase enhances gemcitabine-induced apoptosis in human pancreatic cancer cells. *Cancer Res.* 60, (2000).
144. Bondar, V. M., Sweeney-Gotsch, B., Andreeff, M., Mills, G. B. & McConkey, D. J. Inhibition of the phosphatidylinositol 3′-kinase-AKT pathway induces apoptosis in pancreatic carcinoma cells in vitro and in vivo. *Mol. Cancer Ther.* 1, (2002).
145. Azorsa, D. O. *et al.* Synthetic lethal RNAi screening identifies sensitizing targets for gemcitabine therapy in pancreatic cancer. *J. Transl. Med.* 7, (2009).
146. Fredebohm, J., Wolf, J., Hoheisel, J. D. & Boettcher, M. Depletion of RAD17 sensitizes pancreatic cancer cells to gemcitabine. *J. Cell Sci.* 126, 3380–3389 (2013).
147. Whitehurst, A. W. *et al.* Synthetic lethal screen identification of chemosensitizer loci in cancer cells. *Nature* 446, (2007).
148. Lau, M. T. *et al.* Systematic functional identification of cancer multi-drug resistance genes. *Genome Biol.* 21, (2020).
149. Pritchard, J. R., Bruno, P. M., Hemann, M. T. & Lauffenburger, D. A. Predicting cancer drug mechanisms of action using molecular network signatures. *Mol. Biosyst.* 9, 1604–1619 (2013).
150. Rihel, J. *et al.* Zebrafish behavioral profiling links drugs to biological targets and rest/wake regulation. *Science (80-.).* 327, (2010).
151. Wolpaw, A. J. *et al.* Modulatory profiling identifies mechanisms of small molecule-induced cell death. *Proc. Natl. Acad. Sci. U. S. A.* 108, (2011).
152. Krutzik, P. O., Crane, J. M., Clutter, M. R. & Nolan, G. P. High-content single-cell drug screening with phosphospecific flow cytometry. *Nat. Chem. Biol.* 4, (2008).
153. Bruno, P. M. *et al.* A subset of platinum-containing chemotherapeutic agents kills cells by inducing ribosome biogenesis stress. *Nat. Med.* 23, 461–471 (2017).
154. Oždian, T. *et al.* Abstract 455: Cellular response to oxaliplatin treatment shows altered DNA damage, nucleolar and ribosomal stresses as main altered pathways. *Cancer Res.* 78, (2018).
155. Ozdian, T. *et al.* Proteomic profiling reveals DNA damage, nucleolar and ribosomal stress are the main responses to oxaliplatin treatment in cancer cells. *J. Proteomics* 162, (2017).
156. Richards, R., Honeywell, M. E. & Lee, M. J. FLICK: An optimized plate reader-based assay to infer cell death kinetics. *STAR Protoc.* 2, 100327 (2021).
157. Hart, T. *et al.* Evaluation and design of genome-wide CRISPR/SpCas9 knockout screens. *G3 Genes, Genomes, Genet.* 7, 2719–2727 (2017).
158. Cruz-Gordillo, P., Honeywell, M. E., Harper, N. W., Leete, T. & Lee, M. J. ELP-dependent expression of MCL1 promotes resistance to EGFR inhibition in triple-negative breast cancer

cells. *Sci. Signal.* 13, 1–13 (2020).
159. Jiang, H., Pritchard, J. R., Williams, R. T., Lauffenburger, D. A. & Hemann, M. T. A mammalian functional-genetic approach to characterizing cancer therapeutics. *Nat. Chem. Biol.* 7, 92–100 (2011).
160. Dickins, R. A. *et al.* Probing tumor phenotypes using stable and regulated synthetic microRNA precursors. *Nat. Genet.* 37, 1289–1295 (2005).
161. Zuber, J. *et al.* Toolkit for evaluating genes required for proliferation and survival using tetracycline-regulated RNAi. *Nat. Biotechnol.* 29, 79–85 (2011).
162. Pritchard, J. R. *et al.* Defining principles of combination drug mechanisms of action. *Proc. Natl. Acad. Sci. U. S. A.* 110, (2013).
163. Schwartz, H. R. *et al.* Drug GRADE: An Integrated Analysis of Population Growth and Cell Death Reveals Drug-Specific and Cancer Subtype-Specific Response Profiles. *Cell Rep.* 31, 107800 (2020).
164. Hafner, M., Niepel, M., Chung, M. & Sorger, P. K. Growth rate inhibition metrics correct for confounders in measuring sensitivity to cancer drugs. *Nat. Methods* 13, 521–527 (2016).
165. Ku, J.-L. & Park, J.-G. Biology of SNU cells. 37, 337–344 (2010).
166. Thomas, A. & Pommier, Y. Targeting topoisomerase I in the era of precision medicine. *Clin. Cancer Res.* 25, 6581–6589 (2019).
167. Natale, F. *et al.* Identification of the elementary structural units of the DNA damage response. *Nat. Commun.* 8, (2017).
168. Shen, T. *et al.* Erlotinib inhibits colon cancer metastasis through inactivation of TrkB-dependent ERK signaling pathway. *J. Cell. Biochem.* 120, 11248–11255 (2019).
169. Meyn, R. E., Munshi, A., Haymach, J. V., Milas, L. & Ang, K. K. Receptor signaling as a regulatory mechanism of DNA repair. *Radiother. Oncol.* 92, 316–322 (2009).
170. Hart, T. *et al.* High-Resolution CRISPR Screens Reveal Fitness Genes and Genotype-Specific Cancer Liabilities. *Cell* 163, 1515–1526 (2015).
171. Broderick, R., Rainey, M. D., Santocanale, C. & Nasheuer, H. P. Cell cycle-dependent formation of Cdc45-Claspin complexes in human cells is compromized by UV-mediated DNA damage. *FEBS J.* 280, 4888–4902 (2013).
172. Broderick, R. & Nasheuer, H. P. Regulation of Cdc45 in the cell cycle and after DNA damage. *Biochem. Soc. Trans.* 37, 926–930 (2009).
173. Luijsterburg, M. S. *et al.* A PALB2-interacting domain in RNF168 couples homologous recombination to DNA break-induced chromatin ubiquitylation. *Elife* 6, 1–26 (2017).
174. Chen, B. *et al.* STK3 promotes gastric carcinogenesis by activating Ras-MAPK mediated cell cycle progression and serves as an independent prognostic biomarker. *Mol. Cancer* 20, 1–8 (2021).
175. Ma, H. T. & Poon, R. Y. C. Aurora kinases and DNA damage response. *Mutat. Res. - Fundam. Mol. Mech. Mutagen.* 821, 111716 (2020).
176. Taguchi, K. & Yamamoto, M. The KEAP1NRF2 system in cancer. *Front. Oncol.* 7, 1–11 (2017).
177. Orthwein, A. *et al.* A mechanism for the suppression of homologous recombination in G1 cells. *Nature* 528, 422–426 (2015).
178. Krall, E. B. *et al.* KEAP1 loss modulates sensitivity to kinase targeted therapy in lung cancer. *Elife* 6, 1–21 (2017).
179. Smits, V. A. J., Cabrera, E., Freire, R. & Gillespie, D. A. Claspin – checkpoint adaptor and DNA replication factor. *FEBS J.* 286, 441–455 (2019).
180. Bianco, J. N. *et al.* Overexpression of Claspin and Timeless protects cancer cells from replication stress in a checkpoint-independent manner. *Nat. Commun.* 10, (2019).
181. Li, S. *et al.* GINS1 Induced Sorafenib Resistance by Promoting Cancer Stem Properties in Human Hepatocellular Cancer Cells. *Front. Cell Dev. Biol.* 9, 1–11 (2021).
182. Worster, D. T. *et al.* Akt and ERK control the proliferative response of mammary epithelial cells to the growth factors IGF-1 and EGF through the cell cycle inhibitor p57 Kip2. *Sci. Signal.* 5, (2012).
183. Hegedüs, C. *et al.* Interaction of the EGFR inhibitors gefitinib, vandetanib, pelitinib and neratinib with the ABCG2 multidrug transporter: Implications for the emergence and reversal of cancer drug resistance. *Biochem. Pharmacol.* 84, (2012).
184. Pick, A. & Wiese, M. Tyrosine Kinase Inhibitors Influence ABCG2 Expression in EGFR-Positive MDCK BCRP Cells via the PI3K/Akt Signaling Pathway. *ChemMedChem* 7, 650–662 (2012).
185. Robey, R. W. *et al.* ABCG2: A perspective. *Advanced Drug Delivery Reviews* 61, (2009).
186. Scharenberg, C. W., Harkey, M. A. & Torok-Storb, B. The ABCG2 transporter is an efficient Hoechst 33342 efflux pump and is preferentially expressed by immature human hematopoietic

progenitors. *Blood* 99, 507–512 (2002).
187. Stoczynska-Fidelus, E., Węgierska, M., Kierasińska, A., Ciunowicz, D. & Rieske, P. Role of Senescence in Tumorigenesis and Anticancer Therapy. *Journal of Oncology* 2022, (2022).
188. Kuczler, M. D., Olseen, A. M., Pienta, K. J. & Amend, S. R. ROS-induced cell cycle arrest as a mechanism of resistance in polyaneuploid cancer cells (PACCs). *Prog. Biophys. Mol. Biol.* 165, (2021).
189. Zang, Z. J. *et al.* Exome sequencing of gastric adenocarcinoma identifies recurrent somatic mutations in cell adhesion and chromatin remodeling genes. *Nat. Genet.* 44, (2012).
190. Mandal, J., Mandal, P., Wang, T. L. & Shih, I. M. Treating ARID1A mutated cancers by harnessing synthetic lethality and DNA damage response. *J. Biomed. Sci.* 29, 1–15 (2022).
191. Willis, S. E. *et al.* Retrospective analysis of Schlafen11 (SLFN11) to predict the outcomes to therapies affecting the DNA damage response. *Br. J. Cancer* 125, 1666–1676 (2021).
192. Schaefer, G., Shao, L., Totpal, K. & Akita, R. W. Erlotinib directly inhibits HER2 kinase activation and downstream signaling events in intact cells lacking epidermal growth factor receptor expression. *Cancer Res.* 67, (2007).
193. Huang, W., Wan, C., Luo, Q., Huang, Z. & Luo, Q. Genistein-inhibited cancer stem cell-like properties and reduced chemoresistance of gastric cancer. *Int. J. Mol. Sci.* 15, (2014).
194. Yu, B., Gu, D., Zhang, X., Liu, B. & Xie, J. The role of GLI2-ABCG2 signaling axis for 5Fu resistance in gastric cancer. *J. Genet. Genomics* 44, (2017).